25 Mössbauer Spectroscopy

E. Kuzmann[1] · *Z. Homonnay*[1] · *S. Nagy*[1] · *K. Nomura*[2]
[1]Eötvös Loránd University, Budapest, Hungary
[2]The University of Tokyo, Tokyo, Japan

Attila Vértes, Sándor Nagy, Zoltán Klencsár, Rezső G. Lovas & Frank Rösch (eds.), *Handbook of Nuclear Chemistry*,
DOI 10.1007/978-1-4419-0720-2_25,

Abstract: Mössbauer spectroscopy, based on the recoilless resonance emission and absorption of γ photons observed with certain atomic nuclei, is a powerful investigating tool in most disciplines of natural science ranging from physics to chemistry to biology. This nuclear method makes it possible to measure the energy difference between nuclear energy levels to an extremely high resolution (up to 13–15 decimals). This resolution is required to measure the slight variation of nuclear energy levels caused by electric monopole, electric quadrupole, and magnetic dipole interactions between the electrons and the nucleus. Mössbauer nuclides being at different microenvironments act as local probes for the sensitive detection of the hyperfine interactions. Such interactions reflect changes in the electronic, magnetic, geometric, or defect structure as well as in the lattice vibrations, serving as a basis for a variety of applications. In this chapter, the principles and some practical aspects of Mössbauer spectroscopy are described.

25.1 Principles of Mössbauer Spectroscopy

Mössbauer spectroscopy is based on the Mössbauer effect discovered by Rudolf Mössbauer (Mössbauer 1958a, b). The discovery was honored by the Nobel Prize in 1961.

Mössbauer effect is the recoilless (also called: recoil-free) nuclear resonance emission/absorption of γ rays (see *Fig. 25.1*). In the case of a nuclear transition, the de-excited nucleus is normally recoiled by the momentum of the γ photon emitted, which makes its resonance absorption impossible by another ground-state nucleus of the same type. In solids, however, recoilless photons can be emitted (and reabsorbed by another ground-state nucleus) with some probability.

A number of monographs and articles describe the basic aspects and applications of Mössbauer spectroscopy in detail (see, e.g., Kagan 1962; Goldanskii 1963; Frauenfelder 1962; Wertheim 1964; Abragam 1964; Wegener 1965; Gruverman 1965–1976; Danon 1968; Matthias and Shirley 1968; Goldanskii and Herber 1968; Shpinel 1969; Greenwood and Gibb 1971; Sano 1972; May 1971; Janot 1972; Kaipov 1976; Bancroft 1973; Bhide 1973; Cohen and

Fig. 25.1

Schematic representation of nuclear resonance based on the recoilless emission and absorption of a γ photon. The story that goes with the figure is this. A nucleus in excited state emits a γ photon with energy (E_0) equal to the difference between the energies of the excited-and ground-state levels, and, subsequently, the same γ photon is absorbed resonantly by another nucleus in the ground state by transforming it to the excited state. This sounds rather trivial but in order to happen both the emission and the absorption of the photon must be a recoilless/recoil-free event (this is called the Mössbauer effect), because recoil of either nucleus would render the energy of the photon insufficient for the resonance to occur

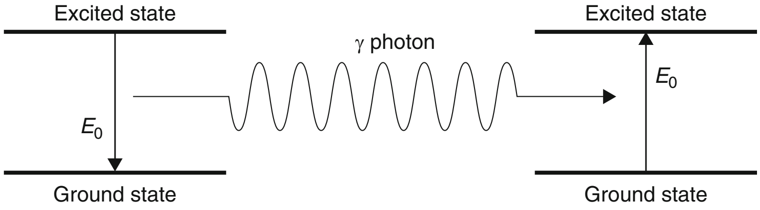

Pasternak 1973; Gruverman and Seidel 1973; Gonser 1975a; Gibb 1976; Cohen 1976; Perlow 1977; Shenoy and Wagner 1978; Gütlich et al. 1978; Vértes et al. 1979; Cohen 1980; Gonser 1981; Mørup 1981; Stevens and Shenoy 1981; Thosar and Iyengar 1983; Long 1984; Herber 1984; Cranshaw et al. 1985; Long 1987, 1989; Vértes and Nagy 1990; Long and Grandjean 1993; Schatz et al. 1996; Long and Grandjean 1996, 1997; Vértes and Homonnay 1997; Fujita 1999). The Mössbauer Effect Reference and Data Index (MERDI) (Muir et al. 1958–1965; Stevens and Stevens 1966–) and Journal (MERDJ) serve as an important data source and contain a compilation of all references in the field.

25.1.1 Isomeric Transition Between Nuclear Levels

With regard to the nuclear resonance effect of γ rays, the (median) energy, E_0, of the transition and the mean life, τ, of the excited state are very important parameters. The fact that the mean life of the excited state is finite – that the excited state sooner or later "decays" to the ground state according to the exponential law of decay (see Chap. 7 in Vol. 1 on the "Kinetics of Radioactive Decay") – causes a "blurring" of the supposedly discrete energy of the excited level. The energy of the excited nuclear levels is characterized by a $C(E_0,\Gamma/2)$ Cauchy distribution (see Chap. 9 in Vol. 1 on the "Stochastics and Nuclear Measurements") whose un-normalized density function is called a *Lorentzian* (or *Breit–Wigner*) *curve* in physics (Breit and Wigner 1936):

$$L(E) = A\frac{\Gamma}{2\pi}\frac{1}{(E-E_0)^2+\left(\frac{\Gamma}{2}\right)^2} = H\left(\frac{\Gamma}{2}\right)^2\frac{1}{(E-E_0)^2+\left(\frac{\Gamma}{2}\right)^2} \qquad (25.1)$$

where A is the area under the Lorentzian curve (i.e., for $A = 1$, $L(E)$ is a normalized $C(E_0,\Gamma/2)$ density function), H is the height of the Lorentzian at its maximum (i.e., at $E = E_0$), and $E_0 = E_e - E_g$ is the transition energy, i.e., the median difference between the energies of the excited state and the ground state. (The adjective "median" is used as a technical term here. The reason for avoiding the more usual term "mean" is that the underlying Cauchy distribution does not have a mean in the statistical sense; however, it *does* have a median.) Finally, Γ is the natural line width representing the full width at half maximum (FWHM) of the bell-shaped Lorentzian.

The *natural line width* Γ is also referred to sometimes as the "Heisenberg line width" because it obeys the following equation (see also Eq. (2.36) in Chap. 2, Vol. 1, as well as remarks #62–64 in Chap. 9, Vol. 1.):

$$\Gamma\tau = \hbar. \qquad (25.2)$$

For the stationary ground state, the mean life is infinite, and Eq. (25.2) shows that such a state is indeed sharp having $\Gamma = 0$. For the excited state, on the other hand, the mean life is finite, so it will result in an energy uncertainty in the range of 10^{-12} to 10^{-5} eV for the states interesting from the point of view of Mössbauer spectroscopy.

Normally, the photons emitted in an isomeric transition will only have the sharp energy distribution of the excited state shown by Eq. (25.1) if the emission is recoilless. In general, however, there will be an energy loss E_R due to the recoil of the body that emits the radiation. (In the case of gases, this body is the nucleus (atom). With solids, the situation is more complex as it will be pointed out later on.)

To calculate E_R, consider an isolated nucleus of mass M that had been at rest before the decay took place and the photon got emitted. It follows from momentum conservation that $p_N = p_\gamma$, where p_N is the magnitude of the momentum of the recoiled nucleus and $p_\gamma = E_\gamma/c$ is that of the photon. The recoil energy can therefore be given as $E_R = (p_N)^2/(2M)$. Since E_R is small compared with E_0, one can set $E_\gamma = E_0 - E_R \approx E_0$ and thus the *recoil energy* can be expressed as

$$E_R = \frac{E_0^2}{2Mc^2}. \tag{25.3}$$

Considering the excited nuclei of such isolated atoms at rest, the (median) energy of the emitted γ photons (i.e., $E_0 - E_R$) will be less than the transition energy E_0. For the $\pm 3/2 \rightarrow \pm 1/2$ transition of ^{57}Fe, which is the most frequently used Mössbauer nuclide, one has $E_0 = 14.4$ keV, $\Gamma = 4.67 \times 10^{-9}$ eV, $E_R = 1.92 \times 10^{-3}$ eV. The energy distribution of the emitted photons – called the emission line that is characterized by a Lorentzian having line width Γ – gets shifted toward the low energies. On the other hand, the energy distribution of the photons, which can be absorbed resonantly by the ground-state nucleus – called the absorption line – is characterized by the same line width, Γ, with a median energy $E_0 + E_R$ due to the recoil of the absorbing nucleus. Resonance absorption can only occur when the absorption and emission lines overlap each other. In other words, the shift between the absorption and emission lines cannot exceed substantially 2Γ. However, in case of recoil, the energy separation between the emission and absorption lines (which is $2E_R$) can be by six orders of magnitude larger than Γ in the case of ^{57}Fe. Thus, there is no overlap between the emission and absorption lines, and, consequently, no resonant absorption occurs in this case.

25.1.2 Thermal Broadening: γ Emission and Absorption in Gases

In the case of gases, one should also consider that the atoms move with relatively large velocities and thus the energy of the emitted γ rays is modified by the Doppler shift. This will cause a smearing out of both the emission and absorption lines and lead to an additional broadening of the spectrum peaks, which is called the *Doppler* or *thermal broadening*.

Let $\boldsymbol{x}$ refer to the direction of γ emission/observation. The energy of the γ photon emitted by an atom moving at velocity $\boldsymbol{u}$ is now

$$E_\gamma = (E_0 - E_R)\left(1 + \frac{u}{c}\cos\theta\right) \tag{25.4}$$

where $u = |\boldsymbol{u}|$ is the speed of the atom, and θ is the angle between $\boldsymbol{u}$ and the $\boldsymbol{x}$-axis as shown in *Fig. 25.2*.

Since the direction of γ emission is independent of the velocity of the particle, the expected value of the γ energy is easily calculated as

$$\langle E_\gamma \rangle = (E_0 - E_R)\left(1 + \frac{\langle u \rangle}{c}\langle \cos\theta \rangle\right) \tag{25.5}$$

where $\langle u \rangle$ is the mean speed of the atom as calculated from the Boltzmann distribution, and $\langle \cos\theta \rangle$ is calculated with the density function $(\sin\theta)/2$ according to *Fig. 25.2*.

Due to symmetry, $\langle \cos\theta \rangle = 0$ and therefore

$$\langle E_\gamma \rangle = E_0 - E_R \tag{25.6}$$

that is, thermal motion does not affect the mean energy at all.

Fig. 25.2

Representation of the notation used in the calculation of Doppler broadening. The density function that is used for averaging out *θ* (for all possible values between 0 and π) should be proportional to the circumference 2π sin*θ* of the shaded disc that is perpendicular to the *x*-axis at *x* = cos*θ*

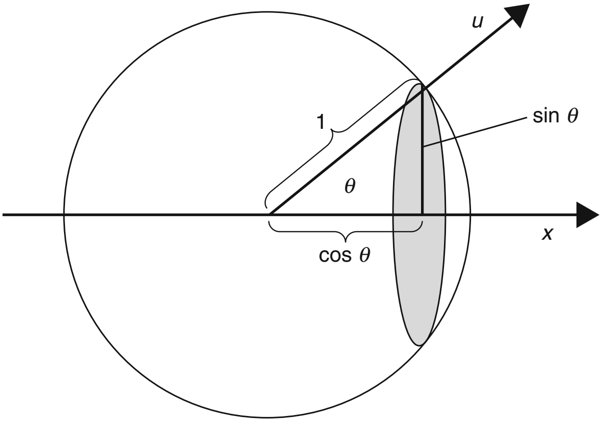

The variance of the γ energy (i.e., *Doppler broadening*), on the other hand, *does* depend on temperature as one can easily show

$$D^2(E_\gamma) = \left\langle (E_\gamma - \langle E_\gamma \rangle)^2 \right\rangle = (E_0 - E_\mathrm{R})^2 \frac{\langle u^2 \rangle}{c^2} \langle \cos^2\theta \rangle = (E_0 - E_\mathrm{R})^2 \frac{\langle u^2 \rangle}{3c^2} \tag{25.7}$$

where the same density function was used as before for averaging out θ, and $\langle u^2 \rangle$ is the mean square speed of the atoms.

The temperature dependence can be made explicit by using the kinetic theory of gases according to which

$$\frac{M\langle u^2 \rangle}{2} = \frac{3kT}{2} \tag{25.8}$$

Thus, one observes the following formula for the standard deviation of the γ energy:

$$D(E_\gamma) = (E_0 - E_\mathrm{R})\sqrt{\frac{kT}{Mc^2}} \approx E_0\sqrt{\frac{kT}{Mc^2}} = \sqrt{2kTE_\mathrm{R}} \tag{25.9}$$

where it was made use of the fact that $E_\mathrm{R} \ll E$.

For the $\pm 3/2 \rightarrow \pm 1/2$ transition of ^{57}Fe one has $D(E_\gamma) = 1.0 \times 10^{-2}$ eV at 300 K. Since $D(E_\gamma)$ is commensurable with E_R, one can see that Doppler broadening can cause some overlapping between the shifted emission and absorption lines (*Fig. 25.3*), and thus a small yield of nuclear resonance absorption is to be expected (and, indeed, achieved; see Malmfors 1953). However, if the overlap occurs due to such thermal motion, the essence of using resonant nuclear absorption to develop a spectroscopic method with an extremely high-energy resolution is lost.

Fig. 25.3

Doppler/thermal broadening in gases. Thermal motion causes blurring of the (normalized) emission and absorption profiles. At high-enough temperatures, the profiles will overlap thus bridging the gap of $2E_R$ between the maxima. Without recoil (and thermal broadening), both the emission and the absorption profile would be represented by a Lorentzian at E_0, with a full width at half maximum (FWHM) so small that the (normalized) peak would be way out of the vertical scale

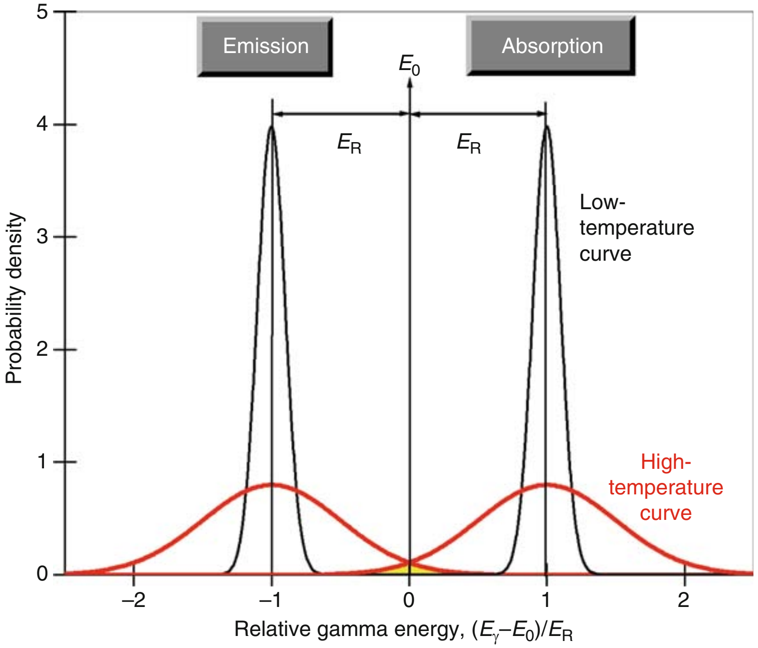

25.1.3 Recoilless γ Emission and Absorption in Condensed Matter, the Mössbauer Effect

25.1.3.1 Conditions of Nuclear Resonance Absorption

Before the discovery of the Mössbauer effect, many attempts had been made to improve the chances for γ ray resonance absorption. The idea was to make the overlap between the emission and absorption lines larger by setting the emitter/absorber nuclei in motion (in order to compensate for the energy loss due to recoil) either mechanically (Moon 1950) or thermally (Malmfors 1953).

The key problem, i.e., how to avoid recoil and Doppler broadening at the same time, has been solved by Rudolf Mössbauer (Mössbauer 1958a) when he discovered that γ-ray emitting and absorbing nuclei if embedded in the lattice of a solid give rise to a recoilless line (the so-called Mössbauer line) at the energy E_0.

The cross section for the resonant absorption depends on the energy E of the γ photons. The energy dependence can be expressed by a Lorentzian shown by ❯ Eq. (25.1) (Frauenfelder 1962):

$$\sigma = \sigma_0 \left(\frac{\Gamma}{2}\right)^2 \frac{1}{(E - E_0)^2 + \left(\frac{\Gamma}{2}\right)^2} \tag{25.10}$$

where σ_0 is the maximum of the resonant cross section for which one has

$$\sigma_0 = 2\pi \lambda\!\!\!^{-2} \frac{2I_e + 1}{2I_g + 1} \frac{1}{1 + \alpha} \tag{25.11}$$

where I_e and I_g are the nuclear spin quantum numbers of the excited and ground state, respectively, $\lambda\!\!\!^{-} \equiv \lambda/(2\pi)$ is proportional to the wavelength λ of the γ ray, and α is the internal conversion coefficient (see Sect. 2.3.2.1 in Chap. 2, Vol. 1).

25.1.3.2 Lattice Vibrations

Mössbauer effect is unique in that it provides a means of eliminating the destructive effect of recoil and thermal energies. In the Mössbauer domain, recoil energy is much less than the chemical binding energy and also less than the energy needed to excite lattice vibrations (phonons). Since the energy of lattice vibrations is quantized, the relatively low recoil energy cannot be transferred to the solid to increase its internal vibrational energy. It can only be transferred to the lattice, if it suffices to induce a vibrational quantum jump. If no quantum jump occurs (as in the case of the Mössbauer effect), then the recoil energy can be considered as being taken by the whole crystal grain as a rigid object in which the Mössbauer nuclide is embedded. The recoiled mass (M) in the denominator of Eq. (25.3) becomes extremely large (in fact, it becomes equal to the mass of the whole grain), and therefore the recoil energy E_R will be negligibly small in comparison with the natural line width Γ.

In order to understand the interactions between the emitting/absorbing nuclei and the lattice, some basics of the Einstein model and the Debye model of solids are needed.

The *Einstein model* (Kittel 1968) assumes that the solid is composed of a large number of independent linear oscillators each vibrating at the same angular frequency ω_E. (Each atom is represented by three oscillators, one for each dimension.) As the temperature increases, the oscillators keep vibrating with the same frequency, however, the amplitude of vibration – and so the mean square displacement of the atoms – becomes larger. The Einstein frequency ω_E is associated with the Einstein temperature θ_E:

$$\hbar\omega_E = k\theta_E \tag{25.12}$$

and the Einstein energy E_E, which is the minimum of vibrational energy that the lattice can emit or absorb:

$$E_E = \hbar\omega_E = \frac{\hbar c_s}{\lambda\!\!\!^{-}_s} = \frac{\pi\hbar c_s}{a} \tag{25.13}$$

where a is the lattice constant, c_s is the speed of the sound waves in the solid, and $2\pi\lambda\!\!\!^{-}_s$ is the wavelength of the sound associated with the vibration. The wavelength is supposed to satisfy the condition $\lambda_s = 2a$. For the bcc iron lattice (α-Fe), this yields $E_E = 0.04$ eV.

It is interesting to compare the γ emission of different isotopes of iron embedded in the same α-Fe lattice. Consider, e.g., the 14 keV transition of ^{57}Fe and the 800 keV transition of ^{58}Fe. It is found that the recoil energy of ^{57}Fe ($E_R = 0.002$ eV) is small compared with the Einstein energy ($E_E = 0.04$ eV) and, consequently, recoilless emission can occur. For ^{58}Fe, on the other hand, the recoil energy ($E_R = 6$eV) is large enough to excite the lattice.

The Einstein model gives a good qualitative agreement with the real behavior of solids, but the quantitative agreement is poor (Cranshaw et al. 1985). A more realistic representation of a solid is given by the *Debye model*. The model describes the lattice vibration of solids as a superposition of independent vibrational modes (i.e., collective wave motion of the lattice, associated with "phonons") with different frequencies. The (normalized) density function $p(\omega)$ of the vibrational frequencies is monotonically increasing up to a characteristic maximum of ω_D, where it abruptly drops to zero (Kittel 1968):

$$p(\omega) = \begin{cases} 3\frac{\omega^2}{\omega_\mathrm{D}^3} & \text{for } 0 \le \omega \le \omega_\mathrm{D} \\ 0 & \text{elsewhere} \end{cases} \tag{25.14}$$

It is usual to express the cutoff frequency ω_D with the characteristic Debye temperature θ_D:

$$\hbar\omega_\mathrm{D} = k\theta_\mathrm{D} \tag{25.15}$$

The energy is quantized for each possible frequency ω:

$$\varepsilon_n = \left(n + \frac{1}{2}\right)\hbar\omega \tag{25.16}$$

where n is a quantum number ($n = 0, 1, 2\ldots$).

The mean energy for a given frequency ω at a given temperature T is calculated as

$$\bar{\varepsilon}(\omega, T) = \frac{\sum\limits_{n=0}^{\infty} \varepsilon_n \exp\left(-\frac{\varepsilon_n}{kT}\right)}{\sum\limits_{n=0}^{\infty} \exp\left(-\frac{\varepsilon_n}{kT}\right)} = \left(\bar{n}(\omega, T) + \frac{1}{2}\right)\hbar\omega \tag{25.17}$$

where $\bar{n}(\omega, T)$, representing the mean of the quantum number n, is called the Bose–Einstein distribution function

$$\bar{n}(\omega, T) = \frac{1}{\exp\left(\frac{\hbar\omega}{kT}\right) - 1} \tag{25.18}$$

In quantum theory, the time-average of the square displacement (and that of the square speed) of an atom doing harmonic oscillation along the x-axis with angular frequency ω is given by

$$\langle x^2\rangle_{\omega,T} = \frac{\langle \dot{x}^2\rangle_{\omega,T}}{\omega^2} = \left(\bar{n}(\omega, T) + \frac{1}{2}\right)\frac{\hbar}{M\omega} \tag{25.19}$$

where M is the mass of the atom and the subscripts are to indicate that the time-averages depend on both the frequency and the temperature.

The *mean square displacement* at a given temperature is obtained by averaging the time-average of the square displacement over all frequencies:

$$\langle x^2\rangle_T = \int\limits_0^{\omega_\mathrm{D}} \langle x^2\rangle_{\omega,T}\, p(\omega)\mathrm{d}\omega = \frac{3\hbar^2}{Mk\theta_\mathrm{D}}\left[\frac{1}{4} + \left(\frac{T}{\theta_\mathrm{D}}\right)^2 \int\limits_0^{\theta_\mathrm{D}/T} \frac{x}{\mathrm{e}^x - 1}\mathrm{d}x\right]. \tag{25.20}$$

For very low and very high temperatures, Eq. (25.20) can be approximated by the following expressions:

$$\langle x^2 \rangle_T \approx \frac{3\hbar^2}{Mk\theta_D}\left[\frac{1}{4}+\left(\frac{T}{\theta_D}\right)^2\frac{\pi^2}{6}\right], \quad T \ll \theta_D, \tag{25.21}$$

$$\langle x^2 \rangle_T \approx \frac{3\hbar^2}{Mk\theta_D}\frac{T}{\theta_D}, \quad T \gg \theta_D \tag{25.22}$$

Note that Eqs. (25.20)–(25.22) justify the intuitive expectation that the mean square displacement of the vibrating atoms should increase with temperature.

The *mean square velocity* of the lattice vibration, $\langle u^2 \rangle$, at a given temperature can be derived similarly to that of mean square displacement, and obtained as

$$\langle u^2 \rangle_T = \int_0^{\omega_D} \langle u^2 \rangle_{\omega,T}\, p(\omega)\mathrm{d}\omega = \frac{9k\theta_D}{M}\left[\frac{1}{8}+\left(\frac{T}{\theta_D}\right)^4 \int_0^{\theta_D/T} \frac{x^3}{\mathrm{e}^x - 1}\mathrm{d}x\right] \tag{25.23}$$

25.1.3.3 The Probability of the Mössbauer Effect

The probability of the recoilless emission or absorption is given by the *recoilless fraction f*, meaning the fraction of all γ rays of the Mössbauer transition that are emitted (f_S) or absorbed (f_A) without recoil-energy loss. This is also commonly referred to as the Mössbauer fraction, Debye–Waller factor, Mössbauer–Lamb factor or, simply, the *f*-factor.

The theory of the *Mössbauer–Lamb factor* has been developed by several authors (Lamb 1939; Mössbauer 1958a; Singwi and Sjolander 1960; Lipkin 1960; Shapiro 1960).

In its most general form, the recoilless fraction is given by the following formulas that are completely equivalent to each other:

$$f = \exp(-k^2\langle x^2 \rangle_T) = \exp\left(-\frac{\langle x^2 \rangle_T}{\lambda\!\!\!^{-2}}\right) = \exp\left(-\frac{E_0^2}{\hbar^2 c^2}\langle x^2 \rangle_T\right) = \exp\left(-\frac{2ME_R}{\hbar^2}\langle x^2 \rangle_T\right) \tag{25.24}$$

where $k/(2\pi)$ is the wave number of the γ ray:

$$k = \frac{2\pi}{\lambda} = \frac{1}{\lambda\!\!\!^{-}} = \frac{E_0}{\hbar c} \tag{25.25}$$

Equation (25.24) carries several important messages for the Mössbauer spectroscopist:

1. The recoilless fraction decreases with increasing γ energy (note that in the recoilless case $E_\gamma = E_0$ except for the energy uncertainty expressed by Eq. (25.2)). This means that isomeric transitions with $E_0 \geq 200$ keV are not practical for the purpose of Mössbauer spectroscopy, since the *f*-factor would be too small. (The Mössbauer effect has been observed with over 100 transitions of near 50 elements shown in *Fig. 25.4*. The nuclear data for the Mössbauer transitions are summarized in Sect. 36.1 of the Appendix of this Volume.)
2. Since according to Eq. (25.21) the value of $\langle x^2 \rangle_T$ is supposed to decrease on cooling, the recoilless fraction should increase when the temperature is lowered. This was the crucial and unexpected finding of the first recoilless resonance absorption experiment by Rudolf Mössbauer using ^{191}Ir, which lead to the discovery of the Mössbauer effect (Mössbauer 1958a).

The explicit temperature dependence of the Mössbauer–Lamb factor can be estimated from the Debye model by using Eqs. (25.20)–(25.22) and (25.24):

Fig. 25.4

The Mössbauer periodic table. Shaded cells contain elements with no known Mössbauer isotope. Unshaded cells also indicate the mass number(s) of the Mössbauer isotope(s) below the chemical symbol. For brevity's sake no more than two (of the most important) isotopes are indicated for each element. An asterisk "*" after the last mass number means that the full list of the Mössbauer isotopes (see Sect. 36.1 of the Appendix of this Volume) is longer than shown here

IA	IIA	IIIB	IVB	VB	VIB	VIIB	VIIIB			IB	IIB	IIIA	IVA	VA	VIA	VIIA	VIIIA
1 H																	2 He
3 Li	4 Be											5 B	6 C	7 N	8 O	9 F	10 Ne
11 Na	12 Mg											13 Al	14 Si	15 P	16 S	17 Cl	18 Ar
19 K 40	20 Ca	21 Sc	22 Ti	23 V	24 Cr	25 Mn	26 Fe 57	27 Co	28 Ni 61	29 Cu	30 Zn 67	31 Ga	32 Ge 73	33 As	34 Se	35 Br	36 Kr 83
37 Rb	38 Sr	39 Y	40 Zr	41 Np	42 Mo	43 Tc 99	44 Ru 99 101	45 Rh	46 Pd	47 Ag 107	48 Cd 201	49 In	50 Sn 117 119	51 Sb 121	52 Te 125	53 I 127 129	54 Xe 129 131
55 Cs 133	56 Ba 133	57 La 139	72 Hf 178 180*	73 Ta 181	74 W 184 186*	75 Re 187	76 Os 188 190*	77 Ir 191 193	78 Pt 195	79 Au 197	80 Hg 201	81 Ti	82 Pb	83 Bi	84 Po	85 At	86 Rn
87 Fr	88 Ra	89 Ac	104 Rf	105 Db	106 Sg	107 Bh	108 Hs	109 Mt	110 Dm								

58 Ce	59 Pr 141	60 Nd 145	61 Pm 145 147	62 Sm 152 154*	63 Eu 151 153	64 Gd 154– 158*	65 Tb 159	66 Dy 160– 162*	67 Ho 165	68 Er 166 168*	69 Tm 169	70 Yb 172 174*	71 Lu 175
90 Th 232	91 Pa 231	92 U 238*	93 Np 237	94 Pu 239	95 Am 243	96 Cm	97 Bk	98 Cf	99 Es	100 Fm	101 Md	102 No	103 Lr

$$f(T) = \exp\left\{ -\frac{6E_{\mathrm{R}}}{k\theta_{\mathrm{D}}} \left(\frac{1}{4} + \left(\frac{T}{\theta_{\mathrm{D}}} \right)^2 \int\limits_0^{\theta_{\mathrm{D}}/T} \frac{x}{\mathrm{e}^x - 1} \mathrm{d}x \right) \right\}. \tag{25.26}$$

Let us emphasize here, however, that the Debye model had been developed for a monatomic cubic lattice, and thus the quantitative results applied to an arbitrary lattice must be taken with more than a grain of suspicion.

25.1.4 The Mössbauer Spectrum

Figure 25.5 shows the schematic arrangement of a typical transmission *Mössbauer experiment*. The assembly consists of a source, an absorber, and a detector.

Fig. 25.5
Schematic arrangement of a transmission type Mössbauer measurement. The scanning of the absorption line with the emission line using the Doppler principle is illustrated. The intensity of the resultant spectrum is proportional to the overlap of the emission and absorption lines (marked at four arbitrarily chosen velocities u_1 to u_4)

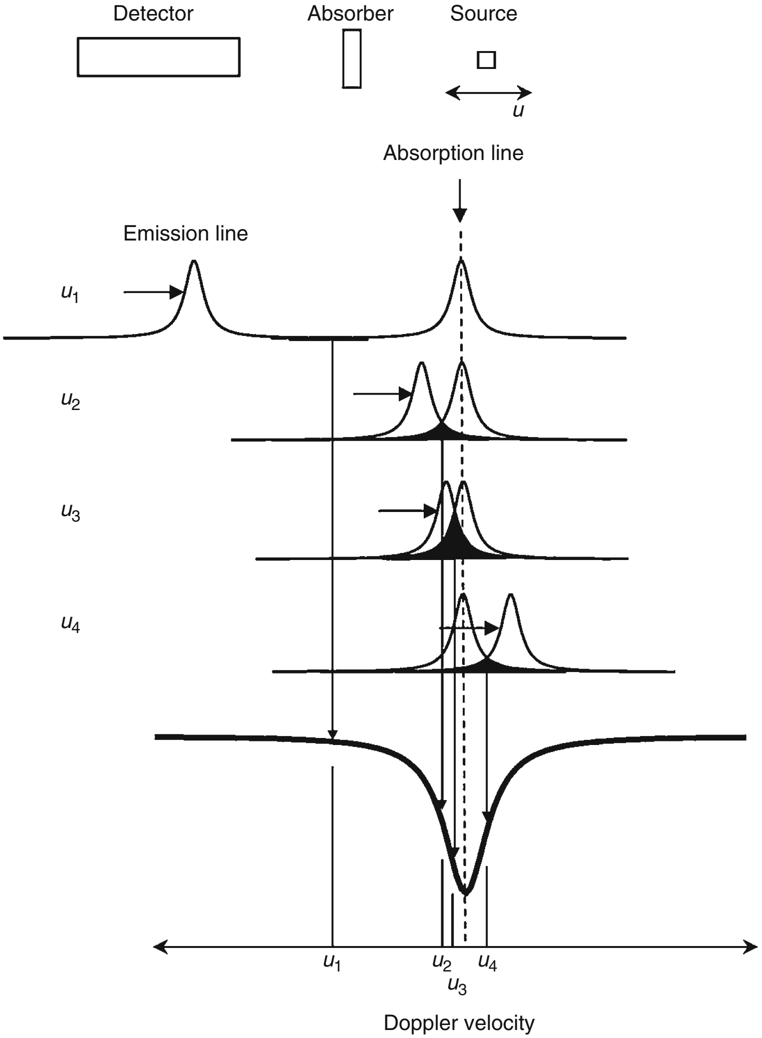

The *source* is a body containing the excited-state nuclei of a Mössbauer-active nuclide "frozen" in a solid matrix thus providing the conditions for recoilless γ emission.

The *absorber* is another body that contains the ground-state nuclei of the same Mössbauer-active nuclide also "frozen" in a solid matrix so satisfying the conditions for recoilless absorption.

The γ photons transmitted by the absorber are counted by the detector.

The resonance curve of the absorber (absorption line), however, cannot be measured at all by any existing detector, since it would require an energy resolution (Γ/E_0) of about 13–15 orders of magnitude. Therefore, the Mössbauer nuclei themselves are used to measure the resonance curve in the following way. If both the source and the absorber are at rest, and have the same chemical environment for the Mössbauer nuclei, then there is a maximum overlap of the emission and the absorption lines, and a certain intensity is observed by the detector. This ideal condition for the resonance absorption is destroyed by modifying the energy of the emission line according to the Doppler effect by moving the source with velocity u, relative to the absorber. This action results in a decreased overlap of the emission and absorption lines and therefore an increased count rate of the detector (see ➲ *Fig. 25.5*). A systematic energy modification of the emission line on the basis of the Doppler effect can be used to scan the absorption characteristics of the absorber very sensitively (with the required resolution). The count rate detected as a function of the Doppler velocity results in the Mössbauer spectrum.

The Mössbauer spectrum itself is usually presented as a plot of counts/percentage/fraction of transmission vs. channel/Doppler velocity.

The transmitted intensity vs. Doppler velocity (i.e., the transmission Mössbauer spectrum) will show a resonance "dip" around the Doppler velocity where the overlap is at its maximum (see ➲ *Fig. 25.6*).

In the *simplest* (thin-source, thin-absorber) *approximation*, a simple transmission Mössbauer spectrum (➲ *Fig. 25.6*) consists of one single *Lorentzian peak* the half width of which corresponds to twice of the natural line width $\Gamma = \hbar \ln 2/T_{1/2}$ (in energy unit). (The natural line width Γ is characteristic of both the recoilless emission in the source and the resonant absorption in the absorber. So doubling is actually the result of "adding up.") The peak width $W_0 = 2c\Gamma/E_\gamma$ (in speed unit) thus obtained is an asymptotic minimum to which (normally) actual experimental peak widths are compared. For the $3/2 \rightarrow 1/2$ (see ➲ *Fig. 25.7*) transition of ^{57}Fe, e.g., $W_0 \approx 0.2$ mm/s is the minimum (or natural) peak width.

In the general case, the peak width will be broadened and the peak shape will be different from Lorentzian.

A general evaluation of the integrated absorption intensity is rather difficult, but a useful result can be obtained under the following conditions (Margulies and Ehrman 1961).

Let both the emission and absorption line be centered at E_0 and have the same natural line width $\Gamma_S = \Gamma_A = \Gamma$. The distribution of the ground-state Mössbauer atoms in question (e.g., ^{57}Fe) is taken to be uniform in both the source and the absorber. The distribution of the parent atoms (e.g., ^{57}Co) producing the excited Mössbauer atoms (➲ *Fig. 25.7*) (and thus the γ photons) is described by the density function $\rho(x)$ along the $\mathbf{x}$-axis (see ➲ *Fig. 25.6* for the notation). In the derivation of the peak shape of the Mössbauer spectrum, nonresonant and resonant absorption processes are to be considered in both the source and the absorber as illustrated schematically in ➲ *Fig. 25.6*.

The γ radiation emitted by the excited Mössbauer nuclei will be attenuated by both "electronic" absorption/scattering (mainly due to photoelectric effect) and resonance absorption by ground-state nuclei.

Electronic absorption consumes both the recoiled $(1 - f_S)$ and the recoilless fraction (f_S) of photons. Their attenuation is described by the coefficients μ_S and μ_A for the source and the absorber, respectively. The electronic attenuation coefficients can be considered constant over the whole Doppler-velocity range.

Resonance absorption only concerns the recoilless fraction (f_S) of the radiation. According to ➲ Eq. (25.1), the energy distribution of this fraction can be given as

Fig. 25.6

Schematic transmission Mössbauer spectrum (*bottom*) with notations for the simplest arrangement (*top*). Either the source or the absorber is vibrated by a transducer. As usual, positive Doppler velocities (*u*) refer to approaching source and absorber

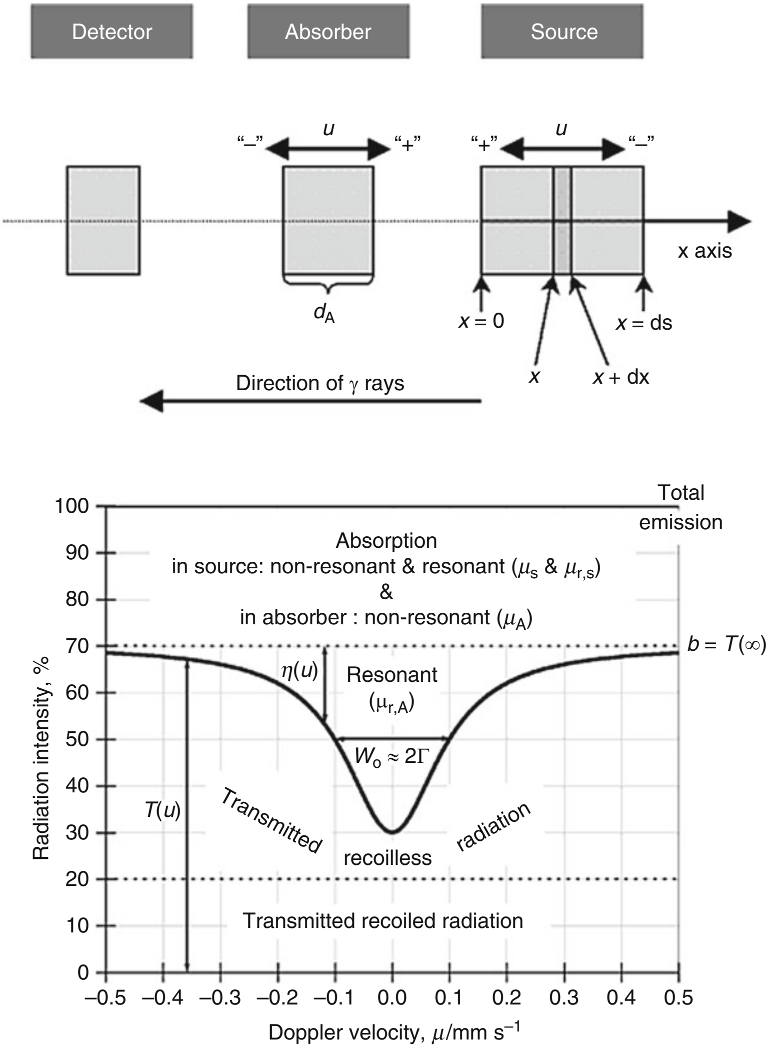

$$L(E) = f_S \frac{\Gamma}{2\pi} \frac{1}{(E - E_0)^2 + \left(\frac{\Gamma}{2}\right)^2}. \tag{25.27}$$

The attenuation coefficients $\mu_{r,S}$ and $\mu_{r,A}$ that characterize the resonance absorption of the recoilless radiation (in the source and in the absorber, respectively) are, however, energy dependent.

Using Eq. (25.10), for the case when the source is at rest and the absorber is moving with relative velocity u one can write

Fig. 25.7

Decay scheme of ^{57}Co to ^{57}Fe. The half-lives of γ transitions are indicated in parentheses

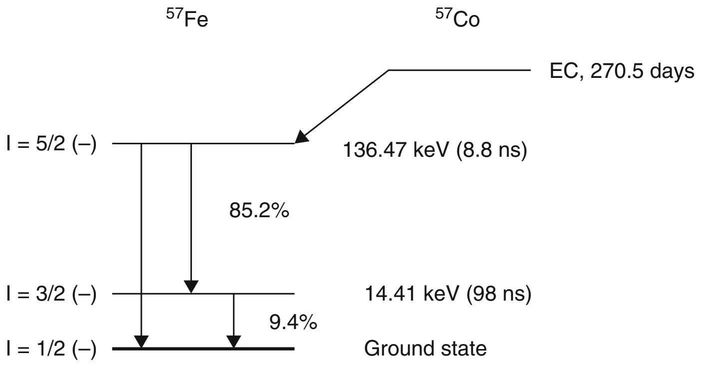

$$\mu_{\mathrm{r,S}} = \frac{f_{\mathrm{S}} n_{\mathrm{S}} a_{\mathrm{S}} \sigma_0 (\Gamma/2)^2}{(E - E_0)^2 + (\Gamma/2)^2}, \quad \mu_{\mathrm{r,A}} = \frac{f_{\mathrm{A}} n_{\mathrm{A}} a_{\mathrm{A}} \sigma_0 (\Gamma/2)^2}{[E - E_0(1 - u/c)]^2 + (\Gamma/2)^2} \tag{25.28}$$

where f_{S} and f_{A} are the Mössbauer–Lamb factors, n_{S} and n_{A} are the number densities (unit: number of atoms per volume) of the Mössbauer element (e.g., Fe), a_{S} and a_{A} are the fractional abundances of the Mössbauer isotope (e.g., ^{57}Fe in Fe), for the source and absorber, respectively, and σ_0 is the maximum of resonant absorption cross section given by Eq. (25.11).

Note that the negative sign before u/c in the second formula means that when the absorber approaches the source, the positive Doppler shift helps lower-energy γ photons to meet the condition of resonance absorption. As a result of this, the absorption line represented by the second formula is shifted to the left by the Doppler term.

The fraction of γ photons reaching the detector (considering only those photons that are emitted in the direction of the detector) can be given as

$$\begin{aligned} T(u) = \Bigg\{ & (1 - f_{\mathrm{S}}) \left[\int_0^{d_{\mathrm{S}}} \rho(x) \exp(-\mu_{\mathrm{S}} x) \mathrm{d}x \right] \\ & + f_{\mathrm{S}} \Bigg[\int_{-\infty}^{+\infty} \frac{\Gamma}{2\pi} \frac{1}{(E - E_0)^2 + (\Gamma/2)^2} \\ & \times \int_0^{d_{\mathrm{S}}} \rho(x) \exp\left(- \frac{f_{\mathrm{S}} n_{\mathrm{S}} a_{\mathrm{S}} \sigma_0 (\Gamma/2)^2}{(E - E_0)^2 + (\Gamma/2)^2} x - \mu_{\mathrm{S}} x \right) \mathrm{d}x \\ & \times \exp\left(- \frac{\tau_{\mathrm{A}} (\Gamma/2)^2}{[E - E_0(1 - u/c)]^2 + (\Gamma/2)^2} \right) \mathrm{d}E \Bigg] \Bigg\} \exp(-\mu_{\mathrm{A}} d_{\mathrm{A}}) \end{aligned} \tag{25.29}$$

where d_{A} is the thickness, and τ_{A} is the *effective thickness* of the absorber:

$$\tau_{\mathrm{A}} = f_{\mathrm{A}} n_{\mathrm{A}} a_{\mathrm{A}} d_{\mathrm{A}} \sigma_0. \tag{25.30}$$

The first term (line 1) in Eq. (25.29) represents the γ radiation emitted with recoil from the source (S) in which it is attenuated by nonresonant absorption via Compton or photoelectric effect as it proceeds toward the absorber (A). This term is independent of the Doppler shift.

Line 2 contains the $C(E_0,\Gamma/2)$ Cauchy distribution of the γ photons emitted from the source without recoil.

Line 3 describes the resonant and nonresonant (self) absorption within the source for the recoilless γ photons emitted at different depths (x) of the source while they proceed toward the front of the source ($x = 0$) on their way to the absorber.

The first exponential in line 4 expresses the resonant absorption of the recoilless γ photons in the absorber that moves with velocity u toward the source. Finally, the factor $\exp(-\mu_A d_A)$ in the same line accounts for the nonresonant absorption/scattering in the absorber attenuating both the recoiled and the recoilless photons.

In the case of an infinitely thin source – when the radioactive parent forms a monatomic layer on the front of the source at $x = 0$, and therefore $\rho(x) = \delta(x)$, where δ is the Dirac "function" – lines 1 and 3 in Eq. (25.29) are equal to $(1 - f_S)$ and 1, respectively. Therefore, one obtains the following formula, generally called the *transmission integral*:

$$T(u) = \left\{ 1 - f_S + \int_{-\infty}^{+\infty} \frac{\frac{\Gamma f_S}{2\pi}}{(E - E_0)^2 + \left(\frac{\Gamma}{2}\right)^2} \exp\left(- \frac{\tau_A \left(\frac{\Gamma}{2}\right)^2}{\left[E - E_0\left(1 - \frac{u}{c}\right)\right]^2 + \left(\frac{\Gamma}{2}\right)^2} \right) \mathrm{d}E \right\} e^{-\mu_A d_A} \tag{25.31}$$

For very large Doppler speeds, there is no resonance absorption at all (note that the exponential part of the integrand is 1 at the limit $|u| \to \infty$), and therefore, the baseline b can be expressed as

$$b = T(\infty) = \mathrm{e}^{-\mu_A d_A}. \tag{25.32}$$

The contour of the transmission peak (see *Fig. 25.6*) can be easily determined from the above equations:

$$\eta(u) = \frac{b - T(u)}{b} = f_S \left\{ 1 - \int_{-\infty}^{+\infty} \frac{\frac{\Gamma}{2\pi}}{(E - E_0)^2 + \left(\frac{\Gamma}{2}\right)^2} \exp\left(- \frac{\tau_A \left(\frac{\Gamma}{2}\right)^2}{\left[E - E_0\left(1 - \frac{u}{c}\right)\right]^2 + \left(\frac{\Gamma}{2}\right)^2} \right) \mathrm{d}E \right\} \tag{25.33}$$

If the effective thickness of the absorber is very small (i.e., $\tau_A \to 0$), then the exponential in the integrand of Eq. (25.33) can be replaced by the linear terms of its Taylor series.

As a result, the peak shape can be expressed by the following integral:

$$\eta(u) = f_S \tau_A \int_{-\infty}^{+\infty} \frac{\frac{\Gamma}{2\pi}}{(E - E_0)^2 + \left(\frac{\Gamma}{2}\right)^2} \times \frac{\left(\frac{\Gamma}{2}\right)^2}{\left[E - E_0\left(1 - \frac{u}{c}\right)\right]^2 + \left(\frac{\Gamma}{2}\right)^2} \mathrm{d}E. \tag{25.34}$$

Using the residuum theorem, the above formula yields

$$\eta(u) = \frac{f_S \tau_A}{2} \frac{\Gamma^2}{\left(\frac{E_0}{c} u\right)^2 + \Gamma^2} = \frac{f_S \tau_A}{2} \frac{\left(\frac{W_0}{2}\right)^2}{u^2 + \left(\frac{W_0}{2}\right)^2}. \tag{25.35}$$

As it has turned out, the peak shape – in this thin-source, thin-absorber approximation – is indeed Lorentzian, and the FWHM of the peak (W_0), apart from the conversion factor between Doppler speed and energy, is twice the natural line width Γ.

$$W_0 = 2\Gamma \frac{c}{E_0}. \tag{25.36}$$

Note also that the height of the peak is proportional to the effective thickness and, consequently, (through the number density n_A) to the concentration of the Mössbauer species:

$$\eta(0) = \frac{f_S \tau_A}{2} = \frac{f_S f_A n_A a_A d_A \sigma_0}{2}. \tag{25.37}$$

In the general case, one observes a nonlinear formula for the peak height (Mössbauer and Wiedemann 1960):

$$\eta(0) = f_S \left[1 - \exp\left(-\frac{\tau_A}{2}\right) I_0\left(\frac{\tau_A}{2}\right) \right] \tag{25.38}$$

where I_0 is the 0^{th} order modified Bessel function of the first kind (see, e.g., BESSEL 2010). The peak area can be obtained by the integration of Eq. (25.33):

$$A = \int_{-\infty}^{\infty} \eta(u) \mathrm{d}u = \pi \Gamma f_S \frac{\tau_A}{2} \exp\left(-\frac{\tau_A}{2}\right) \left[I_0\left(\frac{\tau_A}{2}\right) + I_1\left(\frac{\tau_A}{2}\right) \right] \tag{25.39}$$

where I_1 is the first-order modified Bessel function of the first kind.

In the case of a thin absorber ($\tau_A \rightarrow 0$), the Taylor expansion of the exponential and Bessel functions yields a proportional relationship between the peak area and the number of resonant atoms in the absorber:

$$A \approx \frac{\pi \Gamma f_S \tau_A}{2}. \tag{25.40}$$

The latter equation is fundamental in Mössbauer spectroscopy establishing its use as a tool of quantitative analysis.

25.1.5 Hyperfine Interactions

The interaction between the electrons and the nucleus causes a very small perturbation of the nuclear energy levels in comparison with the energy of the nuclear transition. Such interactions are called *hyperfine interactions*. The main hyperfine interactions are the following: electric monopole, electric quadrupole, and magnetic dipole interactions between the nucleus and the electrons (shell electrons, ligands, etc.). Such interactions can be sensitively monitored by Mössbauer spectroscopy. The measurement of hyperfine interactions is the key to the utilization of Mössbauer spectroscopy in a wide range of applications.

Hyperfine interactions shift and/or split the energy levels of the nucleus. The total Hamiltonian can be written as a sum of various contributions:

$$H = H_0 + H_C + H_Q + H_m, \tag{25.41}$$

where $\boldsymbol{H}_C$, $\boldsymbol{H}_Q$, and $\boldsymbol{H}_m$ refer to electric monopole (Coulomb) interaction, electric quadrupole interaction, and magnetic dipole interaction, respectively, and $\boldsymbol{H}_0$ represents all other terms not considered here.

All of the hyperfine interactions may occur together, but only the magnetic and quadrupole interactions are directional thus having a complicated interrelationship.

25.1.5.1 Electric Monopole Interaction

The electric monopole interaction is part of the full electric Coulomb interaction occurring between the nucleus and the surrounding charges. Because of this interaction, the energy levels of the nucleus become shifted. The corresponding energy shift of the ground-state nuclear level may differ from that of the excited state level when the finite size of the nucleus is taken into consideration. (If the nucleus were a point charge, the Coulomb shift due to electrons would be the same for its ground state and its excited state.) Consequently, the electric monopole interaction leads to a change in the energy of the emitted γ ray compared to the case of a bare nucleus that is without any surrounding electric charge (Dunlap and Kalvius 1978).

The full *Coulomb interaction* between the nuclear charge distribution $e\rho_{\mathrm{N}}(\boldsymbol{r}_{\mathrm{N}})$ and the electronic charge distribution $-e\rho_{\mathrm{e}}(\boldsymbol{r}_{\mathrm{e}})$ is given by

$$U = -e^2 \iint \frac{\rho_{\mathrm{e}}(r_{\mathrm{e}})\rho_{\mathrm{N}}(r_{\mathrm{N}})}{|r_{\mathrm{e}} - r_{\mathrm{N}}|} \mathrm{d}V_{\mathrm{e}} \mathrm{d}V_{\mathrm{N}} \tag{25.42}$$

where $\boldsymbol{r}_{\mathrm{e}}$ and $\boldsymbol{r}_{\mathrm{N}}$ are location vectors, and $\mathrm{d}V_{\mathrm{e}}$ and $\mathrm{d}V_{\mathrm{N}}$ are the volume elements containing the points determined by $\boldsymbol{r}_{\mathrm{e}}$ and $\boldsymbol{r}_{\mathrm{N}}$, respectively.

The above equation can be rewritten by using the following multipole expansion (Clauser and Mössbauer 1969):

$$\frac{1}{|r_{\mathrm{e}} - r_{\mathrm{N}}|} = \sum_{l=0}^{\infty} \sum_{m=-l}^{+l} \frac{2\pi}{2l+1} \left(\frac{r_<^l}{r_>^{l+1}} \right) Y_{lm}^*(\theta_{\mathrm{N}}, \phi_{\mathrm{N}}) Y_{lm}(\theta_{\mathrm{e}}, \phi_{\mathrm{e}}) \tag{25.43}$$

where Y_{lm} are the normalized spherical harmonics, $r_<$ and $r_>$ are the smaller and the larger of $|\boldsymbol{r}_{\mathrm{e}}|$ and $|\boldsymbol{r}_{\mathrm{N}}|$, respectively.

The full Coulomb interaction energy term can be expressed by combining Eqs. (25.42) and (25.43) as the sum of a number of terms with multipole order l. The term for $l = 0$ is the electric monopole term. The $l = 2$ term gives rise to electric quadrupole interactions and will be discussed later. (All the odd l terms vanish for reasons of symmetry. The very small even terms for $l > 2$ can also be ignored.)

For $l = 0$, the energy of the interaction is

$$U_0 = -e^2 \iint \frac{\rho_{\mathrm{e}}(r_{\mathrm{e}})\rho_{\mathrm{N}}(r_{\mathrm{N}})}{r_>} \mathrm{d}V_{\mathrm{e}} \mathrm{d}V_{\mathrm{N}}. \tag{25.44}$$

In Mössbauer spectroscopy, the only thing that matters is not the energy shift of an individual level, but the energy-shift difference between the ground-state and excited-state levels. Let us consider the energy shifts of the nuclear levels due to the electric monopole interaction and the energy of the γ ray emitted from the source and absorbed by the absorber (*Fig. 25.8*).

If the nuclei did not experience any hyperfine interaction, they would have the same energy levels in both the source and the absorber ($E^{\mathrm{S}*} = E^{\mathrm{A}*}$, $E^{\mathrm{S}} = E^{\mathrm{A}}$, and thus $E^{\mathrm{S}*} - E^{\mathrm{S}} = E^{\mathrm{A}*} - E^{\mathrm{A}} = E_0$, see *Fig. 25.8* for notations). With a finite size nucleus the Coulomb term, U_0, can be different for the excited state ($U_{0,\mathrm{S}}^*$) and the ground state ($U_{0,\mathrm{S}}$) in the source, and also for the excited state ($U_{0,\mathrm{A}}^*$) and the ground state ($U_{0,\mathrm{A}}$) in the absorber.

The energy of the γ ray emitted from the source will be

$$E_\gamma^{\mathrm{S}} = (E^{\mathrm{S}*} - E^{\mathrm{S}}) + (U_{0,\mathrm{S}}^* - U_{0,\mathrm{S}}) = E_0 + \varDelta E_{\mathrm{C}}^{\mathrm{S}} \tag{25.45}$$

where the notation $\varDelta E_{\mathrm{C}}^{\mathrm{S}} = (U_{0,\mathrm{S}}^* - U_{0,\mathrm{S}})$ has been introduced.

Fig. 25.8

The shifts of nuclear energy levels in the source and the absorber due to the electric monopole interaction between the nucleus and the electrons, and the resulted Mössbauer spectrum. According to Eq. (25.80), the chemical isomer shift δ_c is proportional to the energy shift ΔE_{IS}

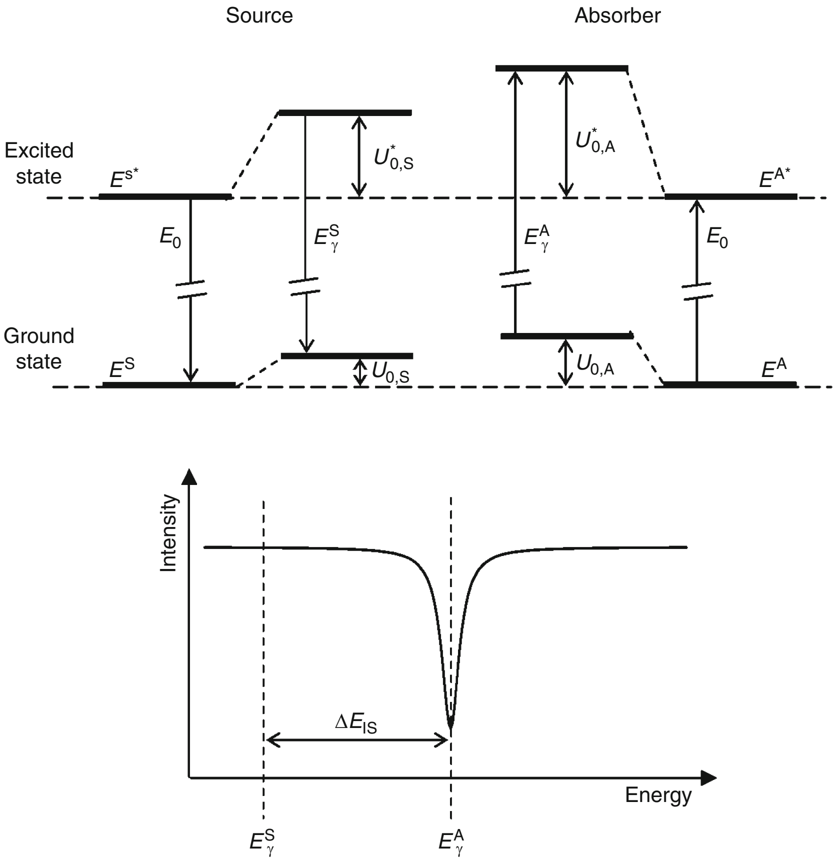

The energy of the γ ray, which can be absorbed by the absorber will be

$$E_\gamma^A = (E^{A*} - E^A) + (U_{0,A}^* - U_{0,A}) = E_0 + \varDelta E_C^A \tag{25.46}$$

with the notation $\varDelta E_C^A = (U_{0,A}^* - U_{0,A})$.

The energy difference

$$\varDelta E_{IS} = E_\gamma^A - E_\gamma^S = \varDelta E_C^A - \varDelta E_C^S = (U_{0,A}^* - U_{0,A}) - (U_{0,S}^* - U_{0,S}) \tag{25.47}$$

is the missing (or excess) energy of the γ quantum emitted by the source that needs to be compensated in the Mössbauer experiment in order to achieve maximum resonance absorption, i.e., maximum overlap between the emission and absorption lines (*Fig. 25.5*). In the corresponding Mössbauer spectrum, the need for this compensation of energy appears as a line shift (see *Fig. 25.8*) that is called the *chemical isomer shift*.

By substituting the Coulomb shifts $U^*_{0,\mathrm{A}}, U_{0,\mathrm{A}}, U^*_{0,\mathrm{S}}$, and $U_{0,\mathrm{S}}$ in Eq. (25.47) with corresponding expressions according to Eq. (25.44) one obtains

$$\Delta E_{\mathrm{IS}} = \\ -e^2 \iint \frac{\rho^*_{\mathrm{e,A}}(r_\mathrm{e})\rho^*_{\mathrm{N,A}}(r_\mathrm{N}) - \rho_{\mathrm{e,A}}(r_\mathrm{e})\rho_{\mathrm{N,A}}(r_\mathrm{N}) - \rho^*_{\mathrm{e,S}}(r_\mathrm{e})\rho^*_{\mathrm{N,S}}(r_\mathrm{N}) + \rho_{\mathrm{e,S}}(r_\mathrm{e})\rho_{\mathrm{N,S}}(r_\mathrm{N})}{r_>} \mathrm{d}V_\mathrm{e}\,\mathrm{d}V_\mathrm{N} \tag{25.48}$$

where the asterisk (*) refers to the excited state of the nucleus in the source ($_\mathrm{S}$) and in the absorber ($_\mathrm{A}$).

In order to get a simpler expression for the chemical isomer shift, it will be assumed that the electronic charge density around the nucleus is the same whether or not the nucleus is excited:

$$\rho^*_{\mathrm{e,S}}(r_\mathrm{e}) = \rho_{\mathrm{e,S}}(r_\mathrm{e});\, \rho^*_{\mathrm{e,A}}(r_\mathrm{e}) = \rho_{\mathrm{e,A}}(r_\mathrm{e}). \tag{25.49}$$

It is plausible to assume that for a given energy state of the nucleus the nuclear charge density is the same in the source and in the absorber:

$$\rho^*_{\mathrm{N,S}}(r_\mathrm{N}) = \rho^*_{\mathrm{N,A}}(r_\mathrm{N}) \equiv \rho^*_{\mathrm{N}}(r_\mathrm{N});\, \rho_{\mathrm{N,S}}(r_\mathrm{N}) = \rho_{\mathrm{N,A}}(r_\mathrm{N}) \equiv \rho_{\mathrm{N}}(r_\mathrm{N}). \tag{25.50}$$

Introducing spherically averaged electronic densities

$$\bar\rho_\mathrm{e}(r_\mathrm{e}) = \frac{1}{4\pi}\iint \rho_\mathrm{e}(r_\mathrm{e}) \sin\theta\, \mathrm{d}\theta\, \mathrm{d}\phi, \tag{25.51}$$

and assuming that the nuclear charge distribution is spherically symmetric one obtains

$$\Delta E_{\mathrm{IS}} = -4\pi e^2 \int_0^\infty \left(\rho^*_\mathrm{N}(r_\mathrm{N}) - \rho_\mathrm{N}(r_\mathrm{N})\right) I(r_\mathrm{N})\mathrm{d}r_\mathrm{N}. \tag{25.52}$$

with

$$I(r_\mathrm{N}) = \int_0^{r_\mathrm{N}} \left(\bar\rho_{\mathrm{e,A}}(r_\mathrm{e}) - \bar\rho_{\mathrm{e,S}}(r_\mathrm{e})\right)\left(\frac{1}{r_\mathrm{N}} - \frac{1}{r_\mathrm{e}}\right) r_\mathrm{e}^2 \mathrm{d}r_\mathrm{e}. \tag{25.53}$$

Thus, ΔE_{IS} will depend on the assumptions made for the radial dependence of the average electronic densities in the source and in the absorber within the nuclear volume.

In light atoms (for which $Z \ll 137 \approx 1/\alpha$, where α is the fine-structure constant) relativistic effects are negligible. In such a case, only s electrons (having spherically symmetric distribution) have nonvanishing charge density at the place of the nucleus. Considering also the small size of the nucleus, the electronic density can be taken to be approximately constant over the nuclear volume, and therefore:

$$\bar\rho_\mathrm{e}(r_\mathrm{e}) = \rho_\mathrm{e}(r_\mathrm{e}) = \rho_\mathrm{e}(0) \equiv |\psi(0)|^2 \tag{25.54}$$

where $\psi(0)$ is the nonrelativistic many-electron wave function at the place of the nucleus. Thus, carrying out the integration in Eq. (25.53) one obtains

$$I(r_\mathrm{N}) = -\frac{1}{6} r_\mathrm{N}^2 |\psi(0)|^2. \tag{25.55}$$

Substituting this result into Eq. (25.52), for the chemical isomer shift one obtains the expression

$$\Delta E_{\mathrm{IS}} = \frac{2\pi e^2}{3}\Delta|\psi(0)|^2 \int_0^\infty \Delta\rho_\mathrm{N}(r_\mathrm{N}) r_\mathrm{N}^2 \mathrm{d}r_\mathrm{N} = \frac{2\pi Z e^2}{3}\Delta|\psi(0)|^2 \Delta\langle r_\mathrm{N}^2\rangle. \tag{25.56}$$

Note that on the right-hand side of the equation, the *first* $\mathit{\Delta}$ (related to the atomic electrons through $\mathit{\Psi}$) refers to the *difference between absorber and source*, while the *second* $\mathit{\Delta}$ (related to the nucleus through r_N) refers to the *difference between the nuclear states.*

In Eq. (25.56) the following expression was used for the *mth momentum of the nuclear charge distribution*:

$$\langle r^m \rangle = \frac{\int r_\mathrm{N}^m \rho_\mathrm{N}(r_\mathrm{N})\mathrm{d}V_\mathrm{N}}{\int \rho_\mathrm{N}(r_\mathrm{N})\mathrm{d}V_\mathrm{N}} = \frac{1}{Z}\int r_\mathrm{N}^m \rho_\mathrm{N}(r_\mathrm{N})\mathrm{d}V_\mathrm{N}. \tag{25.57}$$

According to Eq. (25.56), one obtains that the energy shift due to electric monopole interaction is proportional to the product of the s electronic density and the second moment of the nuclear charge distribution also called the *mean square nuclear charge radius* (see also Sect. 2.2.3.1 in Chap. 2, Vol. 1). When the nucleus is considered to be a homogeneously charged sphere with a radius R (often called charge equivalent nuclear radius), then

$$\rho_\mathrm{N}(r_\mathrm{N}) = \frac{3Z}{4\pi R^3} \tag{25.58}$$

and therefore

$$\langle r_\mathrm{N}^2 \rangle = \frac{3}{5}R^2 \tag{25.59}$$

which yields the following expression for the chemical isomer shift:

$$\mathit{\Delta} E_\mathrm{IS} = \frac{2\pi Z e^2}{5}\mathit{\Delta}|\psi(0)|^2 \mathit{\Delta} R^2. \tag{25.60}$$

By considering also relativistic effects, in addition to s electrons relativistic $\mathrm{p}_{1/2}$ electrons will also turn out to have finite density at the place of the nucleus. Then, for a uniformly charged spherical nucleus of radius R, single-electron approximation gives the following radial density distribution $\rho_\mathrm{e}(r)$:

$$\rho_\mathrm{e}(r) = \rho_\mathrm{e}(0)\left[1 - \frac{\alpha^2 Z^2}{2}\left(\frac{r}{R}\right)^2 + \frac{\alpha^2 Z^2}{10}\left(1 + \frac{9\alpha^2 Z^2}{8}\right)\left(\frac{r}{R}\right)^4 + \cdots\right]. \tag{25.61}$$

Hence, the energy corresponding to the chemical isomer shift can be written as

$$\mathit{\Delta} E_\mathrm{IS} = \frac{2\pi}{5} Z e^2 S'(Z)\mathit{\Delta} R^2 \mathit{\Delta}|\psi(0)|^2, \tag{25.62}$$

where the numerical factor $S'(Z)$, the so-called *Shirley factor*, corrects the nonrelativistic electron density for relativistic effects. Its value is 1.29 for ^{57}Fe, 2.31 for ^{119}Sn, and 13.6 for ^{237}Np (Shirley 1964).

In the case of a relativistic multi-electron system, further considerations are necessary. The total electron density can be written as

$$\rho_\mathrm{e}(r) = \rho_\mathrm{e}(0)[1 - a_2 r^2 + a_4 r^4 - \cdots] \tag{25.63}$$

which will introduce higher moments of the nuclear charge distribution into the expression of the energy corresponding to the chemical isomer shift:

$$\Delta E_\mathrm{IS} = \frac{2\pi}{3} Z e^2 \mathit{\Delta}\rho_\mathrm{e}(0)[\mathit{\Delta}\langle r^2\rangle - b_4 \mathit{\Delta}\langle r^4\rangle + b_6 \mathit{\Delta}\langle r^6\rangle - \ldots]. \tag{25.64}$$

25.1.5.2 Electric Quadrupole Interaction

A nucleus with nonzero nuclear quadrupole moment is subject to electric quadrupole interaction if it is experiencing an inhomogeneous electric field. The latter is characterized by the electric field gradient (EFG) tensor defined by $\nabla \circ \boldsymbol{E} = -\nabla \circ \nabla V$, where "∘" indicates dyadic product (the matrix product of a column vector and a row vector resulting in a square matrix). The V_{ij} element of the EFG tensor is given by

$$V_{ij} = -\frac{\partial^2 V}{\partial x_i \partial x_j} (x_i, x_j = x, y, z) \tag{25.65}$$

where V is the electrostatic potential. (Note that from this point on only those charges are considered that are outside the volume of the nucleus.) The EFG tensor can be transformed into its *principal axis system (PAS)* where it is represented by a diagonal matrix with components V_{xx}, V_{yy}, and V_{zz}. One can show that electric charge distributions with spherical symmetry around the nucleus (like s electrons) do not contribute to the electric quadrupole interaction. According to the Laplace equation $\nabla^2 V = V_{xx} + V_{yy} + V_{zz} = 0$ outside the sources of the electric field. Therefore, the EFG at the place of the nucleus is traceless and two independent parameters are enough to specify it completely. The two parameters used in practice are the principal component V_{zz} and the asymmetry parameter η defined as

$$\eta = \frac{V_{xx} - V_{yy}}{V_{zz}}. \tag{25.66}$$

By convention the PAS is chosen such that $|V_{xx}| \leq |V_{yy}| \leq |V_{zz}|$ is satisfied, which ensures $0 \leq \eta \leq 1$.

In operator form, the nuclear quadrupole moment is given by

$$Q_{ik} = \frac{3Q}{2I(2I-1)} \left[I_i I_k + I_k I_i - \frac{2}{3} I^2 \delta_{ik} \right] \tag{25.67}$$

where $\boldsymbol{I}$ is the nuclear spin operator and δ_{ik} is the *Kronecker delta*. The energy term for the quadrupole interaction, $\frac{e}{6} \sum_{i,k} V_{ik} Q_{ik}$, can be derived by expanding the electrostatic potential into a series at the center of the nucleus (see, e.g., Gütlich et al. 1978). The Hamiltonian for the quadrupole interaction turns out to be

$$\begin{aligned} H_{\mathrm{Q}} = \frac{e}{6} \sum_i V_{ii} Q_{ii} &= \frac{eQ}{2I(2I-1)} \left[V_{xx} I_x^2 + V_{yy} I_y^2 + V_{zz} I_z^2 \right] \\ &= \frac{eQV_{zz}}{4I(2I-1)} \left[3I_z^2 - I^2 + \eta (I_x^2 - I_y^2) \right] \\ &= \frac{eQV_{zz}}{4I(2I-1)} \left[3m_I^2 - I(I+1) + \frac{\eta}{2} (I_+^2 + I_-^2) \right] \end{aligned} \tag{25.68}$$

where $\boldsymbol{I}$, $\boldsymbol{I}_x$, $\boldsymbol{I}_y$, $\boldsymbol{I}_z$, $\boldsymbol{I}_+ = \boldsymbol{I}_x + \mathrm{i}\boldsymbol{I}_y$ and $\boldsymbol{I}_- = \boldsymbol{I}_x - \mathrm{i}\boldsymbol{I}_y$ are the nuclear spin operators ($\mathrm{i}^2 = -1$), I and m_I are the quantum numbers belonging to the nuclear spin and its z component, respectively. (The quantity m_I is also called the *magnetic quantum number.*)

In the presence of the quadrupole interaction, represented by the Hamiltonian in Eq. (25.68), the eigenstates of the nucleus will in general be a linear combination of the original orthogonal set of $|I, m_I\rangle$ nuclear states. As $\boldsymbol{H}_{\mathrm{Q}}$ depends on $|m_I|$, the degeneration of the energy levels of the nuclear states $|I,-I\rangle, |I,-I+1\rangle, \ldots, |I, I-I\rangle, |I, I\rangle$ is partly removed by the quadrupole interaction. To find the perturbation of the energy levels of the excited (nuclear spin: I_e) and the ground (nuclear spin: I_g) nuclear states, one has to apply the first-order perturbation theory of degenerate states (see, e.g., Raimes 1961 or textbooks on quantum mechanics). In accordance with this theory, the eigenvalues of the matrices $\langle I_e, m_i|H_Q|I_e, m_j\rangle (m_i, m_j = -I_e \ldots I_e)$ and $\langle I_g, m_i|H_Q|I_g, m_j\rangle (m_i, m_j = -I_g \ldots I_g)$ will provide the energy perturbations of the individual sublevels of the excited state and the ground state, respectively.

As a simple but important example, the energy perturbations of the $I_e = 3/2$ excited state of ^{57}Fe (Fig. 25.9) experiencing quadrupole interaction are calculated below.

For the calculation of the matrix $\langle 3/2, m_i|H_Q|3/2, m_j\rangle$ one has to take into account the effect of the $\boldsymbol{I}_+$ and $\boldsymbol{I}_-$ operators (see Eq. (25.68)) on a $|I, m\rangle$ nuclear state:

$$I_+|I,m\rangle = \sqrt{I(I+1) - m(m+1)}\,|I, m+1\rangle, \tag{25.69}$$

$$I_-|I,m\rangle = \sqrt{I(I+1) - m(m-1)}\,|I, m-1\rangle. \tag{25.70}$$

Fig. 25.9

Quadrupole splitting of the $I = 3/2$ nuclear level and the resulted Mössbauer spectrum. According to Eq. (25.91), Δ is proportional to ΔE_Q

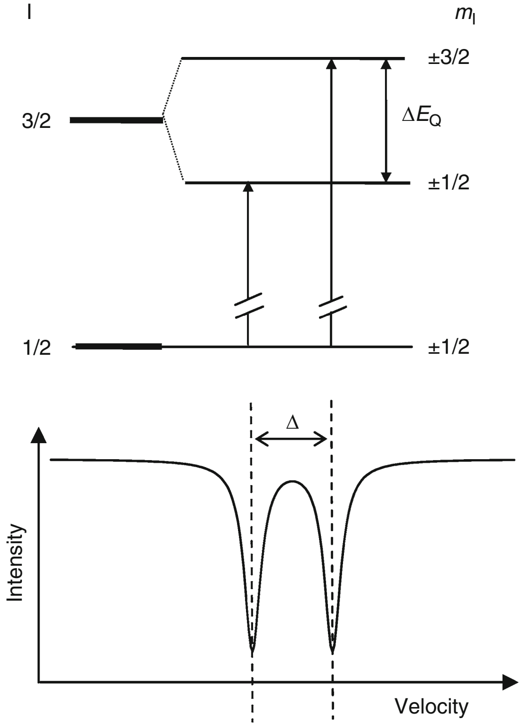

The matrix $\langle 3/2, m_i | H_Q | 3/2, m_j \rangle (m_i, m_j = -3/2 \ldots 3/2)$ will then be equal to

$$\left\langle \frac{3}{2}, m_i \middle| H_Q \middle| \frac{3}{2}, m_j \right\rangle = \frac{eQV_{zz}}{12} \begin{pmatrix} 3 & 0 & \sqrt{3}\eta & 0 \\ 0 & -3 & 0 & \sqrt{3}\eta \\ \sqrt{3}\eta & 0 & -3 & 0 \\ 0 & \sqrt{3}\eta & 0 & 3 \end{pmatrix} \tag{25.71}$$

where increasing row (i) and column (j) numbers correspond to increasing m_i and m_j values, respectively. It can be shown that this matrix has only two different eigenvalues:

$$\lambda_+ = \frac{eQV_{zz}}{4}\sqrt{1+\frac{\eta^2}{3}} \text{ and } \lambda_- = -\frac{eQV_{zz}}{4}\sqrt{1+\frac{\eta^2}{3}}. \tag{25.72}$$

Thus, due to the quadrupole interaction, the $I_e = 3/2$ excited state of ^{57}Fe splits giving rise to two sublevels of different energy.

If the EFG tensor has axial symmetry ($\eta = 0$), then the eigenstates $|I_e, m_e\rangle$ of $\boldsymbol{H}_0$ (see Eq. (25.41)) will also be eigenstates of $\boldsymbol{H}_Q$, and the $I_e = 3/2$ state will split in two energy sublevels with $\lambda_+ = +eQV_{zz}/4$ and $\lambda_- = -eQV_{zz}/4$ for $m_e = \pm 3/2$ and $m_e = \pm 1/2$, respectively (see *Fig. 25.9*, where $\Delta E_Q = |\lambda_+ - \lambda_-|$).

At the same time, the ground state of ^{57}Fe has a nuclear spin characterized by $I_g = 1/2$ for which the quadrupole moment $Q = 0$ (see Sect. 2.2.2.2 in Chap. 2, Vol. 1 as well as Sect. 36.1 of the Appendix of this volume) and therefore the energy of its $m_g = \pm 1/2$ sublevels is not changed by a perturbation of the form described by Eq. (25.68).

For $\eta = 0$, the perturbation of the energy level of a nucleus in the quantum state $|I, m_I\rangle$ can also be given simply by (cf. Eq. (25.68))

$$E_Q = \frac{eQV_{zz}}{4I(2I-1)}\left[3{m_I}^2 - I(I+1)\right]. \tag{25.73}$$

25.1.5.3 Magnetic Dipole Interaction

The nucleus can interact with a magnetic field via its magnetic moment (see Sect. 2.2.2.3 in Chap. 2, Vol. 1). A magnetic flux density, $\boldsymbol{B}$, at the place of the nucleus may be produced by electrons as well as it may be the result of an externally applied magnetic field. The *magnetic hyperfine interaction* can be described by the Hamiltonian

$$H_m = -\boldsymbol{\mu}\boldsymbol{B} = -g_I \mu_N I_z B \tag{25.74}$$

where $\boldsymbol{\mu}$ is the magnetic moment of the nucleus, μ_N is the nuclear magneton ($eh/4\pi m_p = 5.04929 \times 10^{-27}$ Am^2), and g_I is the nuclear giromagnetic factor ($g_I = \mu/(\mu_N I)$) of the nuclear state having a nuclear spin I.

In the presence of magnetic hyperfine interaction, the perturbation of energy levels in the excited and in the ground state of the nucleus can be found similarly to the case of the electric quadruple interaction (see Sect. 25.1.5.2). The case of ^{57}Fe is considered below.

For the $I = 1/2$ ground state of ^{57}Fe the matrix $\langle 1/2, m_i | H_m | 1/2, m_j \rangle (m_i, m_j = -1/2, 1/2)$ has the form

$$\left\langle \frac{1}{2}, m_i \middle| H_m \middle| \frac{1}{2}, m_j \right\rangle = -g_{1/2}\mu_N B \begin{pmatrix} -\frac{1}{2} & 0 \\ 0 & \frac{1}{2} \end{pmatrix}. \tag{25.75}$$

And for the excited state ($I = 3/2$) one obtains (m_i, $m_j = -3/2, -1/2, 1/2, 3/2$)

$$\left\langle \frac{3}{2}, m_i \middle| H_\mathrm{m} \middle| \frac{3}{2}, m_j \right\rangle = -g_{3/2}\mu_\mathrm{N}B \begin{pmatrix} -\frac{3}{2} & 0 & 0 & 0 \\ 0 & -\frac{1}{2} & 0 & 0 \\ 0 & 0 & \frac{1}{2} & 0 \\ 0 & 0 & 0 & \frac{3}{2} \end{pmatrix}. \tag{25.76}$$

As both matrices are diagonal, it is clear that the original orthogonal $|I, m_I\rangle$ states are eigenstates of $\boldsymbol{H}_\mathrm{m}$ and consequently they are also eigenstates of $\boldsymbol{H}_0 + \boldsymbol{H}_\mathrm{m}$ (see Eq. (25.41)). The eigenvalues of the diagonal matrices are simply the elements in the diagonal.

For a nuclear state $|I, m_I\rangle$ the energy perturbation due to magnetic hyperfine interaction is thus given by

$$E_\mathrm{m} = -g_I\mu_\mathrm{N}Bm_I \tag{25.77}$$

where m_I is the magnetic quantum number ($m_I = I, I-1, \ldots, -I$).

As shown also by *Fig. 25.10*, the magnetic field splits the nuclear level of spin I into $2I + 1$ equidistantly spaced non-degenerate sublevels with a separation of $g_I\mu_\mathrm{N}B$ (*nuclear Zeeman effect*).

25.1.5.4 Combined Interactions

In the general case of combined electric quadrupole and magnetic dipole interactions the peak positions can only be calculated numerically.

Fig. 25.10

Magnetic splitting of the I = 3/2 and I = 1/2 nuclear levels (of ^{57}Fe) and the corresponding Mössbauer spectrum. The internal magnetic field (induction, B) is proportional to the distance between any two lines of the sextet; the largest such separation is marked

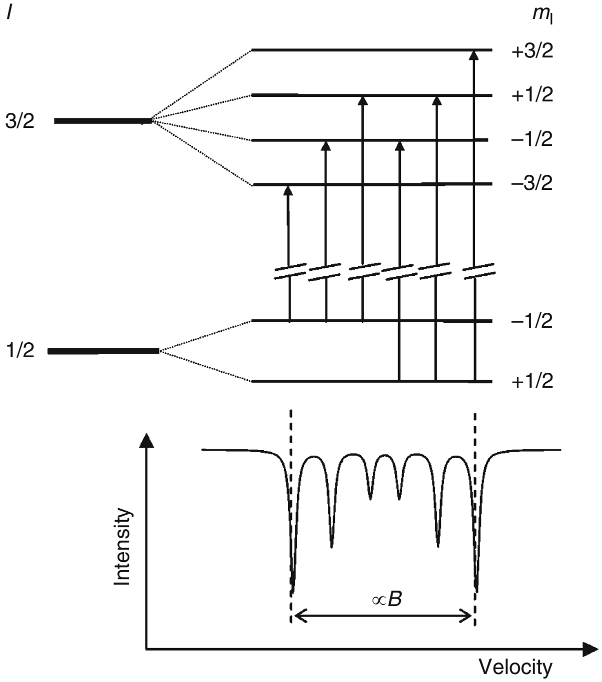

If $|eQV_{zz}| \ll |\mu B|$ first-order perturbation theory may be applied. Let ϑ denote the angle between the z-axis and $\boldsymbol{B}$. If the EFG has axial symmetry, the eigenvalue of the Hamiltonian of the combined interaction is given by

$$E_{\mathrm{mQ}} = -g\mu_{\mathrm{N}}Bm_I + (-1)^{|m_I|+1/2}\frac{eQV_{zz}}{4}\frac{3\cos^2\vartheta - 1}{2}. \tag{25.78}$$

For more complex cases see Matthias et al. (1963).

25.1.5.5 Microenvironment

The term "microenvironment" is of fundamental importance in Mössbauer spectroscopy. It is directly related to the hyperfine interactions sensed by the nucleus. In a solid studied by Mössbauer spectroscopy, there are a large number of nuclei of the Mössbauer isotope. They all sense local hyperfine interactions, which are determined by the product of a nuclear parameter (charge equivalent nuclear radius, R, nuclear quadrupole moment, Q, and nuclear magnetic moment, μ) and a solid-state parameter (electronic density, ρ, electric field gradient represented by V_{zz} and η, and magnetic flux density, $\boldsymbol{B}$) (see Eqs. (25.60), (25.68), and (25.74)).

Normally, the nuclear parameters are the same for all nuclei embedded in a species. However, the solid-state parameters vary from phase to phase in a multiphase species, or may vary within the phase from site to site where the environment of the Mössbauer atom is different. Consequently, there may be assemblies of nuclei sensing different hyperfine interactions in a solid, in general. The microenvironment is a convenient term for the classification of local environments surrounding the Mössbauer atoms. The local environments of two Mössbauer atoms represent the same microenvironment if those atoms experience the same hyperfine interactions there. The correspondence between the microenvironment and hyperfine interactions gives a basis for the analytical use of Mössbauer spectroscopy (see Sect. 25.3).

25.2 Mössbauer Parameters

25.2.1 Isomer Shift

The isomer shift, denoted by δ, is the most often quoted Mössbauer parameter. It is a peak shift that consists of two terms:

$$\delta = \delta_{\mathrm{c}} + \delta_{\mathrm{SOD}} \tag{25.79}$$

where the first term is the chemical isomer shift δ_{c} (already mentioned in Sect. 25.1.5.1) and the second term is the second-order Doppler shift (also called temperature shift). The isomer shift, δ, is measured in velocity units for which the suggested decimal submultiple SI unit is mm/s.

25.2.1.1 Chemical Isomer Shift

The chemical isomer shift, δ_{c} (measured as Doppler velocity in mm/s units), is related to the electric monopole hyperfine interaction between the nucleus and the electrons. The nuclear energy levels will be shifted as a result of this interaction (see *Fig. 25.8*, Sect. 25.1.5.1).

To measure this energy shift in the Mössbauer experiment one should modify the energy of the emitted γ ray by moving the source relative to the absorber by an appropriate Doppler velocity in order to bring the energy of the emitted γ ray into coincidence with the absorption energy in the absorber, when one actually measures the chemical isomer shift.

With the notation introduced in Sect. 25.1.5.1, δ_c can be defined as the Doppler velocity corresponding to the energy shift ΔE_{IS} (see Eq. (25.60)):

$$\delta_c = \frac{c}{E_0} \Delta E_{IS}. \tag{25.80}$$

The name *chemical* isomer shift is related to the fact that the electron density at the place of the nucleus is strongly influenced by the valence state and the chemical bonding of the Mössbauer atom.

The expressions for the chemical isomer shift can be derived by substituting ΔE_{IS} (see Eqs. (25.60), (25.62), and (25.64)) into the formula of δ_c (25.80).

All expressions presently used for evaluation of isomer shifts neglect the polarization effects (see Eqs. (25.49) and (25.50)). This introduces an error less than 5%.

By treating the electron density relativistically, the isomer shift can be given by combining Eqs. (25.64) and (25.80) to give

$$\delta_c = C \Delta\rho_e(0) \left[\Delta\langle r^2 \rangle - b_4 \Delta\langle r^4 \rangle + b_6 \Delta\langle r^6 \rangle \right] \tag{25.81}$$

where $C = (2/3)\pi Z e^2 c / E_0$, $\Delta\rho_e(0) = \rho_e^A(0) - \rho_e^S(0)$, $\Delta\langle r^m \rangle = \langle r^m \rangle_e - \langle r^m \rangle_g$, and b_4 and b_6 are constants that depend on Z.

In most cases, the terms with order higher than $m = 2$ can be neglected. In this way, one obtains the expression for the chemical isomer shift, which is recommended for general use

$$\delta_c = C \Delta\rho_e(0) \Delta\langle r^2 \rangle \tag{25.82}$$

where with the choice $C = 90.42 Z/(E_0/\text{keV})$ and measuring $\Delta\langle r^2 \rangle$ in fm^2 and $\Delta\rho(0)$ in $10^{26}\ \text{cm}^{-3}$ units, δ_c is obtained in units of mm/s.

The error of using this formula instead of the previous one (Eq. (25.81)) is about 1% to 10%. (The error increases with the mass of the atom.)

By introducing the charge equivalent radius R (see Eq. (25.59)) and by expressing the nuclear parameter as the relative change of this radius one obtains

$$\delta_c = C \Delta\rho_e(0) \frac{\Delta R}{R} \tag{25.83}$$

with $C = (4/5)\pi Z e^2 c (1.2 A^{1/3})^2 / E_0 = 156.24 Z A^{2/3} / E_0$.

The additional error is of the order of a few percentage. This expression has found the most widespread application in the solid state and chemical literature.

If only nonrelativistic electron densities are available a correction by a multiplication factor $S'(Z)$ has to be applied (Eq. (25.62)) and the expression for the chemical isomer shift will be

$$\delta_c = C \Delta|\psi(0)|^2 S'(Z) \frac{\Delta R}{R} \tag{25.84}$$

where $|\psi(0)|^2$ denotes the nonrelativistic s electron density at the place of the nucleus. This is the most commonly used formula of the chemical isomer shift for applications in chemistry.

In the case of ^{57}Fe and ^{119}Sn (which are the most frequently used Mössbauer nuclides), the evaluation of the chemical isomer shift is often performed by using a so-called isomer shift calibration constant, α or α', especially in the chemical literature. With the help of these calibration constants, the following expressions can be obtained for the chemical isomer shift:

$$\delta_c = \alpha' \Delta \rho(0) \text{ and } \delta_c = \alpha \Delta |\psi(0)|^2. \tag{25.85}$$

In most chemical applications of Mössbauer spectroscopy, Eq. (25.84) is used. Consequently, from the chemical isomer shift, the charge equivalent nuclear radius (R) and the electron density can be determined. Any of the two can be obtained from a Mössbauer measurement if the other one is determined independently. In most chemical applications, the goal is the determination of the shift in electron density.

In practice, the chemical isomer shift is usually given relative to a standard reference material. In ^{57}Fe Mössbauer spectroscopy, α-Fe has become the most commonly used standard reference material.

25.2.1.2 Second-Order Doppler Shift

The second-order Doppler shift, δ_{SOD}, which is often called *temperature shift*, is a peak shift related to the relativistic Doppler effect originating from the thermal motion of the nuclei. If the Mössbauer atom has a speed u, and moves in a direction making angle α with the direction of the γ ray it emits, then the v frequency of the emitted γ ray will differ from the v_0 frequency it had if the atom had been at rest. The v frequency is related to v_0 in the following way:

$$v = v_0 \frac{\sqrt{1 - \frac{u^2}{c^2}}}{1 - \frac{u}{c}\cos\alpha}. \tag{25.86}$$

As atoms in a solid perform an oscillatory motion with a period in the order of around 10^{-13} s, during the lifetime of the excited state of the Mössbauer nucleus (for the case of ^{57}Fe, e.g., $\tau \approx 10^{-7}$ s) the corresponding atom goes through approximately a million of cycles. As a result, only the time-average of the relativistic Doppler effect can be detected in the Mössbauer spectra. Taking into account that $u \ll c$, time averaging the right-hand side of Eq. (25.86) yields the following equation for the mean frequency of the emitted γ photon (Pound and Rebka 1960):

$$v \approx v_0 \left(1 - \frac{1}{2}\frac{\langle u^2 \rangle}{c^2}\right), \tag{25.87}$$

i.e., the Doppler effect arising because of the oscillatory motion of atoms in a solid influences the frequency of the emitted γ ray only in the second order of the speed of the atoms.

The corresponding energy shift of the γ ray can be calculated as

$$\Delta E_{\mathrm{SOD}} = h(v - v_0) = -\frac{hv_0}{2}\frac{\langle u^2 \rangle}{c^2} = -\frac{1}{2}\frac{\langle u^2 \rangle}{c^2} E_\gamma \tag{25.88}$$

In the Mössbauer spectrum, the *second-order Doppler shift* is measured as a peak shift in velocity units:

$$\delta_{\mathrm{SOD}} = -\frac{1}{2}\frac{\langle u^2 \rangle}{c}. \tag{25.89}$$

From Eq. (25.23) it follows that δ_{SOD} decreases with increasing temperature.

25.2.2 Quadrupole Splitting

The quadrupole splitting, Δ, is the Mössbauer parameter, which is related to the electric quadrupole hyperfine interaction between the nucleus and the electrons (see Sect. 25.1.5.2).

In the case of ^{57}Fe and ^{119}Sn, e.g., where the Mössbauer transition occurs between nuclear levels with excited state spin $I_e = 3/2$ and ground state spin $I_g = 1/2$, in the presence of hyperfine quadrupole interaction, the excited state will be split into two sublevels (see Eq. (25.72) and *Fig. 25.9*). Resonance absorption can occur between the unsplit ground state and both sublevels of the split-excited state. By performing a Mössbauer measurement (see *Fig. 25.5*) one can detect both of the corresponding absorption peaks. The distance between the two peaks, measured in Doppler velocity units as usual in Mössbauer spectroscopy, is called the *quadrupole splitting* Δ. Thus, the quadrupole splitting is proportional to the energy separation (also called the quadrupole splitting energy, ΔE_Q) between the two sublevels of the split-excited state:

$$\Delta \propto \Delta E_Q = \lambda_+ - \lambda_- = \frac{eQV_{zz}}{2}\sqrt{1+\frac{\eta^2}{3}} \tag{25.90}$$

where λ_+ and λ_- have been defined in Eq. (25.72). The proportionality constant connecting Δ with ΔE_Q depends on the energy of the γ ray (E_0, see *Fig. 25.1*) emitted by the source in a recoilless emission event:

$$\Delta = \frac{c}{E_0}\Delta E_Q. \tag{25.91}$$

The two absorption peaks, appearing in the measured Mössbauer spectrum as a consequence of electric quadrupole hyperfine interaction, are called a *doublet.*

As can be seen from Eq. (25.90), in the case of a 3/2 → 1/2 transition, solely from the knowledge of Δ it is not possible to determine V_{zz} and η independently or to find out the sign of the V_{zz}. It is possible, however, to determine these parameters of the electric field gradient from the angular dependence of the intensity of the peaks when a single crystal is measured. The sign of the V_{zz} can be determined if in addition to electric quadrupole interaction the Mössbauer nuclei experience hyperfine magnetic interaction as well (see *Fig. 25.12*).

The connection between the quadrupole splitting energy and the separation of the absorption lines is less obvious if in addition to the excited state, the ground nuclear state is also subject to hyperfine quadrupole interaction. This is the case, e.g., for ^{129}I where the Mössbauer transition occurs between the excited state with $I_e = 5/2$ and the ground state with $I_g = 7/2$. The quadrupole splittings of this transition are treated below by assuming that the asymmetry parameter of the EFG is zero ($\eta = 0$, see Eqs. (25.68) and (25.73)).

In this case, altogether five quadrupole splittings ($\Delta_1 \ldots \Delta_5$) can be observed (see *Fig. 25.11*). In the excited state the ratio between the splittings $\Delta_1/\Delta_2 = 1/2$, while in the ground state $\Delta_3{:}\Delta_4{:}\Delta_5 = 1{:}2{:}3$, as can be calculated from Eq. (25.92).

The selection rules for a magnetic dipole (M1) electromagnetic (EM) transition ($\Delta m_I = 0, \pm 1$) allow eight transitions, which result in eight Mössbauer peaks in the spectrum. The positions of the individual peaks (relative to the isomer shift) can be given by

$$\delta_{ij} = \frac{ceV_{zz}Q_g}{4E_0}\left[\frac{Q_e}{Q_g}C(I^e, m_{I_j}^e) - C(I^g, m_{I_i}^g)\right], \quad \text{where } C(I, m_I) = \frac{3{m_I}^2 - I(I+1)}{I(2I-1)} \tag{25.92}$$

where Q_e and Q_g are the quadrupole moments of the excited state and the ground state, respectively (Hafemeister 1971).

Fig. 25.11

Quadrupole splitting of the *I* = 5/2 (excited state) and *I* = 7/2 (ground state) nuclear levels of ^{129}I. The relative intensities of the allowed transitions indicated are (from the left to the right): 1:6:21:3:10:15:18:10 (May 1971). Note that the *I* = 7/2 levels are indeed lower than the *I* = 5/2 levels in this particular case

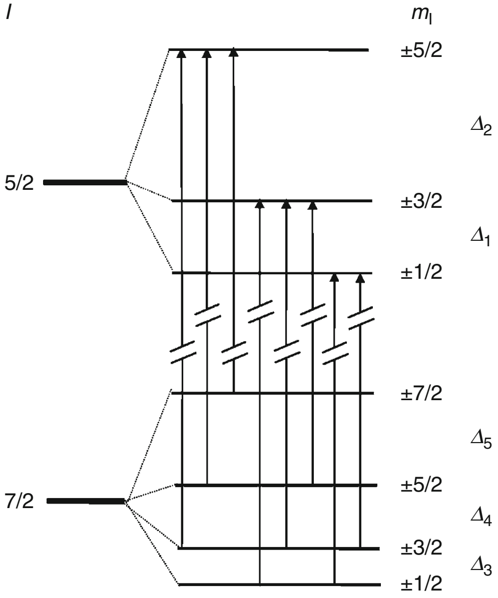

From the measured quadrupole splitting, either the nuclear quadrupole moment or the electric field gradient can be determined. Any of the two can be obtained from a Mössbauer measurement if the other can be determined independently. In chemical applications, the determination of the electric field gradient is the goal.

In many cases, not V_{zz} but eQV_{zz} is derived from the measured quadrupole splitting either in velocity or in frequency units. *Table 25.1* shows the corresponding conversion factors for some Mössbauer nuclides.

25.2.3 Magnetic Splitting

The magnetic splitting Δ_{m} is related to the hyperfine magnetic interaction (see Sect. 25.1.5.3).

As shown by Eq. (25.77), the energy levels produced by the nuclear Zeeman splitting can be expressed as a product containing the nuclear magnetic moment $\boldsymbol{\mu}$ and the *magnetic flux density*, ***B***, existing at the site of the nucleus.

The magnetic splitting energy ΔE_{m} means the energy difference between the adjacent Zeeman split sublevels of a nuclear level. Its value derived from Eq. (25.77) is

$$\Delta E_{\mathrm{m}} = -g_I \mu_{\mathrm{N}} B \Delta m_I = -g_I \mu_{\mathrm{N}} B \qquad (25.93)$$

Note that the ΔE_{m} magnetic splitting energy in the excited state is different from that in the ground state.

Table 25.1

Numerical factors that can be used to obtain the value of eQV_{zz} in mm s^{-1} or in MHz units from the value of V_{zz}. In the case of 3/2 ⟶ 1/2 transitions (^{57}Fe, ^{119}Sn, ^{125}Te) the conversion factors are calculated with Q referring to the quadrupole moment of the excited nuclear state. For the other nuclides, Q refers to the quadrupole moment of the ground state. The precision of the given numerical factors is limited by the uncertainty of the respective Q values

Mössbauer nuclide ($I_e \longrightarrow I_g$)	In order to obtain eQV_{zz} in mm s^{-1} units, $V_{zz}/(10^{21}$ V/m$^2)$ should be multiplied by	In order to obtain eQV_{zz} in MHz units, $V_{zz}/(10^{21}$ V/m$^2)$ should be multiplied by
^{57}Fe (3/2 → 1/2)	+0.333(2)	+3.87(2)
^{119}Sn (3/2 → 1/2)	−0.166(1)	−3.19(2)
^{125}Te (3/2 → 1/2)	−0.262(17)	−7.5(5)
^{151}Eu (7/2 → 5/2)	+1.257(14)	+21.83(24)
^{121}Sb (7/2 → 5/2)	−0.438(9)	−13.13(27)
^{141}Pr (7/2 → 5/2)	−0.0122(8)	−1.43(10)
^{129}I (5/2 → 7/2)	−0.537(8)	−12.04(17)
^{237}Np (5/2 → 5/2)	+1.957(3)	+93.96(15)
^{161}Dy (5/2 → 5/2)	+2.930(23)	+60.62(48)
^{197}Au (1/2 → 3/2)	+0.212(6)	+13.23(39)

For a transition between nuclear levels with nuclear spin $I_g = 1/2$ and $I_e = 3/2$, due to hyperfine magnetic interaction, the excited state splits into four sublevels with $m_{3/2} = -3/2$, $-1/2$, $+1/2$, and $+3/2$, while the ground state splits into two sublevels with $m_{1/2} = +1/2, -1/2$, as illustrated in *Fig. 25.10*. According to the selection rule that applies to M1 electromagnetic transitions ($\Delta m_I = 0, \pm 1$), there are six allowed transitions in this case. This results in a six-peak pattern called sextet in the Mössbauer spectrum. The magnetic splitting of the excited state can be determined from the peak separation of the first and second or of the second and third peaks as well as from that of the fourth and fifth or of the fifth and sixth peaks (see *Fig. 25.10*). The magnetic splitting of the ground state can be obtained from the peak separation of the second and fourth or of the third and fifth peaks. The peak separation and, consequently, the *magnetic splitting* $\varDelta_m$ is measured as a Doppler velocity, in mm/s unit:

$$\varDelta_{\mathrm{m}} = \Delta E_{\mathrm{m}} \frac{c}{E_0} . \tag{25.94}$$

For the chemical application of Mössbauer spectroscopy, it is not necessary to derive the magnetic splitting explicitly from the Mössbauer spectrum in order to determine the magnetic flux density. As the separation of any two of the peaks in a *magnetic sextet* is also proportional to the magnetic flux density sensed by the corresponding nuclei, the basis of the determination of B is usually the separation of the two outermost peaks of the spectrum.

For a transition between nuclear levels with higher nuclear spin values, the magnetic field results in a more complex peak pattern in the Mössbauer spectrum. In the case of ^{151}Eu, e.g., the Mössbauer transition occurs between the $I_g = 5/2$ and $I_e = 7/2$ nuclear levels, and in the presence of magnetic splitting the Mössbauer spectrum consists of 18 peaks (Greenwood and

Gibb 1971). The separation of the peaks will also be proportional to the corresponding magnetic flux density.

In many cases the hyperfine magnetic dipole interaction occurs together with the electric quadrupole interaction. As shown in *Fig. 25.12* for the transition $I = 1/2 \rightarrow 3/2$, when $H_Q \ll H_m$, the sublevels of the excited state are no longer equally spaced, but the $m_I = +3/2$ and $m_I = -3/2$ sublevels are raised while the $m_I = +1/2$ and $m_I = -1/2$ sublevels are lowered when $V_{zz} > 0$. (Note that if $V_{zz} > 0$ and $\eta \neq 0$, the eigenstates of $\boldsymbol{H} = \boldsymbol{H}_0 + \boldsymbol{H}_C + \boldsymbol{H}_m$ (i.e., $|I, m_I\rangle$) will no longer be eigenstates of $\boldsymbol{H}' = \boldsymbol{H}_0 + \boldsymbol{H}_C + \boldsymbol{H}_m + \boldsymbol{H}_Q$ – see Eqs. (25.41) and (25.68–25.70) – and therefore the sublevels shifted higher or lower than those belonging to the case $\boldsymbol{H}_Q = 0$ will no longer represent pure $|I, m_I\rangle$ states but linear combinations of several $|I, m_I\rangle$ states as mentioned in Sect. 25.1.5.2.) In the corresponding Mössbauer spectrum, the separation between the centers of the outermost two and of the inner four peaks will be proportional to the quadrupole splitting. From the position of these centers relative to each other, the sign of V_{zz} can be determined. The energies of the individual nuclear sublevels are given by Eq. (25.78) in this case.

Fig. 25.12

Energy shift and magnetic splitting of the $I = 1/2$ and $I = 3/2$ levels in the presence of an electric field gradient with $\eta = 0$, and the corresponding Mössbauer spectrum ($V_{zz} > 0$). Note that due to quadrupole interaction, the symmetry center of the outmost peaks is shifted relative to the inner four peaks in contrast to *Fig. 25.10*

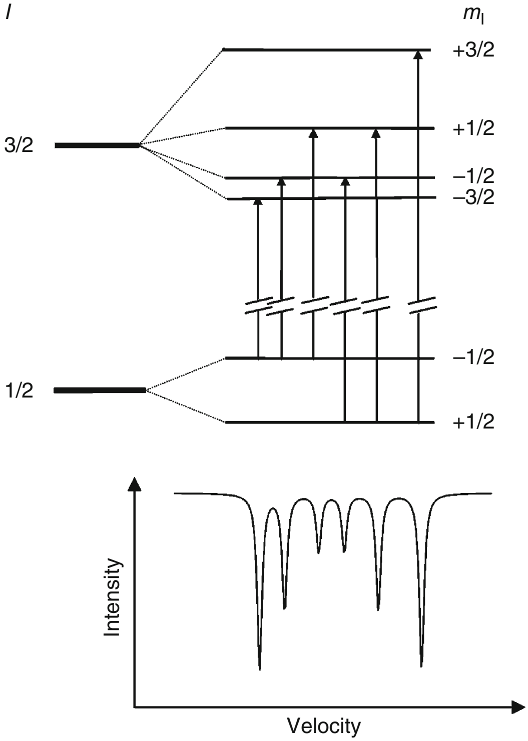

25.2.4 Peak Intensity

If no splitting of the nuclear levels occurs, then the Mössbauer peak intensity can be given by Eq. (25.31).

In the case of the electric quadrupole and magnetic dipole interactions, the individual peaks have characteristic intensities relative to each other, which can confirm the assignment of the peaks to the appropriate nuclear transitions, and, in addition to the information provided by δ, $\varDelta$, and $\varDelta_{\mathrm{m}}$, it helps assigning the various subspectra of the Mössbauer spectrum to lattice sites. The relative intensities can also furnish information on the orientational relationships in the sample/lattice (Schatz et al. 1996).

The relative intensity of a peak is proportional to the *relative* probability of the corresponding nuclear transition. For the *probability of a transition* from a state $|I_{\mathrm{e}}, m_{\mathrm{e}}\rangle$ to the state $|I_{\mathrm{g}}, m_{\mathrm{g}}\rangle$ by electromagnetic (EM) multipole radiation of σl (where σ = E for electric and σ = M for magnetic multipole character, and 2^l is the multipolarity of the radiation, see Sect. 2.3.2.2 in Chap. 2, Vol. 1) one can write

$$p(I_{\mathrm{g}}, m_{\mathrm{g}}, M_l^{\sigma}, I_{\mathrm{e}}, m_{\mathrm{e}}) \propto \left|\langle I_{\mathrm{g}}, m_{\mathrm{g}}|M_{l,m}^{\sigma}|I_{\mathrm{e}}, m_{\mathrm{e}}\rangle\right|^2 \tag{25.95}$$

where $M_{l,m}^{\sigma}$ is the multipole operator (for more details see, e.g., Blatt and Weisskopf (1959) or Mayer-Kuckuk (1994)) corresponding to the multipole radiation σl that carries away an angular momentum of $l\hbar$ with a z component of $m\hbar$.

According to the Wigner–Eckart theory (see, e.g., Rotenberg et al. 1959)

$$\langle I_{\mathrm{g}}, m_{\mathrm{g}}|M_{l,m}^{\sigma}|I_{\mathrm{e}}, m_{\mathrm{e}}\rangle = (-1)^{I_{\mathrm{g}}-m_{\mathrm{g}}} \begin{pmatrix} I_{\mathrm{g}} & l & I_{\mathrm{e}} \\ -m_{\mathrm{g}} & m & m_{\mathrm{e}} \end{pmatrix} \langle I_{\mathrm{g}}|M_l^{\sigma}|I_{\mathrm{e}}\rangle \tag{25.96}$$

where the term $\langle I_{\mathrm{g}}|M_l^{\sigma}|I_{\mathrm{e}}\rangle$ (called the *reduced matrix element*) does not depend on m_{g}, m_{e}, and m. Consequently, it has the same value for all of the transitions occurring via σl multipole radiation between the excited state and ground state of the nucleus.

As it is only the *relative* value of probabilities of $|I_{\mathrm{e}}, m_{\mathrm{e}}\rangle \to |I_{\mathrm{g}}, m_{\mathrm{g}}\rangle$ nuclear transitions ($m_{\mathrm{e}} = -I_{\mathrm{e}} \ldots I_{\mathrm{e}}$, $m_{\mathrm{g}} = -I_{\mathrm{g}} \ldots I_{\mathrm{g}}$) that can be detected in a Mössbauer measurement, for the probability of a certain $|I_{\mathrm{e}}, m_{\mathrm{e}}\rangle \to |I_{\mathrm{g}}, m_{\mathrm{g}}\rangle$ transition via σl multipole radiation one can write

$$p(I_{\mathrm{g}}, m_{\mathrm{g}}, M_l^{\sigma}, I_{\mathrm{e}}, m_{\mathrm{e}}) \propto \begin{pmatrix} I_{\mathrm{g}} & l & I_{\mathrm{e}} \\ -m_{\mathrm{g}} & m & m_{\mathrm{e}} \end{pmatrix}^2 \tag{25.97}$$

where the term on the right side is the so-called "3j symbol" (see, e.g., Lindner (1984) and Weisstein (2010)). The 3j symbols are closely related to the so-called Clebsch–Gordan coefficients. There are numerous Web sites on the Internet where automatic calculators are available for the calculation of 3j symbols as a function of I_{g}, I_{e}, l, m_{g}, m_{e}, and m.

The square of 3j symbol values entering the calculations in the case of the Mössbauer transition of ^{57}Fe ($I_{\mathrm{e}} = 3/2$, $I_{\mathrm{g}} = 1/2$, $\sigma\, l =$ M1) are the following:

$$\begin{pmatrix} 1/2 & 1 & 3/2 \\ \pm 1/2 & \pm 1 & \mp 3/2 \end{pmatrix}^2 = \frac{1}{4}, \quad \begin{pmatrix} 1/2 & 1 & 3/2 \\ \pm 1/2 & 0 & \mp 1/2 \end{pmatrix}^2 = \frac{1}{6}, \quad \begin{pmatrix} 1/2 & 1 & 3/2 \\ \pm 1/2 & \mp 1 & \pm 1/2 \end{pmatrix}^2 = \frac{1}{12}. \tag{25.98}$$

To calculate the relative intensities of absorption lines in a Mössbauer spectrum, one also has to take into account that the intensity of the emitted multipole radiation is not isotropic but has a certain angular dependence $F_{lm}(\theta)$ where θ is the polar angle that the direction of observation encloses with the z-axis of the principal axis system (defined, e.g., by the direction of the hyperfine magnetic field). It follows that the relative intensity of the peak belonging to the transition $|I_\mathrm{e}, m_\mathrm{e}\rangle \rightarrow |I_\mathrm{g}, m_\mathrm{g}\rangle$ can be expressed as

$$I(I_\mathrm{e}, m_\mathrm{e}, I_\mathrm{g}, m_\mathrm{g}, \sigma lm) \propto \begin{pmatrix} I_\mathrm{g} & l & I_\mathrm{e} \\ -m_\mathrm{g} & m & m_\mathrm{e} \end{pmatrix}^2 F_{lm}(\theta). \tag{25.99}$$

For the case of 3/2 → 1/2 magnetic dipole transitions, the angular dependence of the relative peak intensities are tabulated in *Table 25.2* together with corresponding values of $3j$ symbol squares.

For an isotropic distribution of $\boldsymbol{B}$ (e.g., when a powder sample without texture is measured), the term $F_{lm}(\theta)$ describing the angular dependence of the intensity of multipole radiation can be integrated to give a factor of 1 for all the values of m. This means that in the case of powdered samples (and in the absence of additional effects, see Sect. 25.2.7.5) the relative intensity of the Mössbauer peaks is determined only by the values of $3j$ symbol squares. For 3/2 → 1/2 magnetic dipole transitions, in the case of magnetic splitting this results in a sextet with relative peak intensities of 3:2:1:1:2:3, while in the case of electric quadrupole interaction, assuming an isotropic distribution of the z direction of the EFG's PAS (principal axis system) in this case, a doublet with relative peak intensities of 1:1 is obtained.

The determination of peak intensities becomes a more complicated issue in the case of combined hyperfine magnetic dipole and electric quadrupole interactions (for the case of ^{57}Fe see, e.g., Kündig (1967) and Housley et al. (1969)), or when the Mössbauer transition has a mixed (most often M1 + E2) multipole character (for the case of ^{99}Ru see, e.g., Foyt et al. (1975)). Further factors influencing the relative peak intensities will be discussed in Sect. 25.2.7.5.

25.2.5 The *f*-Factor

The f-factor, also called the Mössbauer–Lamb factor, is not only a measure of the probability of recoilless resonance emission/absorption of γ photons as discussed in Sect. 25.1.3.3, but it is

Table 25.2

$3j$ symbols and angular dependent terms determining the relative intensities of peaks in the case of a magnetic dipole transition occurring between nuclear levels with nuclear spins I = 3/2 and I = 1/2 (which is the case for, e.g., ^{57}Fe and ^{119}Sn)

			Square of corresponding $3j$ symbol	Angular dependence of intensity
$m_{3/2}$	$m_{1/2}$	m	$\begin{pmatrix} 1/2 & 1 & 3/2 \\ -m_{1/2} & m & m_{3/2} \end{pmatrix}^2$	$F_{lm}(\theta)$ (l = 1)
3/2	1/2	−1	$\frac{3}{12}$	$\frac{3}{8}(1+\cos^2\theta)$
1/2	1/2	0	$\frac{2}{12}$	$\frac{3}{4}\sin^2\theta$
−1/2	1/2	1	$\frac{1}{12}$	$\frac{3}{8}(1+\cos^2\theta)$
−3/2	1/2	2	Not allowed	
3/2	−1/2	−2	Not allowed	
1/2	−1/2	−1	$\frac{1}{12}$	$\frac{3}{8}(1+\cos^2\theta)$
−1/2	−1/2	0	$\frac{2}{12}$	$\frac{3}{4}\sin^2\theta$
−3/2	−1/2	1	$\frac{3}{12}$	$\frac{3}{8}(1+\cos^2\theta)$

an important Mössbauer parameter, which can be obtained from the measurement of Mössbauer spectra. The f-factor is defined as the number of recoilless γ events (emission or absorption) divided by the total number of γ events. Since it can be expressed as a function of the mean square displacement, $\langle x^2 \rangle$, of the Mössbauer atom "frozen" in the lattice, (see Eq. (25.24)), it is possible to get important information from the f-factor about the state of lattice vibrations (e.g., to determine the Debye temperature from its temperature dependence).

The Mössbauer–Lamb factors f_S (for the source) and f_A (for the absorber) show up as coefficients to determine the Mössbauer peak intensity (see Eq. (25.31) for the transmission integral). Unfortunately, it is difficult to determine the absolute values of f_S and f_A from the absorption intensity without tedious and difficult experimentation.

The so-called black absorber method may be used for the determination of f_S. This uses the saturation effect of f_S when the effective thickness, τ_A (see Eq. (25.30)), approaches infinity. In this case, the asymptotic form of the spectral peak amplitude can be used to obtain f_S. The measurement of the f-factor of the absorber, f_A, is based on Eq. (25.33) and the corresponding nonlinear dependence of the intensity, amplitude, and width of the Mössbauer spectrum peak on the effective thickness (see later in *Fig. 25.17*). This latter is the so-called *blackness effect*. For the determination of f_A, the peak intensity and the peak amplitude should be measured for at least two absorbers of different thicknesses (Vértes and Nagy 1990).

When the Mössbauer nuclides are in different microenvironments, the determination of the relative values of the Mössbauer–Lamb factors belonging to each microenvironment is necessary in order to obtain the correct relative molar quantities.

25.2.6 Peak Width

The Mössbauer peak is characterized by an experimental parameter, the peak width W, which is measured as the full width at half maximum of the peak.

The peak width W for Lorentzian peaks can be derived from Eq. (25.31) (Margulies and Ehrman 1961) as a function of the absorber thickness:

$$W = W_0 \tau \frac{\exp\left(-\frac{\tau}{2}\right) I_0\left(-\frac{\tau}{2}\right) + I_1\left(-\frac{\tau}{2}\right)}{1 - \exp\left(-\frac{\tau}{2}\right) I_0\left(-\frac{\tau}{2}\right)}, \tag{25.100}$$

where $W_0 = 2\Gamma$, and Γ is the natural line width of the given Mössbauer transition. I_0 and I_1 denote the modified Bessel functions (see, e.g., BESSEL 2003) of the first kind (also referred to as having imaginary argument), and τ is the effective thickness of the absorber (which is proportional to the actual surface density d measured in mg/cm^2, see Eq. (25.30)).

In the case of an ideally thin absorber, the Mössbauer peak width is twice of the natural line width ($W_0 = 2\Gamma$), which gives a possibility to determine the lifetime of the excited states of the Mössbauer nuclei on the basis of Eq. (25.2).

It is possible to observe Mössbauer peak widths narrower than W_0 without violating the uncertainty principle. This can happen, e.g., if γ photons from a nuclear decay are selected in such a way that only those are counted, which are emitted after a certain time of the "birth" of the excited state (*time-dependent Mössbauer spectroscopy*).

Deviations from the expected peak width may arise due to various effects. A number of inherent physical processes cause peak broadening (like diffusion, relaxation processes) and, consequently, a lot of useful information can be obtained from the peak width W.

25.2.7 Mössbauer Parameters and Experimental Parameters

As it was just seen, the main *Mössbauer parameters* that can be derived from a Mössbauer spectrum are as follows: Mössbauer–Lamb factor (f), isomer shift (δ), quadrupole splitting (Δ), magnetic splitting (Δ_m), peak width (W), and the relative area – also called the relative intensity – of the spectrum peaks (A). Sometimes, it is convenient to consider these parameters as the coordinates of the Mössbauer parameter vector $\boldsymbol{P}_M$:

$$\boldsymbol{P}_M = (f, \delta, \Delta, \Delta_m, W, A), \tag{25.101}$$

where the individual symbols between the parentheses may again represent sets of similar parameters (i.e., vectors).

For instance, instead of A one might write $\boldsymbol{A}$ meaning:

$$A = (A_1, A_2, \ldots), \tag{25.102}$$

where A_1, A_2,... represent the spectral areas of different peaks.

The Mössbauer parameters depend on a number of various *experimental parameters* such as temperature (T), pressure (p), external magnetic flux density ($\boldsymbol{B}_{ext}$) if any, the polar angles of the sample relative to the direction of the γ rays (θ, ϕ), the frequency (v) of high-frequency field if any, etc.:

$$\boldsymbol{P}_M = f(P_{exp}), \tag{25.103}$$

where the vector $\boldsymbol{P}_{exp}$ represents all of the relevant experimental parameters:

$$\boldsymbol{P}_{exp} = (T, p, B_{ext}, \theta, \phi, v, c, \ldots) \tag{25.104}$$

in which the c concentration of the Mössbauer species in the sample is also included.

Some of the above-listed experimental parameters may have *standard values*. For instance, T_0 = 293 K (room temperature, RT), p_0 = 1 bar (~ atmospheric pressure), $\boldsymbol{B}_{ext,0}$ = 0 T (no external magnetic field applied), etc. The measuring conditions specified by such values are called *standard conditions*.

25.2.7.1 Temperature Dependence

The temperature dependence of Mössbauer parameters can be very useful in qualitative analysis. As the temperature dependence of the different spectrum components is usually different, measuring the same sample at different temperatures may help distinguish between species whose "fingerprints" are similar under standard conditions (i.e., at room temperature in the given instance) but different at lower or higher temperatures.

The temperature dependence of the isomer shift (see *Fig. 25.13*) is mainly determined by that of the second-order Doppler shift and can be obtained by combining Eqs. (25.89) and (25.23):

$$\delta_{SOD}(T) = -\frac{9k\theta_D}{2cM}\left[\frac{1}{8} + \left(\frac{T}{\theta_D}\right)^4 \int_0^{\theta_D/T} \frac{x^3}{e^x - 1}\,dx\right]. \tag{25.105}$$

The temperature dependence of the quadrupole splitting comes mainly from the temperature-dependent population of the different valence levels of the Mössbauer nuclide, provided that

Fig. 25.13

Temperature dependence of the isomer shift of ^{119}Sn in $V_3Ga_{0.1}Sn_{0.9}$, based on the results of Kimball et al. (1974)

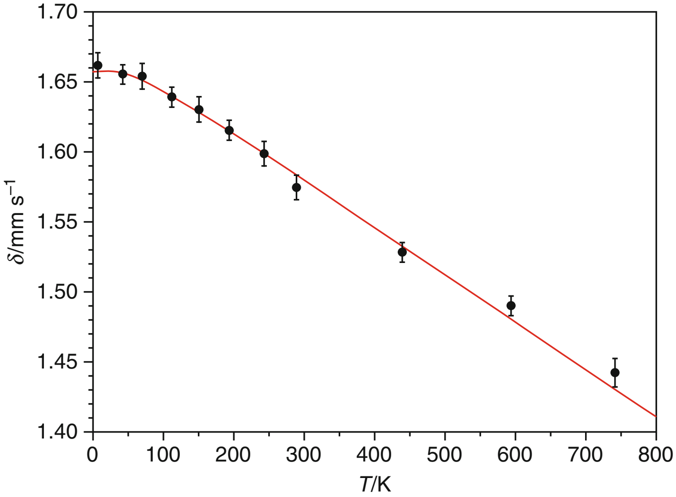

the valence contribution to the electric field gradient is not negligible (Ingalls 1964; Eicher and Trautwein 1969; Gütlich et al. 1978).

In the case of ^{57}Fe one has

$$\Delta(T) = \frac{2}{7} e^2 Q \frac{c}{E_\gamma} (1 - R) \langle r^{-3} \rangle \alpha^2 F(E_i, \alpha^2 \lambda_0, T) \tag{25.106}$$

where the temperature sensitive factor F depends on the energy separation of the 3d levels E_i, on the isotropic covalency factor α^2, and on the free-ion spin-orbit coupling constant λ_0. $\langle r^{-3} \rangle$ means the expectation value of r^{-3}, and R is the antishielding *Sternheimer factor* (Sternheimer 1950, 1951, 1963).

The temperature dependence of quadrupole splitting is illustrated in *Fig. 25.14* for $Cd_3[Fe(CN)_6]_2$.

The temperature dependence of the Mössbauer–Lamb factor (see *Fig. 25.15*) can be calculated in the frame of the Debye model of solids from Eq. (25.26). For different temperature regions, the following formulae can be derived (cf. Eqs. (25.20)–(25.22) and (25.24)):

$$f(T) \approx \exp\left\{ -\frac{6E_R}{k\theta_D} \left(\frac{1}{4} + \left(\frac{T}{\theta_D} \right)^2 \frac{\pi^2}{6} \right) \right\}, \quad \text{if } T \ll \theta_D \tag{25.107}$$

$$f(T) \approx \exp\left\{ -\frac{6E_R}{k\theta_D} \frac{T}{\theta_D} \right\}, \quad \text{if } T \gg \theta_D \tag{25.108}$$

where E_R is the recoil energy and θ_D is the Debye temperature.

The temperature dependence of the magnetic splitting itself depends on the nature of the magnetic interaction in the investigated material.

Fig. 25.14

Temperature dependence of the quadrupole splitting of ^{57}Fe in $Cd_3[Fe(CN)_6]_2$ (Based on Vértes et al. 1979)

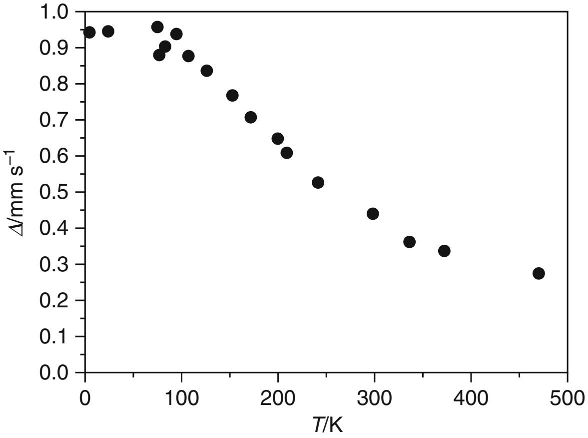

Fig. 25.15

Typical shape of the temperature dependence of the Mössbauer–Lamb factor

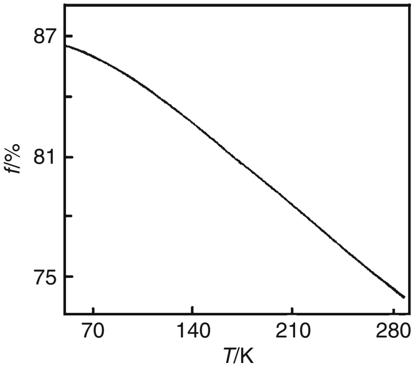

For simple *ferromagnetic* interaction, e.g., when the Bloch law (Kittel 1968) is valid for the field, one obtains

$$\frac{\Delta E_m(T)}{\Delta E_m(0K)} = 1 - CT^{3/2} \tag{25.109}$$

where C is a constant.

In the case of some *paramagnetic* materials exhibiting magnetically split Mössbauer spectra, the magnetic splitting is due to the paramagnetic spin relaxation time τ_{SR} being relatively high in comparison with the *Larmor precession* time of the nucleus. In this case, temperature dependence is governed by that of the spin-lattice relaxation of the material (Vértes and Nagy 1990).

The temperature dependence of the peak width W caused by the diffusive motion of resonant nuclei can be expressed either by the formula

$$\frac{\Delta W}{W} = \exp\left(-\frac{E^*}{kT}\right) \tag{25.110}$$

or by

$$\Delta W = \frac{2c\hbar}{E_0\tau_0}\left[1 - \int e^{ikr}h(r)\mathrm{d}r\right], \tag{25.111}$$

where E^* is the activation energy, $\boldsymbol{k}$ is the wave vector of the γ photon, $h(\boldsymbol{r})$ is the probability density of finding an atom after one jump at point $\boldsymbol{r}$ relative to the origin of the jump, and τ_0^{-1} is the jump frequency (Singwi and Sjolander 1960).

25.2.7.2 Pressure Dependence

The pressure dependence of Mössbauer parameters follows from that of the physical quantities that determine the values of those parameters. The pressure dependence of the isomer shift (Shenoy and Wagner 1978), e.g., is illustrated in *Fig. 25.16*.

25.2.7.3 External Magnetic Field Dependence

The external magnetic field dependence of Mössbauer parameters can be very important, because – by choosing an appropriate external magnetic flux density – one often gets a better-resolved spectrum.

Fig. 25.16
Pressure dependence of the isomer shift of ^{57}Fe in α-Fe, based on the results of Williamson et al. (1972)

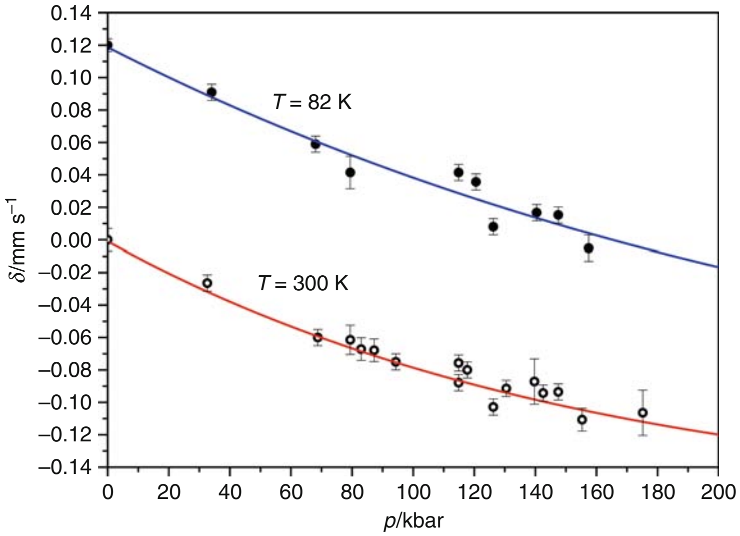

By applying an external magnetic field, one can produce sources of polarized γ rays. In ^{57}Fe Mössbauer spectroscopy, this can be done by embedding the ^{57}Co parent nuclide in a ferromagnetic host (e.g., in α-Fe) and by magnetically saturating the host material with an appropriate external field. Such a source will emit six lines (instead of just one) which, when overlapping with a simple six-line absorber hyperfine pattern, will lead to 36 (i.e., six times six) possible absorption peaks (Gonser 1975a).

The *effective magnetic flux density* $\boldsymbol{B}$ measured at the nucleus consists of two terms:

$$\boldsymbol{B} = \boldsymbol{B}_{\text{ext}} + \boldsymbol{B}_{\text{int}} \tag{25.112}$$

where $\boldsymbol{B}_{\text{ext}}$ is the external magnetic flux density and $\boldsymbol{B}_{\text{int}}$ is the *internal magnetic flux density* which, again, consists of a number of components of different origin (Thosar and Iyengar 1983).

The use of external magnetic field makes it possible to determine the sign of the quadrupole splitting from the induced magnetic pattern (Gütlich et al. 1978) in the case of ^{57}Fe and ^{119}Sn spectroscopy of nonmagnetic materials.

The effect of external magnetic field on the magnetic splitting of magnetic materials depends on the nature of magnetic coupling (i.e., whether the material is ferromagnetic, ferrimagnetic, or antiferromagnetic) (Gonser 1975a).

25.2.7.4 Radio-Frequency Electromagnetic Radiation

Radio-frequency electromagnetic radiation can have two kinds of effect on the Mössbauer spectrum (Gonser 1981). It can result in a collapse of the split Mössbauer pattern, but it can also produce side bands in the spectrum on the basis of which a better identification of the atomic species can sometimes be achieved (Kopcewicz 1989).

25.2.7.5 Angular Dependence of Peak Areas/Intensities

The angular dependence of peak areas follows from the angular dependent nature of the intensity of multipole radiations (see ➲ *Table 25.2* for $F_{lm}(\theta)$ in the case of $l = 1$).

Magnetic sextet. The angular dependence of the relative peak areas of a magnetic sextet (appearing in, e.g., ^{57}Fe and ^{119}Sn Mössbauer spectra, both representing the $I = 3/2 \longrightarrow 1/2$ nuclear spin transition), can be calculated by multiplying the $3j$ symbols with the corresponding $F_{lm}(\theta)$ angular dependent terms (both given in ➲ *Table 25.2*). Apart from a constant factor one obtains

$$A_1(\theta) = A_6(\theta) = 3(1 + \cos^2\theta) \tag{25.113}$$

$$A_2(\theta) = A_5(\theta) = 4\sin^2\theta \tag{25.114}$$

$$A_3(\theta) = A_4(\theta) = \frac{1}{3}A_1(\theta) = \frac{1}{3}A_6(\theta) = (1 + \cos^2\theta) \tag{25.115}$$

where θ is the angle between the respective directions of the γ ray and the effective magnetic flux density, and the area subscripts refer to the peak numbers of the sextet.

In the case of ferromagnetic materials, the direction of the effective magnetic flux density $\boldsymbol{B}$ can be manipulated by an external field $\boldsymbol{B}_{\text{ext}}$.

If the direction of the effective magnetic field changes from point to point in a sample so that each direction has the same occurrence, then the relative peak areas (intensities) of the resultant sextet will average out to

$$A_1 : A_2 : A_3 : A_4 : A_5 : A_6 = 3 : 2 : 1 : 1 : 2 : 3, \tag{25.116}$$

which is the typical case for antiferromagnetic powder samples without texture. Bulk ferromagnetic materials (e.g., a not too thin α-iron foil) also have such a tendency, because the magnetic moments of their domains point at random directions.

In the case of magnetic anisotropy, the relative intensity of the second and the fifth lines compared with that of the first and sixth lines depends on θ in the following way:

$$\frac{A_{2,5}}{A_{1,6}} = \frac{4\sin^2\theta}{3(1+\cos^2\theta)} \tag{25.117}$$

(Note that the intensity ratio of the inner and the outer pairs of lines of a sextet has no angular dependence, it is always equal to 3.)

Quadrupole doublet. In the case of a quadrupole doublet, the relative areas (intensities) of the doublet peaks (one representing the $m_I = \pm 3/2 \rightarrow \pm 1/2$ and the other the $m_I = \pm 1/2 \rightarrow \pm 1/2$ nuclear transitions) apart from a constant factor will have the angular dependences

$$A_{\pm 3/2\rightarrow\pm 1/2}(\theta) = 1 + \cos^2\theta \tag{25.118}$$

$$A_{\pm 1/2\rightarrow\pm 1/2}(\theta) = \frac{5}{3} - \cos^2\theta \tag{25.119}$$

where θ is the angle between the respective directions of the γ ray and the main axis of the EFG at the nucleus.

The intensity ratio of the lines of the doublet can also be expressed as (Gütlich et al. 1978)

$$\frac{I_2}{I_1} = \frac{\int_0^\pi (1+\cos^2\theta)h(\theta)f(\theta)\sin\theta \mathrm{d}\theta}{\int_0^\pi \left(\frac{5}{3}-\cos^2\theta\right)h(\theta)f(\theta)\sin\theta \mathrm{d}\theta} \tag{25.120}$$

where $h(\theta)$ is the probability density of the angle θ, and $f(\theta)$ gives the angular dependence of the Mössbauer–Lamb factor.

In a well-mixed powder sample, where there is a random distribution ($h(\theta) = 1/\pi$) of the electric field gradients, and the Mössbauer–Lamb factor is isotropic, a symmetrical doublet with equal peak areas is expected: $A_{\pm 3/2\rightarrow\pm 1/2} : A_{\pm 1/2\rightarrow\pm 1/2} = 1 : 1$

The deviation from the above symmetry in most cases is an indication that the powder sample has some *texture*. If the asymmetry is indeed due to texture, then in accordance with Eq. (25.120) the relative intensity of the peaks should change when the sample is turned around an axis that is perpendicular to the direction of the γ rays. If the preferred orientation of the sample is such that the z-axis of the principal axis system is parallel to the direction of γ rays ($\theta = 0$ in Eqs. (25.118)–(25.120)) then a maximum asymmetry of the peaks is observed (relative intensity of the peaks is 3 in this case). If one turns this sample by $\Delta\theta = 54.7°$ (the so-called *magic angle*) then the two peaks in the Mössbauer spectrum will have equal intensity despite the presence of texture.

The other possible reason for the intensity asymmetry ($A_2/A_1 \neq 1$) of the quadrupole split doublet can be the so-called *Goldanskii–Karyagin effect* (Goldanskii et al. 1963), which is caused by the angular dependence of the Mössbauer–Lamb factor due to the anisotropy of lattice vibrations ($f(\theta)$ depends on θ).

For a comparison of the Goldanskii–Karyagin effect with the effect of texture see, e.g., Pfannes and Gonser (1973).

25.2.7.6 Absorber Thickness

The dependence of the experimental peak width (W) on the absorber thickness for Lorentzian peaks is given (Nozik and Kaplan 1967) by the following equations derived from ➲ Eq. (25.100):

$$W = W_0(2 + \tau/4 + \tau^2/96 - \tau^3/64) \quad \text{for } \tau < 2, \tag{25.121}$$

and

$$W = 2W_0\tau/(\sqrt{\pi\tau} - 1) \quad \text{for } \tau < 2, \tag{25.122}$$

where W_0 is the peak width corresponding to the natural line width of the given Mössbauer transition and τ is the effective thickness of the absorber. The absorber thickness can also be optimized as regards the time necessary to measure a spectrum with satisfactory statistics (Nagy et al. 1975).

➲ *Figure 25.17* shows the peak area, peak height, and peak width as the function of effective thickness.

Fig. 25.17

Dependence of the peak area *A*, peak height *H*, and peak width *W* on the effective thickness of the absorber (τ_A). Γ is the natural line width and f_S is the Mössbauer–Lamb factor of the source

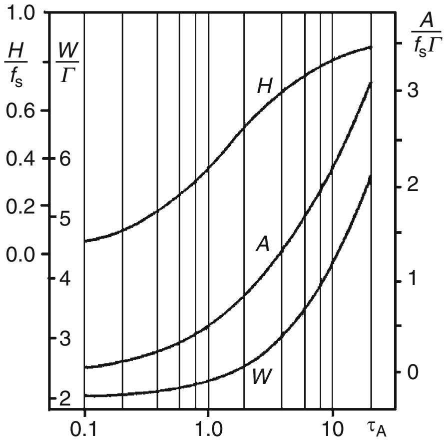

25.2.7.7 Geometric Arrangement

The dependence of Mössbauer parameters on geometric arrangements is mainly due to the cosine smearing of the velocity u. Since the Doppler energy shift ΔE_γ is given by

$$\Delta E_\gamma = E_\gamma \frac{u}{c} \cos\theta, \tag{25.123}$$

(where E_γ is the energy of the emitted γ photon) a smearing effect can always be observed on the experimental peak shape, peak width, and isomer shift (Shenoy and Wagner 1978), even under "ideal" conditions when one uses a point source and a circular absorber placed coaxially as illustrated by *Fig. 25.18*. (Above, θ is the angle between the γ ray and the direction of motion of the source or the absorber, whichever is moved.)

25.3 Analytical Information from Mössbauer Spectra

25.3.1 The Fingerprint Method

Patterns and physicochemical entities. In general, the fingerprint method operates with patterns ("fingerprints") characteristic of different phases, compounds, crystallographic sites etc., which will be referred to as physicochemical entities for brevity. The correspondence between individual patterns and such entities is determined by the nature of interactions serving as a basis for the analytical method. In the case of Mössbauer analysis, the basic interactions are the hyperfine interactions.

Since the hyperfine interactions are determined principally by the electron density and the inhomogeneous electric field as well as by the effective magnetic flux density at the nucleus, the Mössbauer spectrum patterns differ from site to site where these physical quantities are different. Thus, a single-phase material may be characterized by a complex Mössbauer spectrum superimposed from a number of simple Mössbauer patterns belonging to resonant atoms experiencing different hyperfine interactions.

The microenvironment (see Sect. 25.1.5.5) is of basic importance for analytical purpose. Since there is a one-to-one correspondence between the microenvironment and the hyperfine interactions, a simple Mössbauer pattern is always associated with a microenvironment characteristic of one particular population of Mössbauer nuclei in the studied sample. For brevity, such a population of like Mössbauer nuclei is referred to as a *Mössbauer species*.

Fig. 25.18

The origin of cosine smearing. *u* is the velocity of the source relative to the absorber

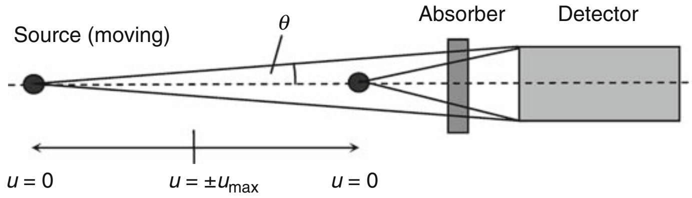

25.3.2 Pattern Analysis

The basic task of the analysis is to identify the individual Mössbauer species from the corresponding patterns present in the spectrum. Ideally, this can be done if there is an exact correspondence between them.

Unfortunately, such a one-to-one correspondence between Mössbauer species and individual patterns may be nonexistent under the given conditions, i.e., for that particular set of experimental parameters at which the Mössbauer spectrum was recorded. However, when the whole range of the possible conditions is considered, one may find points in the space of experimental parameters at which only one pattern is associated with one species and vice versa and thus one can get round the problem of ambiguity. One can also do simultaneous evaluation of a whole series of Mössbauer spectra taken from the same sample under different conditions. Such a *serial evaluation* is a very effective tool, because the known dependences of the Mössbauer parameters (e.g., isomer shift) on the externally set experimental parameters (e.g., temperature) can be used as constraints for the serial fit.

From the analytical point of view, one can classify *Mössbauer patterns* in the following way (Kuzmann et al. 2003).

According to *experimental conditions* there are *standard patterns* and *induced patterns.*

According to *complexity* there are *elementary patterns* and *superimposed patterns.*

According to *mathematical processing* there are *natural patterns* and *transformed patterns.*

A Mössbauer spectrum can be a simple spectrum (elementary pattern) reflecting only a unique microenvironment/Mössbauer species or a complex spectrum (superimposed pattern), which consists of a number of subspectra.

The *standard pattern* is associated with a Mössbauer spectrum obtained at a standard set of experimental parameters. In most laboratories, e.g., measurements performed at room temperature, under atmospheric pressure and without external magnetic field are considered as standard. The *induced pattern*, however, is obtained under conditions other than standard (e.g., measurements performed in a cryostat or a furnace or in the field of a magnet). In this case, the differences between the induced and standard patterns can give important contribution to the analysis.

The *elementary pattern* is associated with one type of microenvironment/Mössbauer species. The *superimposed pattern* is the superposition of elementary patterns.

The *transformed pattern* is obtained from the measured Mössbauer spectrum (i.e., from the *natural pattern*) by mathematical transformation (e.g., by Fourier transformation). For instance, the magnetic hyperfine field (i.e., effective magnetic flux density) distribution or the quadrupole splitting distribution are considered transformed patterns. The transformed pattern may give a better resolution for the analysis.

➲ *Figures 25.19* and ➲ *25.20* illustrate the relation between different types of patterns and the object of the analysis as well as the most common strategy followed when doing qualitative analysis in Mössbauer spectroscopy. Generally, the Mössbauer spectrum of a multi-compound/multiphase material is a superposition of superimposed patterns. This is so because each compound/phase can have different crystallographic sites, each site represented by a different pattern. Note that even a single crystallographic site may represent more than one microenvironment due to variations in the hyperfine interactions (e.g., different electronic and spin density and defect arrangement).

In order to give an example, let us consider a steel sample in which ferrite and austenite phases are present. The standard pattern (^{57}Fe Mössbauer spectrum) of the sample is a complex spectrum that is a sum of subspectra (➲ *Fig. 25.21*). The subspectra of the ferromagnetic ferrite

Fig. 25.19

Relation between different types of patterns and the object of analysis

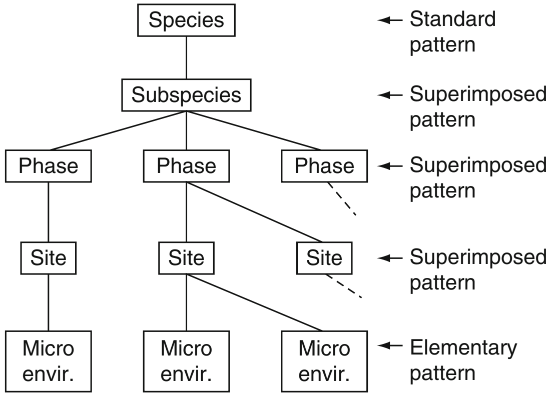

Fig. 25.20

Simplified strategy of qualitative analysis in Mössbauer spectroscopy (i. and n.i. stand for informative and not informative, respectively)

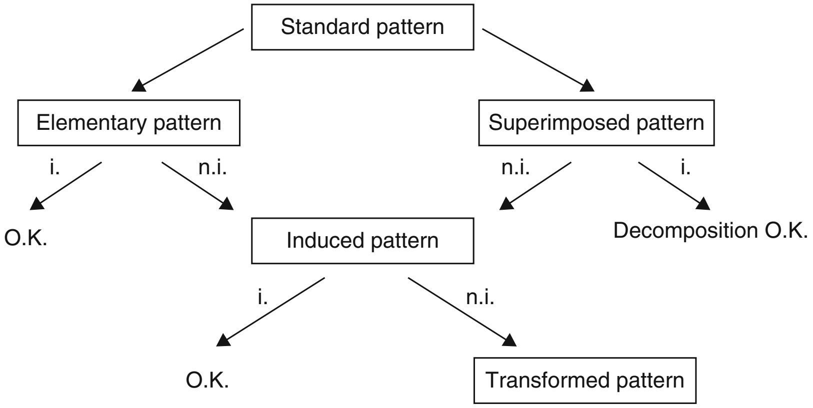

and the paramagnetic austenite are also superimposed from elementary patterns because of the effect of alloying elements.

Very often, when the characteristic subspectra of components are well distinguishable in the standard spectrum, the qualitative analysis can be performed without the need for measuring further nonstandard spectra (induced patterns). In general, however, the subspectra (elementary patterns) overlap each other in the standard spectrum. When the exact decomposition of the spectrum becomes ambiguous, it is still possible to get further analytical information from an induced pattern (e.g., via serial evaluations).

For example, the standard room-temperature patterns of akageneite (β-FeOOH) and lepidocrocite (γ-FeOOH) are paramagnetic doublets with similar parameters. So they cannot be easily differentiated. However, the induced patterns of β-FeOOH taken below the magnetic

Fig. 25.21

The standard pattern of a steel in which ferrite and austenite phases are present. The ^{57}Fe Mössbauer spectrum of the sample is a complex spectrum that is a sum of subspectra. The subspectra of the ferromagnetic ferrite with bcc lattice and the paramagnetic austenite with fcc lattice are also superimposed from elementary patterns because of the effect of alloying elements, although the Fe atoms can only occupy one single crystallographic site in each phase

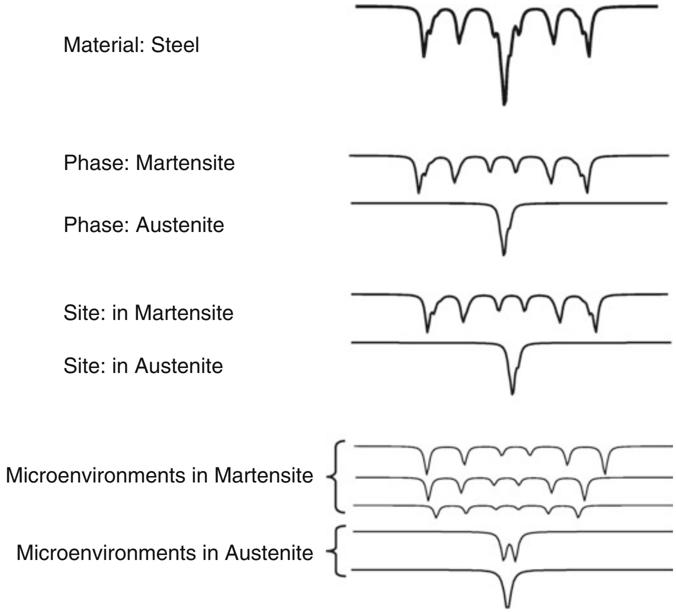

transition temperature (*Fig. 25.22*) reflect magnetically split subspectra (sextets). Now, by the help of the induced pattern, the analytical problem can be solved more easily.

In some cases, the natural pattern consists of hundreds of elementary patterns. This is the typical situation with poorly crystallized and amorphous systems. The transformed pattern (*Fig. 25.23*) can help get more information about the short-range ordering (by characterizing some of the most probable arrangements), thus it can enhance the analytical applicability.

25.3.3 Spectrum Evaluation

The Mössbauer parameters are derived from the *peak parameters* (base line parameters, peak position, peak width, and peak area/height) via the fitting process by computer evaluation of spectra in the case of the so-called model-dependent evaluation. In this case, an exact a priori knowledge about the spectrum decomposition (peak-shape function, number, and type of subspectra corresponding to the interactions assumed for each microenvironment in the model) is inevitably necessary. (Incorrectly chosen number of peaks renders the analysis itself incorrect.)

The most precise way of fitting is based on the computation of the transmission integral given by Eq. (25.31).

Very often, however, the simple Lorentzian peak shape is considered (see also Eqs. (25.1) and (25.35)):

Fig. 25.22

The induced patterns of akagenite (Kuzmann et al. 1994) carry much more information for the analysis than the standard one

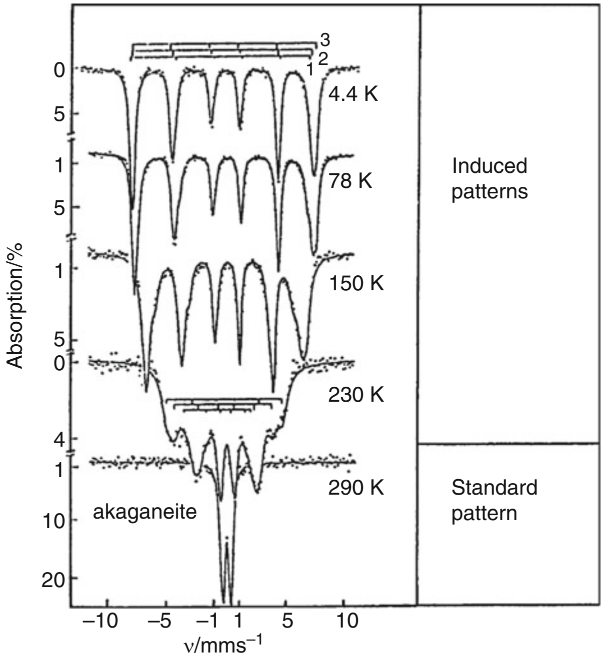

$$L(u) = \frac{1}{\pi}\frac{W}{2}\frac{A}{(u-u_0)^2 + \left(\frac{W}{2}\right)^2} = \left(\frac{W}{2}\right)^2 \frac{H}{(u-u_0)^2 + \left(\frac{W}{2}\right)^2} \tag{25.124}$$

where u_0 is the position (in mm/s), W is the width, A is the area (intensity), and H is the height of the peak. This can be a good approximation, if the absorber is sufficiently thin (the effective thickness τ_A should be less than 1) and if the number of overlapping peaks is not very large.

For the analysis of materials whose spectra consist of a large number of overlapping peaks (e.g., amorphous metals), the product (or rather the convolution) of Lorentzian and Gaussian curves (Voigt function) is used to fit the peaks (Seagusa and Morrish 1982).

The spectrum fitting is done by the least-squares method by using an appropriate model function S, e.g., a linear combination of Lorentzians. (See also ➔ Sect. 9.3.6 on Fitting nuclear spectra in Chap. 9, Vol. 1, on "Stochastics and Nuclear Measurements.") In this procedure, the sum

$$\chi^2 = \sum_{i=1}^{k} \frac{1}{N_i}\left[N_i - S(i; P_{\text{peak}})\right]^2 \tag{25.125}$$

is minimized, where N_i is the number of counts stored in the ith channel; k is the total number of channels. The model function S is determined by the vector $\boldsymbol{P}_{\text{peak}}$ of the peak parameters that is set up from the individual parameter vectors of the baseline ($\boldsymbol{p}_0$) and the peaks ($\boldsymbol{p}_1, \boldsymbol{p}_2, \ldots \boldsymbol{p}_n$):

$$\boldsymbol{P}_{\text{peak}} = (\boldsymbol{p}_0, \boldsymbol{p}_1, \boldsymbol{p}_2, \ldots \boldsymbol{p}_n) \tag{25.126}$$

Fig. 25.23

The transformed patterns (graphs on the right side) of poorly crystallized ferrihydrite (Kuzmann et al. 1994). (a) 57Fe Mössbauer spectrum of poorly crystallized ferrihydrite at room temperature, and (b) the corresponding quadrupole splitting distribution. (c) 57Fe Mössbauer spectrum of poorly crystallized ferrihydrite at 4K, and (d) the corresponding hyperfine magnetic field distribution

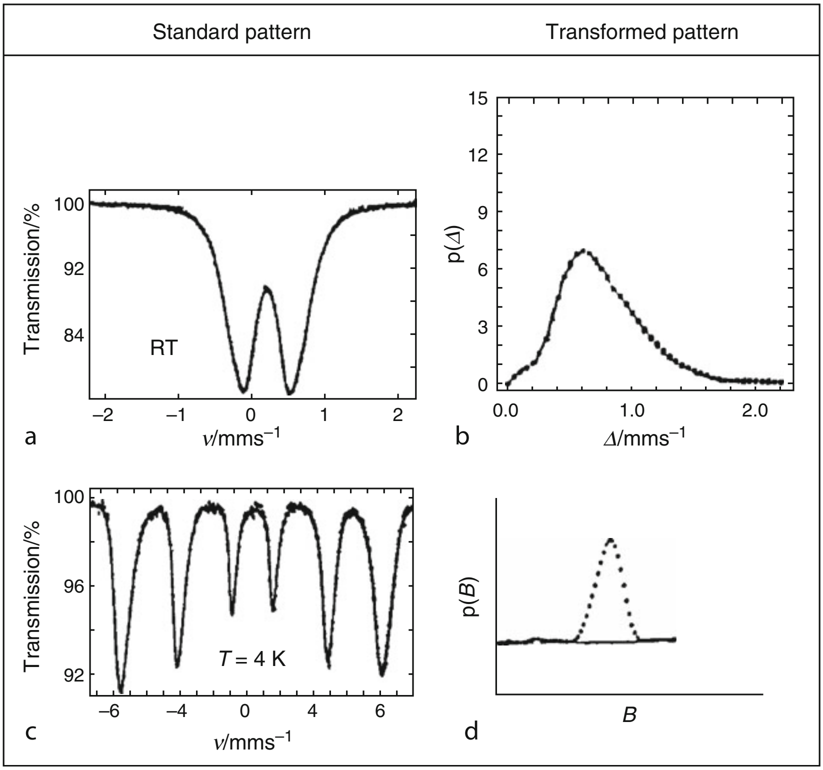

Each parameter vector $\boldsymbol{p}_j$ itself represents a set of three parameters characterizing the position, width, and area/height of the jth peak out of n.

In the thin-absorber approximation, an inhomogeneous linear transformation is used to make connection between the vector of the Mössbauer parameters $\boldsymbol{P}_{\mathrm{M}}$ (set up from isomer shifts, quadrupole splittings, magnetic splittings, etc.) and the vector of the peak parameters $\boldsymbol{P}_{\mathrm{peak}}$:

$$\boldsymbol{P}_{\mathrm{M}}^{\mathrm{T}} = \boldsymbol{T}\boldsymbol{P}_{\mathrm{peak}}^{\mathrm{T}} + \boldsymbol{C}^{\mathrm{T}} \tag{25.127}$$

where the constraints are determined by the elements of the transformation matrix $\boldsymbol{T}$ and the constant vector $\boldsymbol{C}$. (The superscript “T” is to indicate that one has column vectors in the formula.)

The a priori knowledge of the matrix $\boldsymbol{T}$ and the vector $\boldsymbol{C}$ is normally an essential condition of spectrum evaluation. From the point of view of analytical applications, the a priori determination of the $\boldsymbol{T}$ matrix is of fundamental importance. Namely, this transformation enables the experimenter to specify a set of peaks as a pattern representing one particular Mössbauer species in the sample.

The assignment of the subspectrum to one particular Mössbauer species is based on the comparison of the derived pattern with a reference spectrum. The *reference spectrum* can be obtained by measuring an etalon material or from the data published in the literature. In some cases, the reference spectrum can be constructed theoretically (computer simulation).

Another, so-called model-independent way of spectrum evaluation is done by obtaining and analyzing transformed patterns. For a thin absorber, the spectrum shape $S(u)$ can be described as the convolution of a density function $f(u)$ with a Lorentzian function $L(u)$:

$$S(u) = \int_{-\infty}^{+\infty} f(v)L(u-v)\mathrm{d}v. \tag{25.128}$$

One of the methods for obtaining the distribution of effective magnetic flux density or quadrupole splitting (Campbell and Aubertin 1989; Klencsár et al. 1996) is the *Window method* (Window 1971) that uses a Fourier technique. For instance, the distribution of the effective magnetic flux density (also called *hyperfine field distribution*)

$$p(B) = \sum_{i}^{N} a_i \left[\cos \frac{B_i - B_{\mathrm{min}}}{B_{\mathrm{max}} - B_{\mathrm{min}}} - (-1)^i\right] \tag{25.129}$$

can be obtained by fitting the spectrum (B_{min} and B_{max} are the minimum and maximum values of the effective magnetic flux density, respectively).

Another way to obtain the distribution of the effective magnetic flux density or the quadrupole splitting is the *Hesse–Rübartsch method* (Hesse and Rübartsch 1974).

25.3.4 Quantitative Analysis

In Mössbauer spectroscopy, as in other spectroscopic methods, quantitative analysis is based upon the determination of peak areas.

In general, the transmission integral (Eq. (25.31)) can be used to evaluate the peak area that depends nonlinearly on the effective thickness, which, in turn, is proportional to the concentration of the resonant atoms.

In the *thin-absorber approximation* ($\tau_{\mathrm{A}} < 0.1$), the *peak area* is proportional to the Mössbauer atom concentration as shown earlier:

$$A \approx k\tau_{\mathrm{A}} = k\sigma_0 d_{\mathrm{A}} f_{\mathrm{A}} n_{\mathrm{A}} a \tag{25.130}$$

where a is the fractional abundance of the Mössbauer isotope (e.g., that of ^{57}Fe in natural iron) and n_{A} is the number of atoms of the studied Mössbauer element (e.g., iron) per unit volume of the absorber. The constant k includes other constants and parameters involving the background and matrix effects.

For the determination of concentration n_{A} all the parameters in the above equation have to be known. However, in most cases, the exact values of the Mössbauer–Lamb factor f_{A} and the constant k are unknown. In such cases, calibration graphs obtained with etalons are needed. However, the relative f-factors belonging to different microenvironments are usually known. Consequently, Mössbauer spectroscopy has a unique ability for the determination of the relative concentration of individual Mössbauer species in the same sample. The absolute concentration can be determined more accurately using other techniques.

25.4 Measurement Techniques in Mössbauer Spectroscopy

25.4.1 Mössbauer Spectrometers

In order to measure a Mössbauer spectrum one has to detect recoilless absorption or emission of a selected γ radiation as a function of the Doppler velocity of the sample and a reference material relative to each other. In the most common case of transmission geometry, absorption of the γ rays is measured, and the reference material is a standard source, which is moved. Thus, the most important components of a Mössbauer spectrometer are a Doppler velocity drive system and an energy selective γ detection chain with appropriate recording system.

The Mössbauer measurement requires the generation of a precise, controllable relative motion between the source and the absorber. A large variety of drive systems has been developed. The majority of drives work on electromechanical, mechanical, hydraulic, and piezoelectric principle. The spectrometers can be classified into constant-velocity spectrometers and velocity-sweep spectrometers. The mechanical drives, like a lead screw or a cam, move with constant velocity. They have advantages for the thermal scan method and because their absolute velocity calibration is straightforward. The velocity-sweep spectrometers are usually of electromechanical nature (like loudspeaker-type transducers) and normally used in conjunction with a multichannel analyzer. The most commonly used $u(t)$ functions are rectangular (constant velocity), triangular (constant acceleration), trapezoidal, and sinusoidal. A typical Mössbauer spectrometer is shown schematically in ❯ *Fig. 25.24*.

Fig. 25.24

The block scheme of a Mössbauer spectrometer. A, absorber; CR, cryostat with temperature controller TC (optional, for low-temperature measurements); S, source moved by velocity transducer VT of driving unit DR; FG, function generator; VC, velocity calibrator (optional); LI, laser interferometer (optional); DET, detector; HV, high-voltage power supply; PA, preamplifier; AM, amplifier; SCA, single channel analyzer; MCA, multichannel analyzer; and PC, computer, OP, output

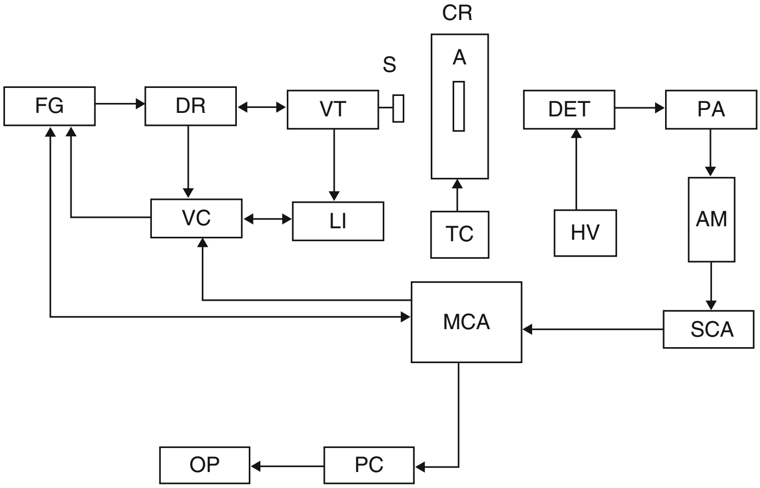

The transmitted or scattered radiation is usually detected by scintillation or proportional counters since high resolution is not required. The signals coming from the detector are amplified and gated by a single-channel analyzer set to transmit the Mössbauer transition energy range. These signals are introduced to a multichannel analyzer working in multiscaler regime (multichannel scaling, MCS). The switching (scaling) of channels is synchronized with the moving system so that in every cycle the same velocity is assigned to the same channel. The electromechanical drives move the source relative to the absorber periodically (with 10–100 Hz frequency) according to the given wave form. In the most typical case, a triangular wave form is used (constant acceleration). In modern Mössbauer spectrometers the velocity step signal is produced by a digital reference generator. While evaluating, the triangular waveform of velocity (with a maximum velocity in the orders of several mm/s) is approximated by a stepwise function of time, at each step of which (50–100 μs) the velocity is considered to be constant. The Mössbauer spectra are usually recorded in 512 or 1,024 channels in each of which 10^5–10^7 counts are collected over several hours or days. Nowadays a major part of the Mössbauer equipment is a personal computer including an analyzer card (PCA card). This setup can be used for the pulse height analysis (PHA) that is needed to select the Mössbauer γ ray (or other secondary radiation), for the recording of the spectrum in MCS mode as well as for the evaluation of the recorded spectra with an appropriate software.

The Mössbauer spectrum is usually obtained as the transmitted or scattered intensity (in counts) vs. the Doppler velocity (in mm/s). However, the data provided by the analyzer are normally given in the form of counts vs. channel number. The correspondence between channel numbers and velocity is established by velocity calibration.

The *velocity calibration* of the Mössbauer spectrometer is performed either by measuring the Mössbauer spectrum of standard materials or by a calibrator instrument measuring the absolute velocity of the source relative to the absorber. The latter can be achieved by counting the fringes from a Michelson interferometer with a laser source connected to the multichannel analyzer, and thus the velocity for each channel can be obtained.

25.4.2 Transmission Geometry

Mössbauer spectra can be recorded in different ways. In the most frequently used *transmission technique* (› *Fig. 25.5*) the γ photons are counted after passing through the sample used as an absorber.

In most cases, the commercial source is moved and the absorber (which is the material to be studied) is at rest. In emission experiments, however, where the source is the material to be studied, the reference absorber is usually moved (see › *Fig. 25.6* and › Sect. 25.4.4).

Scintillation detectors with a thin NaI(Tl) crystal are frequently applied for the detection of γ rays for many Mössbauer nuclides depending on the transition energy and the count rate. Various types of proportional counters are also used especially if the count rate is not very high. Semiconductor detectors are also applied occasionally. (For more about γ detectors see › Chap. 48 in Vol. 5.)

25.4.3 Reflection Geometry

In the scattering technique (› *Fig. 25.25*) the various radiations produced through the de-excitation of the irradiated sample (resonance scatterer) are detected.

Fig. 25.25

Scattering techniques. Reflection arrangements for Mössbauer measurements for γ ray or characteristic X-ray detection (*on the left*) and for conversion electron detection, CEMS (*on the right*)

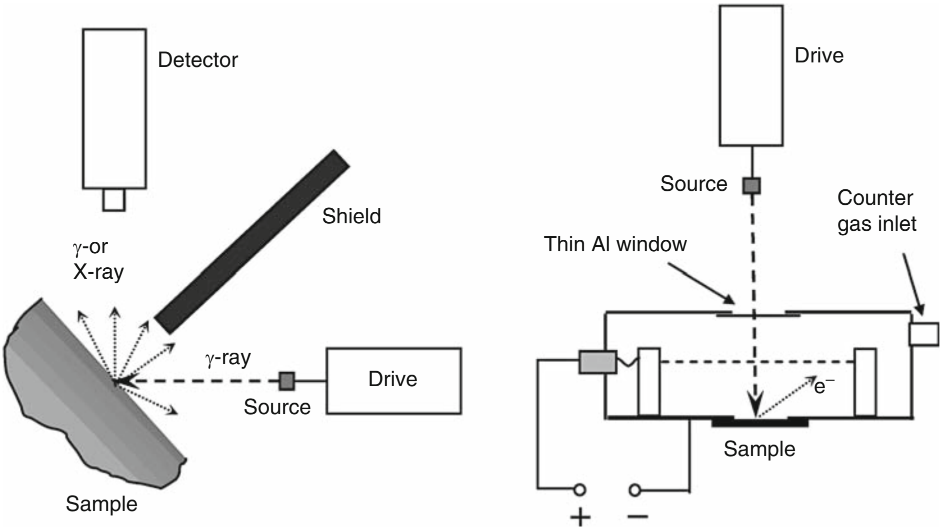

With the *scattering technique*, it is possible to detect γ rays (back-scattering γ-ray Mössbauer spectroscopy), X-rays (X-ray Mössbauer spectroscopy), or conversion electrons (conversion electron Mössbauer spectroscopy, CEMS), which are characterized by different escape depths. Consequently, by the detection of different forms of back-scattered radiation, the surface of the samples can be investigated at different depths. An important advantage of the scattering Mössbauer technique is that it provides a nondestructive way of material testing.

25.4.3.1 Conversion Electron Mössbauer Spectroscopy

Among scattering Mössbauer measurements, the conversion electron Mössbauer spectroscopy (CEMS) is most developed because CEMS provides a unique surface characterization of solid materials. Since in Mössbauer spectroscopy the high Mössbauer–Lamb factor requires low γ energy, it inevitably results in very high electron conversion coefficients (see Table of Mössbauer Nuclides in Appendix of this volume) and therefore the γ sources work at very high losses. This severe setback is turned to an advantage in CEMS. In this method, the γ rays emitted from the source undergo recoilless absorption in the "CEMS-sample." The excited Mössbauer nuclei will then de-excite according to a characteristic lifetime and generate the conversion electrons to be detected.

The penetration range of conversion electrons of a few kilo electron volt is limited to a few 100 nm. The depth information of solid surface layers obtained by CEMS depends on the energy of electrons detected. The emitted electron energy corresponds to the photon energy minus the binding energy of the electron. The *conversion coefficient* $\alpha = N_e/N_\gamma$ (where N_e and N_γ are the numbers of the emitted electrons and photons, respectively) is 8.21 for ^{57}Fe, and 5.1 for ^{119}Sn. The larger the α, the more effective the electron emission. However, not only conversion electrons are emitted, but a large number of Auger electrons can also be expected with substantially lower energies. The emission probability of electrons and photons in the relaxation process following the nuclear absorption in the ^{57}Fe nucleus is 7.3 keV K conversion electrons (80%), 5.6 keV KLL Auger electrons (53%), reemitted 14.4 keV γ rays (10%), and 6.4 keV characteristic Kα X-rays (27%). The total number of electrons emitted is 133% of the number of photons absorbed. In the case of ^{119}Sn nuclei, 19.8 keV L conversion electrons (84%), 23.0 keV M conversion electron (13%), 2.8 keV Auger electrons (75%), 23.8 keV γ ray (16%), and 3.6 keV X-ray (9%) are emitted after Mössbauer absorption. The total percent of electrons emitted is 172%. It is clear from the total emission probability of conversion and Auger electrons that the detection of electrons is advantageous for thin films and solid surface studies (Bonchev et al. 1969).

Detectors for CEMS

Gas counter. A simple proportional gas counter is shown in ❯ *Fig. 25.25*. A backscatter 2π proportional He gas-flow counter has high detection efficiency for low-energy electrons of about 10 keV, because He gas is insensitive to incident X-ray and γ ray (Terrell and Spijkerman 1968). CEMS spectra can be easily recorded by flowing He gas mixed with several % methane or isobutane as a quencher. XM spectra (i.e., when the characteristic X-ray is detected) can also be obtained by using flowing Ar/CH_4 gas mixture and by setting a Lucite plate (3 mm thick) in front of the incident window of the counter in order to filter off the X-rays emitted from the source. Argon, being a relatively light element, can detect 6.3 keV Fe X-rays more efficiently than 14.4 keV incident γ rays. The penetration range of 7.3 keV electrons in He gas of atmospheric pressure is at most 5 mm. The mean energy of electrons emitted is less than 7.3 keV, and the desirable distance between the anode wire and the sample surface is about 2 mm for ^{57}Fe CEMS. The detection efficiency of electrons and good signal-to-noise ratio are crucial to improve the count rate, and they sensitively depend on the actual design of the detector. A good electric contact between the sample (for which it is advisable to be a good conductor) and the body of the detector is very important.

The parallel-plate avalanche counter (PPAC) (Weyer 1976), which consists of flat-plate electrodes of graphite and sample, is advantageous for insulating materials. Any organic polyatomic gas can be used as *counting gas*. Usually acetone vapor is preferred. Depth selective CEMS (DCEMS, see later on) using PPAC is also possible by discriminating electron energy and controlling gas pressure (Weyer 1990). However, the mounting of a sample and the control of pressure in PPAC are rather difficult.

When a proportional counter is operated at low temperature, the gas multiplication decreases, and some quenchers mixed in the He gas get condensed on the cold surface of the sample. A gas counter filled with He + 5% CO at atmospheric pressure showed good performance at 77 K (Isozumi et al. 1983; Cook and Agyekum 1985; Nomura and Ujihira 1985; Meisel 1994). Purified He, H_2, Ne, and mixtures of two gases such as He + 5% N_2 or He + several % CO may be used from temperatures as low as 15–300 K (Fukumura et al. 1991).

For high-temperature CEMS measurements, a gas-flow counter was installed in a furnace by Isozumi et al. (1979). Another type of gas counter was developed to heat only the sample; it was tested up to 740 K (Inaba et al. 1981). At even higher temperatures, low recoilless fraction, reaction of the quenching gas with the sample surface, and intense thermal electron emission made the measurement impossible. However, the gas reactivity can be utilized to monitor in situ gas sensing of sensor materials because various gases can be mixed into He gas as a quenching gas (Nomura et al. 1993).

Electron multipliers and other counters. Channeltrons and channelplates have relatively large efficiency for low-energy electrons (below a few kilo electron volt). These types of counters have inherently no energy resolution, and need to work in a vacuum chamber. Both the sample and the channel electron multiplier installed are directly cooled in a conventional vessel by liquid He or liquid N_2 for CEMS (Sawicki et al. 1981).

The avalanche photodiode detector (APD), which is able to detect conversion electrons with very high intensity can also be useful in special applications (Weyer 1976; Gruverman 1976).

Depth Selective CEMS

Since the conversion electrons emitted from the sample surface have different energies depending on the depth they were generated in, it is theoretically possible to record Mössbauer spectra characteristic of selected surface layers of the sample at different depths. Geometric effects and the relatively wide energy spectrum of the various kinds of emitted electrons (K- and L-conversion, Auger, etc.) result in rather poor depth resolution.

To achieve depth selectivity, the Mössbauer setup should be combined with an electron spectrometer. A magnetic wedge spectrometer was first used for the detection of 30.5 keV K shell conversion electrons produced by the 100.1 keV γ transition in ^{182}W (Kankeleit 1961). DCEMS was proposed by Baverstam et al. (1973); DCEMS spectra were first measured with ^{119}Sn (Bonchev et al. 1977) and ^{57}Fe (Shigematsu et al. 1980) by selecting electrons with a specific energy range.

Practice and theory of DCEMS were further developed by several authors (Liljequist 1981; Kajcsos et al. 1988; Klingelhofer and Kankeleit 1990; Klingelhofer and Meisel 1990; Belozerskii 1993).

Depth selectivity may also be achieved by using normal CEMS (for better distinction sometimes referred to as *ICEMS*, i.e., Integral CEMS) if the sample surface layers are removed stepwise with an appropriate technique like, e.g., noble gas ion sputtering or etching (Smit and van Stapele 1982). However, this is already a destructive analytical method.

A pronounced depth selectivity of CEMS spectra is achieved by selecting the angle of the incident γ ray in addition to selection of the energy of the emitted electrons. On the other hand, depth information changes depending on the applied voltage (Kuprin and Novakova 1992). The layer-by-layer analysis of rough structures is possible by selecting the energy of detected electrons and by changing the voltage supplied using a He gas-flow counter.

Glancing angle CEMS (*GACEMS*) is useful to analyze the orientation of thin films. The influence of surface roughness on the surface selectivity in ^{57}Fe GACEMS is small provided that the electron-emission angle relative to the surface is larger than the average surface inclination angle associated with the surface roughness (Ismail and Liljequist 1986). According to the theory of CEMS at total external reflection (Andreeva and Kuzmin 1984; Topalov and Proikova 1985), the selective observation of a surface layer with a mean depth <10 nm is possible at glancing angles of less than 10 mrad ($\sim 0.6°$).

Grazing incident ^{57}Fe CEMS (*GICEMS*) spectra were first observed by Frost et al. (1985), and GICEMS equipments were improved to have higher precision (Irakaev et al. 1993).

These techniques are rather time consuming, and the application of monochromatic photon beams of synchrotron sources may reduce the necessary measuring time in the future.

25.4.4 Resonance Counters

The most specific type of detectors used in Mössbauer spectroscopy is the so-called resonance detector. In this type of detectors, mainly conversion electrons are detected in a gas-filled chamber in which an ^{57}Fe-enriched standard target is placed. As conversion electrons can only form after the recoilless absorption of the γ rays in the standard target, the nonresonant radiation is very effectively filtered off, and the resultant Mössbauer spectrum has hardly any background (baseline). Therefore, the signal-to-noise ratio becomes excellent and the required measuring time (or the source activity that is needed) drastically decreases.

Since in this simple case, the detector itself contains a Mössbauer standard, the investigated material is in the source, i.e., one has to perform an emission experiment (see Sect. 25.4.5).

A "regular" transmission (absorption) experiment can also be carried out using a resonance detector, if the detector and the source are mounted on the same rigid frame and the standard matrix for the source and the target matrix containing the enriched ^{57}Fe (or other Mössbauer nuclide) are the same. The investigated sample should be placed in between. Either the detector + source system or the sample should be moved, which is not simple to realize technically.

A gas-filled resonance counter had been set up, e.g., by installing enriched ^{57}Fe stainless steel foils in a He gas chamber or parallel plate avalanche gas counter by Mullen and Stevenson (1978). An extremely light detector ($K_2Mg^{57}Fe(CN)_6$ in Poly-Vinyl-Xylene scintillator) has also been developed for a movable resonance counter (Budakovski et al. 1999) to replace heavy gas-filled detectors.

Resonance detectors are also useful for Coulomb-excited nuclear experiments and for in situ implantation experiments using short-lived ^{57}Mn as parent nuclide to produce ^{57}Fe (Kobayashi et al. 2000).

25.4.5 Emission Mössbauer Spectroscopy

In an *emission experiment*, the radioactive excited-state Mössbauer nuclide is introduced into the sample to be investigated. In a Mössbauer experiment only the relative velocity of the source and the sample matters. Therefore, the emission experiment may be considered as a simple mirror image of the transmission experiment. This is well reflected by the upper panel of *Fig. 25.6*, where the "u" axes for the (moving) source and absorber point in opposite directions. Instead of a standard source, one can use, in this case, a standard absorber, which consists of a single-peak compound (i.e., no quadrupole splitting and no magnetic splitting is allowed in the absorber). The most commonly used reference material is potassium hexacyanoferrate(II), $K_4[Fe(CN)_6]\cdot 3H_2O$.

However, the source, which is supposed to be a material doped with a Mössbauer nuclide in its excited state cannot be prepared because the half-life is so short that the source would completely decay before one would start the experiment (for ^{57}Fe, $\tau_{1/2} \approx 10^{-7}$ s). Thus, one has to find a parent nuclide with a reasonably long half-life, which produces the excited Mössbauer level by nuclear decay. This has the consequence that in an emission experiment the dopant element may be different from the Mössbauer active one. In ^{57}Fe Mössbauer spectroscopy, this parent nuclide is ^{57}Co, which decays by electron capture, $^{57}Co(EC)^{57}Fe$, with a half-life of ~9 months.

The doping with a parent element different from the Mössbauer one needs further considerations. The microenvironment of the parent nuclide in the doped sample may be different from that of its daughter element, the Mössbauer nuclide. (That is, the lattice site occupied and the coordination number or the valence state can all be different.) More importantly, the radioactive decay of the parent nuclide can trigger a relaxation process that alters the microenvironment of the Mössbauer dopant, which, in turn, affects the Mössbauer spectrum. These effects are called "aftereffects" (see Sect. 25.4.5.1), and in many cases these are the primary targets of this kind of Mössbauer studies in order to explore the hot-atom reactions triggered by the radioactive decay.

A substantial advantage of emission Mössbauer spectroscopy in comparison with the transmission technique is that if the material to be investigated contains heavy elements, then the required dopant concentration (e.g., ^{57}Co) may be 1–2 orders of magnitude lower in the emission experiment than the ^{57}Fe concentration in an analogous transmission experiment. This is in connection with the intensity loss of the Mössbauer radiation due to electronic absorption, which is always *self absorption* in the source and *regular absorption* in the absorber (Vértes and Homonnay 1997). Low dopant concentration is very important in *impurity Mössbauer spectroscopy*, where the investigated material does not contain a Mössbauer element; thus, a conveniently measurable Mössbauer nuclide is introduced artificially as an impurity with a potential risk of perturbing the physicochemical properties of the host phase.

25.4.5.1 Aftereffects

Aftereffects (Spiering et al. 1990; Nagy 1994) show up in the Mössbauer spectra if the relaxation process, which might have been triggered by the nuclear decay of the parent nuclide, is not finished by the time of the decay of the Mössbauer level, or, if it has caused an irreversible change in the microenvironment of the Mössbauer nuclide.

In the case of ^{57}Co, the electron capture triggers an Auger cascade with high probability, in which electrons, mostly in the energy range 0.6–6 keV, will be produced. The resultant highly charged iron ion (up to Fe^{7+}) starts then to recapture electrons and may reach the original oxidation state of the parent nuclide. This neutralization is accompanied by deposition of large excitation energy that has to dissipate fast and smoothly in order to save the microenvironment of the Mössbauer nuclide. If all these processes are completed in $\sim 10^{-9}$ s, then they will be invisible in the Mössbauer spectrum. The probability of this fast relaxation depends most of all on the electronic conduction properties of the host material.

In metals, electronic relaxation is fast and no aftereffects can be detected by Mössbauer spectroscopy. (This is why ^{57}Co can be built in metallic matrices in commercial sources for ^{57}Fe Mössbauer spectroscopy.)

In insulators and semiconductors, aftereffects show up in most cases in the form of *aliovalent charge states* (when the charge state of the nucleogenic ^{57}Fe is different from the equilibrium charge state of iron in that particular host material). The aliovalent charge states are typically higher than the equilibrium charge state (e.g., observation of Fe^{3+} in ^{57}Co-doped CoO, see Harami et al. 1984), but they can also be lower (e.g., Fe^{+} in Co^{2+}-doped ZnS, see Garcin et al. 1980). In these ionic or ionic/covalent lattices, the formation of aliovalent charge states is explained mostly by the *competing acceptors model* (Helms and Mullen 1971; Perfiliev et al. 1976).

Aliovalent Fe^{3+} charge states can be observed in frozen aqueous solution of Co(II)-salts, where the formation of Fe^{3+} can be explained by the *radiolysis model*. In this model, oxidation of the nucleogenic Fe^{2+} to Fe^{3+} is assumed by OH radicals, which form during the radiolysis of water molecules coordinated to the parent Co^{2+} ion, by Auger electrons (Friedt and Danon 1980).

Excited electronic states due to aftereffects have been found and verified in only a few cases but in various compounds like in ^{57}Co-doped $LiNbO_3$ (Doerfler et al. 1984) and ^{57}Co/Co $(phen)_3(ClO_3)_2{\cdot}2H_2O$ (Ensling et al. 1970).

Bond rupture and complete *fragmentation* of the host molecule due to the deposited large excitation energy during the neutralization of the Auger-ionized Fe^{n+} ion has also been suggested in certain coordination compounds. It was observed that the higher the degree of delocalization in the ligands coordinated to the ^{57}Co center, the higher is the chance to avoid the (supposed) fragmentation (Srivastava and Nath 1976).

Time-differential Mössbauer emission spectroscopy (see Alflen et al. 1989) has also been applied to explore aftereffects.

25.4.6 Thermal Scan Method

In the case of the *Mössbauer thermal scan method*, the spectrum point belonging to zero (or a given constant) velocity is only measured at different temperatures (in the case of zero velocity without Doppler moving). By this simple technique, phase transition temperatures can be detected.

25.4.7 Mössbauer Polarometry

The principle of *Mössbauer polarometry* is similar to that of optical polarometry. In this case, the polarization and the analysis can be performed by appropriately oriented external magnetic fields. Using ^{57}Fe polarization spectroscopy 36 lines, rather than six, are observed with magnetic materials (Gonser and Fisher 1981).

25.4.8 Capillary Mössbauer Spectroscopy

Normally, in liquid state, the recoil of the nucleus at the γ-ray emission hampers the nuclear resonance absorption. However, Mössbauer spectra of liquids can be observed even at room temperature if the molecules of liquids are trapped in the cavities of a special porous silicate glass of a mean pore diameter of $\sim$4 nm. This type of Mössbauer spectroscopy is called capillary Mössbauer spectroscopy (Burger and Vértes 1983).

Three different types of behavior were experienced in various systems. It was concluded from the comparison of the Mössbauer parameters of samples obtained in liquid phase and in frozen solution that, in the case of aqueous solution of the Mössbauer active salts, only the solvent molecules were in chemical interaction with the wall of the capillaries in the glass. The microenvironments of the Mössbauer active species were the same both in liquid state and in the frozen solution.

In another case, when the Mössbauer parameters observed for the liquid state were different from those in frozen solution (e.g., SnI_4 in carbon tetrachloride) the Mössbauer atoms were in direct chemical interaction with the wall of the pores of the carrier.

In the third case, when two Mössbauer subspectra were observed in the liquid state and only one of them corresponded to the frozen solution, a fraction of the Mössbauer species was bound to the wall of pores, and the other part exhibited parameters characteristic of the free species.

It was found that high donicity of the solvent is required to keep the Mössbauer solute off the wall of the cavities, which enables one to study the bulk structure of solutions with Mössbauer spectroscopy in liquid phase.

25.4.9 Time-Dependent Measurements

Time-differential Mösssbauer spectroscopy (Kajcsos et al. 1986; Alflen et al. 1989; Kobayashi 1989; Nakada et al. 1994) presents a unique tool for the study of chemical aftereffects and relaxation processes following the electron capture of ^{57}Co incorporated into various matrices. The principle of this method is as follows.

Using two detectors simultaneously, one has to detect the 122 keV γ quanta coming from the Mössbauer source as a start signal. This actually marks the birth of the 14.4 keV Mössbauer excited level (see the decay scheme in *Fig. 25.7*). Then, with the other detector, the 14.4 keV γ quantum is detected, and the elapsed time measured (stop signal). With this method, Mössbauer spectra can be recorded in any time interval after the nuclear decay of ^{57}Co. Recording characteristic X-rays following the electron capture, part of the aftereffect events can be filtered off. Due to the coincidence technique, very low activities can only be used, and therefore these measurements are rather time consuming (several weeks or months).

25.4.10 Combined Methods

A number of techniques also use Mössbauer spectroscopy combined with other methods like X-ray diffractometry (Parak et al. 1976; Faigel and Tegze 1994; Kriplani et al. 2002) and electron spectroscopy (Hisatake et al. 1974; Klingelhofer and Meisel 1990).

25.4.11 Measurements Using Synchrotron Radiation

Synchrotron radiation can also be used instead of radioactive sources for the nuclear resonance scattering (Ruby 1974; Gerdau et al. 1985). Since the already achieved results and the future perspectives of this method are very promising, a separate Chapter (see Chap. 26 in this Volume) is devoted to this topic.

25.4.12 Sources and Absorbers

The *Mössbauer source* is a solid material containing (or rather continuously generating) the excited-state nuclei of the studied nuclide and thus emitting the γ radiation characteristic of the nuclear transition in question. Although Mössbauer transition has been observed with more than 48 nuclides (➲ *Fig. 25.4*), only a few of them are widely used – those having a relatively long-lived parent nuclide making it possible to produce a source lasting for at least a couple of months. The most common Mössbauer nuclides (and their share from the Mössbauer literature) are as follows: ^{57}Fe (82%), ^{119}Sn (6%), and ^{151}Eu (3%). The remaining 9% is divided among 45 nuclides. The commercial source for the 14.4 keV transition of ^{57}Fe is ^{57}Co diffused into a thin metallic matrix (e.g., Pd, Pt, and Rh) in which the emitted Mössbauer line is sufficiently narrow (to make it possible to produce experimental spectrum peaks as narrow as $W = 0.21$ mm/s). The activity of such sources is typically about 200 MBq to 10 GBq.

The isomer shifts are usually given relative to α-Fe. If the isomer shift is given relative to a particular source matrix, conversion is possible with the help of ➲ *Table 25.3*.

If a proper parent nuclide cannot be found for an otherwise promising (e.g., low-energy) isomeric transition for source preparation, the Mössbauer nuclide may be generated continuously by (n,γ) reaction. In such a situation, prompt or slightly delayed γ quanta are used for Mössbauer purpose. The basic requirement is that, for the potential $^{A+1}_{Z}$N Mössbauer nuclide, there should exist an $^{A}_{Z}\mathrm{N}(\mathrm{n},\gamma)^{A+1}_{Z}\mathrm{N}$ reaction with high cross section, and one should have access to a nuclear reactor with high neutron flux capability. A few tens more possible Mössbauer transitions become available with this method; however, the technical background is rather complex.

Normally, the studied sample is used either as an absorber or a scatterer. The *absorber* has to contain the ground-state nuclei of the nuclide responsible for the Mössbauer radiation of the source. Mössbauer absorbers used for transmission experiments can be sheets or powders of solids. Frozen solutions can also be measured.

The ideal sample has uniform thickness, circular shape, texture-free homogeneous distribution of material, and optimum surface density of the Mössbauer nuclide as well as an optimum thickness (Nagy et al. 1975).

For example, in the case of a natural α-iron foil 7 mg/cm^2 natural iron content (i.e., a linear thickness of 9 μm) is the optimum; however, 0.2 mg/cm^2 samples can also be measured with some difficulty. From the point of view of the Mössbauer resonant transition, only the ^{57}Fe

Table 25.3

^{57}Fe isomer shift conversion for some frequently used standard matrices. To obtain isomer shift values relative to α-Fe, one has to add the corresponding value in column 2 to the isomer shift measured relative to the standard material in column 1

Source matrix/standard material relative to which the isomer shift δ is given	Correction (in mm s^{-1}) to be added to δ to get the isomer shift relative to α-Fe
Sodium nitroprusside (SNP)	−0.257
Chromium (Cr)	−0.147
Stainless steel (SS)	−0.092
α-Iron (reference)	0.000
Rhodium (Rh)	+0.109
Palladium (Pd)	+0.170
Copper (Cu)	+0.227
Platinum (Pt)	+0.344

content is important (which has a 2.14% abundance in natural iron), and therefore, a significant lowering of the minimum iron content (down to a factor of 1/45) can be achieved by enrichment with that isotope. Thus, e.g., the spectrum of an aluminum sample containing 20 ppm of ^{57}Fe can be easily measured by a conventional modern spectrometer.

Powders to be measured are usually spread out with uniform thickness between thin foils of Mylar or aluminum. Sometimes, in order to avoid vibrational effects, the powder is embedded in a matrix with low atomic absorption (e.g., paraffin, granulated organic, and polymer). It is important that neither the matrix nor the foil should contain any traces of the resonant nuclide (which can happen with aluminum in the case of ^{57}Fe measurements).

For samples used in *scattering experiments*, there is no essential demand other than the available surface density of the Mössbauer nuclide.

25.4.13 Cryostates, Furnaces, Magnets, and Pressure Cells

Different kinds of *cryostats* and furnaces are used to determine the temperature dependence of Mössbauer spectra. A simple *cold-finger* cryostat can be designed to measure at the temperature of solid CO_2 or liquid nitrogen. In this case, the precooled sample can be immediately put into the cryostat. This is important, e.g., with frozen solution samples. Temperature-controlled evacuated cryostats are generally applied between the millikelvin and a few hundred kelvin temperature range. They have to be supplied with special coolants (e.g., liquid helium or nitrogen). Nowadays closed circuit *refrigerator* cryostats operating between 12 to 400 K are also used frequently because they do not require liquid helium.

Temperature-controlled *furnaces* operate between room temperature and 1,500 K. *Cryofurnaces* can operate both below and above room temperature.

External magnetic fields are generated by *magnets* producing a field from 1 mT or so to 15 T. High fields are obtained by superconducting magnets. The magnet is usually placed around the cryostat or the furnace.

Cryostats are sometimes combined with *pressure chambers*, which can produce the required pressure on the sample. The high-pressure chambers are capable of pressures up to 200 kbar without disturbing the Mössbauer measurements.

25.5 Applications

Mössbauer spectroscopy has been used to solve problems in a variety of fields. Here is a list of a few examples: archeology (Kostikas et al. 1976), art (Keisch 1976), biochemistry and biology (Moshkovskii 1968; May 1971; Kuzmann 1979; Mössbauer et al. 1981), chemistry (Goldanskii and Herber 1968; Greenwood and Gibb 1971; Gütlich et al. 1978; Vértes et al. 1979; Long 1984; Long 1987; Vértes and Nagy 1990), electronics (Langouche 1989), magnetism (Grant 1975; Long and Grandjean 1993, 1996, 1997), materials sciences, solid-state physics and engineering (Gonser 1971, 1975b; Zemcik 1971), mineralogy and geology (Bancroft 1973; Mitra 1992; Kuzmann et al. 1998), nuclear physics and nuclear chemistry (Hafemeister 1971), physical metallurgy (Fujita 1975), and relativity (Pound 1981).

Shortly after the discovery of recoilless nuclear resonance emission/absorption on ^{193}Ir by Rudolf Mössbauer (Mössbauer 1958a) the Mössbauer effect was shown with ^{57}Fe (Shiffer and Marshall 1959; Pound and Rebka 1959; Hanna et al. 1960; de Pasquali et al. 1960) and somewhat later with ^{119}Sn (Bartaloud et al. 1960; Deljagin et al. 1960), which nuclides are till now the most frequently used Mössbauer isotopes. The verification of the gravitational red shift of electromagnetic radiation (Pound and Rebka 1960) draws widespread scientific attention to Mössbauer spectroscopy.

More than 40,000 publications are available on various applications. The yearly number of publications is still growing. Bibliographic and other information about all these applications can be found in the Mössbauer Effect Reference Data Index (MERDI) and Mössbauer Effect Reference Data Journal (MERDJ). Many applications are discussed in monographs and in the proceedings of Mössbauer conferences (ICAME, ISIAME, LACAME, and other meetings of Mössbauer spectroscopists).

Accurate knowledge of the physical properties of the nuclei to be used for Mössbauer purpose opens the way for Mössbauer spectroscopy to become a really powerful tool in various research fields. In the followings, a few applications from the field of nuclear sciences are presented along with a list about the important chemical and analytical application areas.

25.5.1 Applications in Nuclear Sciences

Nuclear parameters can be determined and decay aftereffects can be studied with the help of Mössbauer spectroscopy (Hafemeister 1971; Burgov and Davidov 1968; Speth et al. 1978).

Nuclear parameters especially those *of the excited state* can be obtained from the hyperfine split Mössbauer spectrum.

The *nuclear spin* quantum number of excited state can be derived from the hyperfine spectra, but this is usually known before the Mössbauer experiment.

The fractional *change in the nuclear radius* $\Delta R/R$ can be obtained from the expression of isomer shift (➲ Eq. (25.83)). For this reason, the accurate knowledge of the difference in the electronic density at the site of nucleus of source and absorber is necessary. Because of the difficulties in the estimation of electronic densities at the nucleus, the values of $\Delta R/R$ have considerable uncertainty (Shenoy and Wagner 1978).

The *nuclear magnetic moment* or the *g-factor* of the excited state can be determined with high accuracy from the magnetic splitting (➲ Eq. (25.93)) since the ground-state values are previously known. In certain cases, large external magnetic field is needed to resolve the magnetically split lines (deWaard and Heberle 1964).

For a nucleus with ground-state nuclear spin higher than 1/2, the energy differences between the states in the quadrupole splitting will contain the ratio of the *quadrupole moments* of the excited state and the ground state. If the value of the quadrupole moment of the ground state is known from an independent experiment, then the quadrupole moment of the excited state is obtained from the corresponding ratio (Hafemeister et al. 1964).

For nuclei with ground-state spin $I_g = 1/2$, the determination of quadrupole moment from the expression of quadrupole splitting energy (➲ Eq. (25.90)) can be performed with a relatively large error (Ingalls 1964; Artman et al. 1968; Chappert et al. 1969).

The *internal conversion coefficient* for ^{57}Fe has been accurately determined from the transmission integral (see ➲ Eqs. (25.11), (➲ 25.30), and (➲ 25.31)) by using a series of iron absorbers all having the same thickness of iron atoms but the enrichment in ^{57}Fe varied by a factor of as much as 37 (Hanna and Preston 1965).

Basically, the *lifetime of the excited state* can be determined from the line width (➲ Eq. (25.2)). However, several broadening effects influence the exact determination of the nuclear lifetime (Hafemeister and Shera 1966), which can be obtained within the range of 10^{-7} and 10^{-10} s. Mössbauer spectroscopy is a unique tool for this application.

A Mössbauer experiment was successfully performed to confirm the *parity nonconservation* in β decay. The Mössbauer spectrum was recorded in a β–γ coincidence experiment and an unequal population of the excited state sublevels was observed when the nuclei in the source were polarized by a large magnetic field in the direction of the β radiation (DeWaard et al. 1968).

The *multipole mixing ratio* δ of mixed M1+E2 radiation ($\delta = |E2/M1|$) as well as the phase angle between E2 and M1 components can be obtained from the relative areas of the corresponding peaks (Kistner 1968; Wagner et al. 1968; Atac et al. 1968). The value of the phase angle has a relevance in testing the time reversal in electromagnetic interaction. No violation of time reversal was found in Mössbauer experiments (Kalvius et al. 1968; Mullen 1986).

25.5.2 Chemical and Analytical Applications

The application of Mössbauer spectroscopy in chemistry is based on the utilization of information obtained mainly from the isomer shift, quadrupole splitting, and magnetic splitting.

The chemical isomer shift is a direct function of the s-electron density at the nucleus (see Eqs. (25.83)–(25.85), Shenoy and Wagner 1978), but shows secondary induced effects due to changes in shielding (i.e., electron–electron repulsion) of the s-electrons by p-, d-, or f-electrons. It is therefore sensitive to most changes of orbital occupation in the valence shell of the atom. Since there are well-established monotonous correlations between the electronic density and the oxidation and spin state of the Mössbauer atom, the isomer shift can be used for the *determination of the oxidation and spin state* of Mössbauer nuclides. Isomer shift scales as a function of the oxidation state are now available for a large number of Mössbauer nuclides, and they are helpful in characterizing unknown materials and identifying different species of a certain Mössbauer nuclide in a mixture in wide areas of inorganic chemistry, organic chemistry, biochemistry, and geochemistry.

The quadrupole splitting (Eqs. (25.90)–(25.91), see, e.g., Travis (1971), Gütlich et al. (1978)) is caused by the asymmetric occupation of the nonspherical p-, d-, or f-electron orbitals, and its magnitude and sign can also be used to *determine the asymmetry of the charge distribution with respect to chemical bond.*

The variation of the coordination number in compounds results primarily in a change in the symmetry of the coordination sphere; therefore, the quadrupole splitting can serve as an indicator of such a change. At the same time, the contraction or expansion of the coordination sphere also affects the bond strength between the ligands and the central Mössbauer atom, which will be reflected in the isomer shift values.

One can obtain information about the molecular geometry mainly from the *electric field gradient* data derived from the quadrupole splittings. The principal component of electric field gradient can be written as (Gütlich et al. 1978)

$$V_{zz} = (1-\gamma_\infty)(V_{zz})_{\mathrm{L}} + (1-R)(V_{zz})_{\mathrm{VAL}} = (1-\gamma_\infty)(V_{zz})_{\mathrm{L}} + (1-R)[(V_{zz})_{\mathrm{CF}} + (V_{zz})_{\mathrm{MO}}] \tag{25.131}$$

where $(V_{zz})_{\mathrm{L}}$ is the *ligand contribution* arising from the aspherical charge distribution in the ligand sphere and/or lattice surroundings with a symmetry lower than cubic, $(V_{zz})_{\mathrm{VAL}}$ is the *valence electron contribution* due to the aspherical distribution of electrons in the valence orbitals. $(V_{zz})_{\mathrm{VAL}}$ can be divided into two parts due to nonspherical population of the *d*-orbitals according to crystal field splitting $(V_{zz})_{\mathrm{CF}}$ and due to anisotropic population of molecular orbitals $(V_{zz})_{\mathrm{MO}}$. The parameters γ_∞ and R are the Sternheimer factors (Sternheimer 1963).

In the case of compounds where the ligand contribution determines the V_{zz}, the *point-charge model* can be applied to calculate the electric field gradient as the sum of independent contributions of each ligand. Based on the point-charge model, the calculation of V_{zz} for trans and cis isomers of mixed octahedral complexes (Travis 1971) results $(V_{zz})_{\mathrm{trans}} = -2(V_{zz})_{\mathrm{cis}}$. This makes Mössbauer spectroscopy very sensitive to distinguish between *cis and trans isomers* by measuring the corresponding quadrupole splitting values.

When the *valence contribution* determines the V_{zz}, the *crystal fields* in the complex compounds (e.g., in the case of high-spin iron(II) or low-spin iron(III) compounds with D_{4h} symmetry) can be determined (Gütlich et al. 1978) by measuring the temperature dependence of the quadrupole splitting (Eq. (25.106)). In these cases, the change in the thermal

Table 25.4

Characteristic applications of Mössbauer spectroscopy considered as fundamental studies of compounds

Fundamental studies of compounds
Electronic structure Determination of oxidation and spin states of the Mössbauer atom, spin transitions (spin crossover)
Bond properties σ and π interactions between the Mössbauer atom and ligands, influence of electronegativity of ligands
Structural properties Molecular geometry, determination of cis- and trans isomers, distortion from cubic symmetry (Jahn–Teller effect), effect of polymerization, finding the right structure of polynuclear complexes, identification of possible structural position occupied by the Mössbauer atom, determination of distribution of Mössbauer atoms among the sites, determination of site preference, determination of coordination number, effect of neighbors
Crystal structure Determination of crystalline and amorphous states, determination of crystal anisotropy, defects and defect structures, characterization of quasicrystalline, microcrystalline, nanocrystalline and amorphous materials
Magnetic properties Diamagnetism, paramagnetism, temperature-dependent spin-changes, spin relaxations, cooperative phenomena, ferromagnetism, ferrimagnetism, antiferromagnetism, determination of transition temperature, determination of magnetic structure
Dynamic processes Phonon mode changes, determination of Debye temperature, determination of effective mass, determination of anisotropy of lattice vibration, electron hopping in spinels, diffusion, determination of jump frequency and diffusion coefficient, paramagnetic spin relaxation, spin–spin relaxation, spin-lattice relaxation, superparamagnetism, determination of grain size

electronic population of the low-lying orbitals is taken into consideration in the temperature dependence of $(V_{zz})_{\mathrm{CF}}$.

Bonding properties of complex compounds can be obtained by using data both from isomer shift and quadrupole splitting together, since the electronic density and the electric field gradient at the Mössbauer nucleus are influenced differently by σ donor and π acceptor strengths of surrounding ligands, covalency effects, oxidation/reduction processes, difference in electronegativity of ligands coordinated to the Mössbauer atom, etc.

Magnetically split Mössbauer spectra can be obtained not only with ferro-, ferri-, and antiferromagnetic materials but with paramagnetic compounds, too, when the electronic spin orientation changes slowly as compared to the Larmor precession of the Mössbauer nucleus (paramagnetic spin relaxation, see Wickman et al. 1966). In these cases the internal magnetic flux density at the site of nucleus, $\boldsymbol{B}_{\mathrm{int}}$, is determined from the magnetic splitting (see Eqs. (25.93) and (25.94)). The internal magnetic flux density originates from several terms. In the absence of an external field, $\boldsymbol{B}_{\mathrm{int}} = \boldsymbol{B}_{\mathrm{c}}+\boldsymbol{B}_{\mathrm{orb}}+\boldsymbol{B}_{\mathrm{dip}}$, (Watson and Freeman 1961). The Fermi-contact term $\boldsymbol{B}_{\mathrm{c}}$ arises from the unbalanced spin density of s electrons at the nucleus, the orbital term $\boldsymbol{B}_{\mathrm{orb}}$ is from the orbital angular momentum of the ion, while the dipolar term $\boldsymbol{B}_{\mathrm{dip}}$ is the field produced at the nucleus by the arrangement of atomic moments through the crystal. By measuring the dependences of the magnetic splitting either on temperature or on concentration of Mössbauer atoms, the *spin-lattice* and *spin–spin relaxation* can also be studied.

As a conclusion, one can distinguish between two main characteristic kinds of applications of Mössbauer spectroscopy in chemistry. It can be applied to study *fundamental properties* of compounds as well as it serves as an *analytical tool* for identifying chemical species. In the latter case it is usually used as a fingerprint method (see Sect. 25.3.3). In *Tables 25.4* and *25.5* characteristic applications of Mössbauer spectroscopy in various fields of chemistry are collected.

Table 25.5

Characteristic applications of Mössbauer spectroscopy considered as analytical studies

Analytical studies
Phase and chemical analysis in compounds and alloys
Surface studies Corrosion, determination of corrosion products on iron and steel surfaces, adsorption properties of ion exchangers, catalysis, surface reactions on catalysts, coatings, effect of the preparation parameters on the phase composition and the short-range order
Solid-state reactions Ligand exchange in transition metal complexes, thermal and radiation-induced decomposition, pressure-induced reactions, electron exchange reactions, substitutional effects in sophisticated oxides
Frozen solution studies Hydration and solvation effects, electron exchange reactions, polymerization
Phase transformation Change in crystal structure, crystallization of amorphous materials, magnetic ordering

References

Abragam A (1964) L'Effect Mössbauer. Gordon & Breach, New York

Alflen M, Hennen C, Tuczek F, Spiering H, Gütlich P, Kajcsos Zs (1989) Hyperfine Interact 47–48:115

Andreeva MA, Kuzmin RN (1984) Phys Stat Sol B 125:461

Artman JO, Muir AH, Wiedersich H (1968) Phys Rev 173:337

Atac M, Crisman B, Debrunner P, Frauenfelder H (1968) Phys Rev Lett 20:691

Bancroft GM (1973) Mössbauer spectroscopy. McGraw Hill, London

Bartaloud R, Picou JL, Tsara C (1960) C R Acad Sci Paris 250:2705

Baverstam U, Bohm C, Ringstrom B, Ekdahl T (1973) Nucl Instr Meth 108:439

Belozerskii GN (1993) Mossbauer studies of surface layers. Elsevier, Amsterdam

BESSEL (2010) http://www.efunda.com/math/bessel/bessel.cfm Accessed 2nd October, 2010

Bhide VG (1973) Mössbauer effect and its applications. Tata McGraw-Hill, New Delhi

Blatt JM, Weisskopf VF (1959) Theoretische Kernphysik. Teubner, Leipzig

Bonchev T, Jordanov A, Minkova A (1969) Nucl Instr Meth 70:36

Bonchev Ts, Minkova A, Kushev G, Grozdanov M (1977) Nucl Instr Meth 147:481

Breit G, Wigner E (1936) Phys Rev 49:519

Budakovski SV, Iliassov AZ, Kruglov EM, Lavrov AO, Rogozev BI (1999) Proceedings of the conference on ICAME99, T9/22. Garmisch-Partenkirchen, Germany

Burger K, Vértes A (1983) Nature 306:353

Burgov NA, Davidov AV (1968) In: Goldanskii VI, Herber RH (eds) Chemical applications of Mössbauer spectroscopy. Academic, New York, London

Campbell SJ, Aubertin F (1989) In: Long GJ (ed) Mössbauer spectroscopy applied to inorganic chemistry, Vol 3. Plenum, New York

Chappert J, Frankel RB, Misetich A, Blum NA (1969) Phys Rev B 28:406

Clauser MJ, Mössbauer RL (1969) Phys Rev 178:559

Cohen RL (1976) Applications of Mössbauer spectroscopy I. Academic, New York, San Francisco, London

Cohen RL (1980) Applications of Mössbauer spectroscopy II. Academic, New York, San Francisco, London

Cohen SG, Pasternak M (1973) Perspectives in Mössbauer spectroscopy. Plenum, New York, London

Cook DC, Agyekum E (1985) Nucl Instr Meth B 12:515

Cranshaw TE, Dale BW, Longworth CO, Johnson CE (1985) Mössbauer spectroscopy and its applications. Cambridge University Press, Cambridge

Danon J (1968) Lectures on the Mössbauer effect. Gordon & Breach, New York

De Pasquali G, Frauenfelder H, Margulies S, Peacock RN (1960) Phys Rev Lett 4:71

Deljagin NN, Shpinel VS, Bryukhanov VA, Zwenglinski B (1960) Zh Exp Theor Fiz 39:894

deWaard H, Heberle J (1964) Phys Rev 136:1615

DeWaard H, Heberle J, Schurrer PJ, Hasper H, Koks WWJ (1968) In: Matthias E, Shirley DE (eds) Hyperfine structure and nuclear reactions. North Holland, Amsterdam

Doerfler R, Nagy DL, Pfannes H-D, Putzka A, Ritter G, Zeman N (1984) Phys Stat Sol B 124:767

Dunlap BD, Kalvius GM (1978) In: Shenoy GK, Wagner FE (eds) Mössbauer isomer shifts. Noth Holland, Amsterdam, New York, Oxford

Eicher H, Trautwein A (1969) J Chem Phys 50:2540

Ensling J, Fitzsimmons BW, Gütlich P, Hasselbach KM (1970) Angew Chem 82:638

Faigel Gy, Tegze M (1994) Hyperfine Interact 92:1137

Foyt DC, Good ML, Cosgrove JG, Collins RL (1975) J Inorg Nucl Chem 37:1913

Frauenfelder H (1962) The Mössbauer effect. Benjamin, New York

Friedt JM, Danon J (1980) At Energy Rev 18:893

Frost JC, Cowie BCC, Chapman SN, Marshall JF (1985) Appl Phys Lett 47:581

Fujita FE (1975) In: Gonser U (ed) Mössbauer spectroscopy. Springer, New York

Fujita FE (ed) (1999) Introduction to the Mossbauer spectroscopy – principles and applications. Agune Gijutsu Center, Tokyo

Fukumura K, Nakanishi A, Kobayashi T, Katano R, Isozumi Y (1991) Nucl Instr Meth Phys Res A 301:482

Garcin C, Imbert P, Jehanno G, Gerard A, Danon J (1980) J Phys Chem Solids 41:969

Gerdau E, Rüffer R, Winkler H, Tolksdorf W, Klages CP, Hannon JP (1985) Phys Rev Lett 54:835

Gibb TC (1976) Principles of Mossbauer spectroscopy. Chapman & Hall, London

Goldanskii VI (1963) The Mössbauer effect and its application to chemistry. Izd. Academii Nauk, Moscow

Goldanskii VI, Herber RH (1968) Chemical applications of Mössbauer spectroscopy. Academic, New York, London

Goldanskii VI, Makarov EF, Khrapov VV (1963) Phys Lett 3:334

Gonser U (1971) In: May L (ed) An introduction to Mössbauer spectroscopy. Adam Hilger/Plenum, London, New York

Gonser U (ed) (1975a) Mössbauer spectroscopy. Springer, New York

Gonser U (1975b) Proceedings of the conference ICAME, 113. Cracow, Poland

Gonser U (ed) (1981) Mössbauer spectroscopy II – the exotic side of the method. Springer, Berlin

Gonser U, Fisher H (1981) In: Gonser U (ed) Mössbauer spectroscopy II – the exotic side of the method. Springer, Berlin

Grant RW (1975) Mössbauer spectroscopy in magnetism. In: Gonser U (ed) Mössbauer spectroscopy. Springer, New York

Greenwood NN, Gibb TC (1971) Mössbauer spectroscopy. Chapman & Hall, London

Gruverman IJ (ed) (1965) Mössbauer effect methodology, Vol 1. Plenum, New York

Gruverman IJ (ed) (1966) Mössbauer effect methodology, Vol 2. Plenum, New York

Gruverman IJ (ed) (1967) Mössbauer effect methodology, Vol 3. Plenum, New York

Gruverman IJ (ed) (1968) Mössbauer effect methodology, Vol 4. Plenum, New York

Gruverman IJ (ed) (1970) Mössbauer effect methodology, Vol 5. Plenum, New York

Gruverman IJ (ed) (1971a) Mössbauer effect methodology, Vol 6. Plenum, New York

Gruverman IJ (ed) (1971b) Mössbauer effect methodology, Vol 7. Plenum, New York

Gruverman IJ (ed) (1974) Mössbauer effect methodology, Vol 9. Plenum, New York

Gruverman IJ (ed) (1976) Mössbauer effect methodology, Vol 10. Plenum, New York

Gruverman IJ, Seidel CW (eds) (1973) Mössbauer effect methodology, Vol 8. Plenum, New York

Gütlich P, Link R, Trautwein A (1978) Mössbauer spectroscopy and transition metal chemistry. Springer, Berlin

Hafemeister DW (1971) In: May L (ed) An introduction to Mössbauer spectroscopy. Adam Hilger, Plenum, London, New York

Hafemeister DW, Shera EB (1966) Nucl Inst Meth 41:133

Hafemeister DW, dePasquali D, deWaard H (1964) Phys Rev B 135:1089

Hanna SS, Preston RS (1965) Phys Rev Lett 139:A722

Hanna SS, Heberle J, Littlejohn C, Perlow GJ, Preston RS, Vincent DJ (1960) Phys Rev Lett 4:177 and 513

Harami T, Loock J, Huenges E, Fontcuberta J, Obradors X, Tejada J, Parak FG (1984) J Phys Chem Solids 45:181

Helms WR, Mullen JG (1971) Phys Rev B 4:750

Herber RH (ed) (1984) Chemical Mössbauer spectroscopy. Plenum, London, New York

Hesse J, Rübartsch A (1974) J Phys E Sci Instrum 7:526

Hisatake K, Toriyama T, Kigawa M, Fujioka M (1974) J Jpn Appl Phys 2:733

Housley RM, Grant RW, Gonser U (1969) Phys Rev 178:514

Inaba M, Nakagawa H, Ujihira Y (1981) Nucl Instr Meth 180:131

Ingalls R (1964) Phys Rev A 133:787

Irakaev SM, Andreeva MA, Semrenov VG, Belozerskii GN, Grishin OV (1993) Nucl Instr Meth B 74:545

Isozumi Y, Kurakado M, Katano R (1979) Nucl Instr Meth 166:407

Isozumi Y, Kurakado M, Katano R (1983) Nucl Instr Meth 204:571

Ismail M, Liljequist D (1986) Hyperfine Interact 29:1509

Janot C (1972) L'Effect Mössbauer et ses Applications, a la Physique du Solid et la Metallurgie Physique. Masson, Paris

Kagan Yu (1962) The Mössbauer effect. Izd. Inostrannoi Literatuti, Moscow

Kaipov DK (1976) Nuclear gamma resonance and its related processes. Nauka, Alma Ata

Kajcsos Zs, Alflen M, Spiering H, Gütlich P, Albrecht R, Schulze R, Kurz R (1986) Hyperfine Interact 29:1551

Kajcsos Z, Sauer Ch, Holzwarth A, Kurz R, Zinn W, Ligtenberg MAC, Van Aller G (1988) Nucl Instr Meth Phys Res B 34:384

Kalvius GM, Sprouse GD, Hanna SS (1968) In: Matthias E, Shirley DE (eds) Hyperfine structure and nuclear reactions. North Holland, Amsterdam

Kankeleit E (1961) Z Phys 164:442

Keisch B (1976) In: Cohen RL (ed) Applications of Mössbauer spectroscopy. Academic, New York, San Francisco, London

Kimball CW, Taneja SP, Weber L, Fradin FY (1974) In: Gruverman IJ (ed) Mössbauer effect methodology, Vol 9. Plenum, New York

Kistner OC (1968) In: Matthias E, Shirley DE (eds) Hyperfine structure and nuclear reactions. North Holland, Amsterdam

Kittel Ch (1968) Introduction to solid state physics. Wiley, New York

Klencsár Z, Kuzmann E, Vértes A (1996) J Rad Nucl Chem 210:105

Klingelhofer G, Kankeleit E (1990) Hyperfine Interact 53:1905

Klingelhofer G, Meisel W (1990) Hyperfine Interact 57:1911

Kobayashi T (1989) Bull Chem Soc Jpn 62:576

Kobayashi Y, Yoshida Y, Yoshida A, Watanabe Y, Hayakawa K, Yukihira K, Shimura F, Ambe F (2000) Hyperfine Interact 126:417

Kopcewicz M (1989) In: Long GJ (ed) Mössbauer spectroscopy applied to inorganic chemistry, Vol 3. Plenum, New York

Kostikas A, Simopoulos A, Gangas NH (1976) In: Cohen RL (ed) Applications of Mössbauer spectroscopy. Academic, New York, San Francisco, London

Kriplani U, Regehr MW, Fultz B (2002) Hyperfine Interact 139:667

Kündig W (1967) Nucl Instr Meth 48:219

Kuprin AP, Novakova AA (1992) Nucl Instr Meth Phys Res B 62:493

Kuzmann E (1979) Mösbauer effect in biological research. In: Vértes A, Korecz L, Burger K (eds) Mössbauer spectroscopy. Akadémiai Kiadó, Elsevier, Amsterdam, Oxford, New York, Budapest

Kuzmann E, Nagy S, Vértes A (1994) J Radioanal Nucl Chem Lett 186:463

Kuzmann E, Nagy S, Vértes A, Weiszburg T, Garg VK (1998) In: Vértes A, Nagy S, Süvegh K (eds) Nuclear methods in mineralogy and geology. Plenum, New York, London

Kuzmann E, Nagy S, Vértes A (2003) Pure Appl Chem 75:801

Lamb WE Jr (1939) Phys Rev 55:190

Langouche G (1989) In: Long GJ (ed) Mössbauer spectroscopy applied to inorganic chemistry, Vol 1. Plenum, New York

Liljequist D (1981) Nucl Instr Meth 179:617; 185:599

Lindner A (1984) Drehimpulse in der Quantenmechanik. Teubner, Stuttgart

Lipkin HJ (1960) Ann Phys 9:332

Long GJ (ed) (1984) Mössbauer spectroscopy applied to inorganic chemistry, Vol 1. Plenum, New York

Long GJ (ed) (1987) Mössbauer spectroscopy applied to inorganic chemistry, Vol 2. Plenum, New York

Long GJ (ed) (1989) Mössbauer spectroscopy applied to inorganic chemistry, Vol 3. Plenum, New York

Long GJ, Grandjean F (eds) (1993) Mössbauer spectroscopy applied to magnetism and materials science, Vol 1, Modern inorganic chemistry, Plenum, New York

Long GJ, Grandjean F (eds) (1996) Mössbauer spectroscopy applied to magnetism and materials science, Vol 2, Modern inorganic chemistry, Plenum, New York

Long GJ, Grandjean F (eds) (1997) Mössbauer spectroscopy applied to magnetism and materials science, Vol 3, Modern inorganic chemistry, Plenum, New York

Malmfors KG (1953) Arkiv Fysik 6:49

Margulies S, Ehrman JR (1961) Nucl Instr Meth 12:131

Matthias E, Shirley DE (1968) Hyperfine structure and nuclear reactions. North Holland, Amsterdam

Matthias E, Schneider W, Steffen RM (1963) Arkiv För Gysik 24:97

May L (1971) An introduction to Mössbauer spectroscopy. Adam Hilger, Plenum, London, New York

Mayer-Kuckuk T (1994) Kernphysik. Teubner, Stuttgart, p 93

Meisel W (1994) Hyperfine Interact 92:1213

Mitra S (1992) Applied Mossbauer spectroscopy, physics and chemistry of earth, Vol 18. Pergamon, Oxford, New York, Seoul, Tokyo

Moon PB (1950) Proc Phys Soc 63:1189

Mørup S (1981) Paramagnetic and superparamagnetic relaxation phenomena studied by Mössbauer spectroscopy. Polyteknisk Forlag, Lyngby

Mössbauer RL (1958a) Z Physik 151:124

Mössbauer RL (1958b) Naturwissenschaften 45:538

Mössbauer RL, Wiedemann W (1960) Z Physik 159:33

Mössbauer RL, Parak F, Hoppe W (1981) In: Gonser U (ed) Mössbauer spectroscopy II – the exotic side of the method. Springer, Berlin

Moshkovskii Yu Sh (1968) In: Goldanskii VI, Herber RH (eds) Chemical applications of Mössbauer spectroscopy, Academic, New York and London

Muir A, Ando KJ, Coogan HM (1958–1965) Mössbauer effect data index. Inter Science, New York, London, Sydney

Mullen JG (1986) Hyperfine Interact 29:1513

Mullen JG, Stevenson J (1978) Nucl Instrum Meth 153:77

Nagy DL (1994) Hyperfine Interact 83:3

Nagy S, Lévay B, Vértes A (1975) Acta Chim Akad Sci Hung 85:273

Nakada M, Makaki M, Saeki M, Sagawa C, Aratono Y, Endo K (1994) Hyperfine Interact 92:183

Nomura K, Ujihira Y (1985) Bunseki Kagaku 34:T5

Nomura K, Sharma SS, Ujihira Y (1993) Nucl Instr Meth Phys Res B 76:357

Nozik AI, Kaplan M (1967) J Chem Phys 47:2960

Parak F, Mössbauer RL, Hoppe W (1976) J Phys 37: C6–703

Perfiliev YuD, Kulikov LA, Bugaenko LT, Babeshkin AM, Afanasov MI (1976) J Inorg Nucl Chem 38:2145

Perlow JG (1977) Workshop on new directions in Mössbauer spectroscopy. AIP, New York

Pfannes H-D, Gonser U (1973) Appl Phys 1:93

Pound RW (1981) In: Gonser U (ed) Mössbauer spectroscopy II – the exotic side of the method. Springer, Berlin

Pound RV, Rebka GA Jr (1959) Phys Rev Lett 3:554

Pound RV, Rebka GA Jr (1960) Phys Rev Lett 4:337

Raimes S (1961) The wave mechanics of electrons in metals. North Holland, Amsterdam

Rotenberg M, Bivins R, Metropolis N, Wooten JK Jr (1959) The 3j and 6j symbols. MIT Press, Cambridge

Ruby SL (1974) J Phys 35:C6–209

Sano H (1972) Mössbauer spectroscopy: the chemical applications. Kodansha, Tokyo

Sawicki JA, Tyliszczak T, Gzowski O (1981) Nucl Instr Meth 190:433

Schatz G, Weidinger A, Gardner JA (1996) Nuclear condensed matter physics, Nuclear methods and applications. Wiley, Chichester, New York, Brisbane, Toronto, Singapore

Seagusa N, Morrish AH (1982) Phys Rev B 26:10

Shapiro FL (1960) Usp Fiz Nauk 72:685

Shenoy GK, Wagner FE (eds) (1978) Mössbauer isomer shifts. North Holland, Amsterdam, New York, Oxford

Shiffer JP, Marshall V (1959) Phys Rev Lett 3:556

Shigematsu T, Pfannes HD, Keune W (1980) Am Phys Soc 45:1206

Shirley DA (1964) Rev Mod Phys 36:339

Shpinel VSh (1969) Resonance of gamma rays in crystals. Nauka, Moscow

Singwi KS, Sjolander A (1960) Phys Rev 120:1093

Smit PH, van Stapele RP (1982) Appl Phys A28:113

Speth J, Henning W, Kienle P, Meyer J (1978) In: Shenoy GK, Wagner FE (eds) Mössbauer isomer shifts. Noth Holland, Amsterdam, New York, Oxford

Spiering H, Alflen M, Gütlich P, Hauser A, Hennen C, Manthe U, Tuczek F (1990) Hyperfine Interact 53:113

Srivastava TS, Nath A (1976) J Phys Chem 80:529

Sternheimer RM (1950) Phys Rev 80:102

Sternheimer RM (1951) Phys Rev 84:244

Sternheimer RM (1963) Phys Rev 130:1423

Stevens JG, Shenoy GK (1981) Mössbauer spectroscopy and its chemical applications in: advances in chemistry series, Vol 194. American Chemical Society, Washington DC

Stevens JG, Stevens VE (1966) Mössbauer effect data index (MERDI). Adam Hilger, London

Terrell JH, Spijkerman JJ (1968) Appl Phys Lett 13:11

Thosar BV, Iyengar PK (eds) (1983) Advances in Mössbauer spectroscopy. Elsevier, New York

Topalov P, Proikova A (1985) Nucl Instr Meth Phys Res A 236:142

Travis JC (1971) In: May L (ed) An introduction to Mössbauer spectroscopy. Adam Hilger, Plenum, London, New York

Vértes A, Homonnay Z (1997) Mössbauer spectroscopy of sophisticated oxides. Akadémiai Kiadó, Budapest

Vértes A, Nagy DL (1990) Mössbauer spectroscopy of frozen solutions. Akadémiai Kiadó, Budapest

Vértes A, Korecz L, Burger K (1979) Mössbauer spectroscopy. Akadémiai Kiadó, Elsevier, Amsterdam, Oxford, New York, Budapest

Wagner FE, Kaindl G, Kiennle P, Korner HJ (1968) In: Matthias E, Shirley DE (eds) Hyperfine structure and nuclear reactions. North Holland, Amsterdam

Watson RE, Freeman AJ (1961) Phys Rev 123:2027

Wegener H (1965) Der Mössbauer Effect und seine Anwendung. Bibliographisches Institut AG, Mannheim

Weisstein EW (2010) Wigner 3j-Symbol (MathWorld: A Wolfram Web Resource), http://mathworld.wolfram.com/Wigner3j-Symbol.html. Accessed 2nd October, 2010

Wertheim GK (1964) Mössbauer effect: principles and applications. Academic, New York

Weyer G (1976) Mössbauer Effect Meth 10:301

Weyer G (1990) Hyperfine Interact 58:2561

Wickman HH, Klein MP, Shirley DA (1966) Phys Rev 152:345

Williamson DL, Bukshpan S, Ingalls R (1972) Phys Rev B 6:4194

Window B (1971) J Phys E Sci Instrum 4:40

Zemcik T (1971) Proceedings of the conference ICAME. Dresden, Germany